

AREPO-IDORT: Implicit Discrete Ordinates Radiation Transport for Radiation Magnetohydrodynamics on an Unstructured Moving Mesh

Jing-Ze Ma (马竞泽)*¹, Rüdiger Pakmor¹, Stephen Justham¹, and Selma E. de Mink¹

Max Planck Institute for Astrophysics, Karl-Schwarzschild-Str. 1, 85748 Garching, Germany

March 24, 2025

ABSTRACT

Radiation is crucial not only for observing astrophysical objects, but also for transporting energy and momentum. However, accurate on-the-fly radiation transport in astrophysical simulations is challenging and computationally expensive. Here we introduce AREPO-IDORT (Implicit Discrete Ordinates Radiation Transport), a scheme coupled to the explicit magnetohydrodynamic (MHD) solver in the 3D moving-mesh code AREPO. The discrete ordinates scheme means we directly solve for the specific intensities along discrete directions. We solve the time-dependent relativistic radiation transport equation via an implicit Jacobi-like iterative finite-volume solver, which overcomes the small radiation time-steps needed by explicit methods. Compared to commonly-used moment-based methods, e.g. flux-limited diffusion or M1 closure, this scheme has the advantage of correctly capturing the direction of radiation in both optically-thick and thin regions. It is based on the scheme by Jiang 2021 for the adaptive mesh refinement code ATHENA++, but we generalize the scheme to support (1) an unstructured moving-mesh, (2) local time-stepping, and (3) general equations of state. We show various test problems that commonly-used moment-based methods fail to reproduce accurately. To apply the scheme to a real astrophysics problem, we show the first global 3D radiation hydrodynamic simulation of the entire convective envelope of a red supergiant star. We even marginally resolve the photosphere, which is a known challenge for global 3D simulations of stars. For this problem, the radiation module only takes less than half of the total computational cost. Our current scheme assumes grey radiation, is first-order accurate in both time and space, and is memory intensive especially for large cosmological simulations, but we discuss potential avenues for future improvements. We expect our scheme will enable more accurate multi-scale radiation MHD simulations involving supersonic bulk motions, ranging from planet formation in protoplanetary disks, stars and associated transients, to accretion flows near black holes.

Key words. Radiative transfer – Methods: numerical – Hydrodynamics

Contents

1	Introduction	2	4	Test Problems	12
1.1	Overview: Challenges and Available Methods for Radiation Transport	2	4.1	Steady-state Tests with Fixed Gas Background	13
1.2	Objective: Towards a More Accurate General-purpose 3D Moving-mesh Radiation Magnetohydrodynamic Code	4	4.1.1	2D Crossing Beams in Optically-thin Vacuum	13
2	Basic Equations	5	4.1.2	1D Absorption-dominated Homogeneous Sphere in Spherical Coordinates	14
2.1	General Equations of Radiation Transport	5	4.1.3	1D Scattering-dominated Non-LTE Atmosphere	15
2.2	Radiation Transport Equations under Assumptions	6	4.1.4	2D Shadow Test	16
2.3	Equations of Radiation Ideal Magnetohydrodynamics	7	4.2	Evolving-radiation Tests with Fixed Gas Background	16
3	Implicit Discrete Ordinates Solver	7	4.2.1	2D Dynamic Diffusion	16
3.1	Discretization in Space, Time, and Angular Space	8	4.2.2	2D Expanding Multi-source Radiation Bubbles	17
3.2	Discretized Equations	8	4.3	Radiation Hydrodynamic Tests for Radiation-gas Coupling	18
3.3	Derivation of the Equations for the Iterative Solver	9	4.3.1	2D Thermal Equilibrium in a Uniform Medium	18
3.4	Detailed Scheme for the Radiation Transport Module	11	4.3.2	2D Linear Waves	19
3.5	Coupling to the MHD Solver via the Radiation Source Terms	12	4.3.3	1D Radiation Shocks	21
3.6	Optional Features	12	4.3.4	2D Irradiated Cloud	22
			5	Astrophysical Example: Global 3D Convective Envelope of a Red Supergiant Star	22
			5.1	Numerical Setup	23
			5.2	Results	25

* jingze@mpa-garching.mpg.de

6 Discussion on Caveats and Directions for Future Development	26
6.1 From Grey to Multigroup	26
6.2 From Fast to Faster: GPU Acceleration and Node-to-node Communication	27
6.3 Convergence Criterion and Iterative Solver	29
6.4 Faster Convergence and Higher-order Accuracy: Alternative Implicit Solvers	29
6.5 Heavy Memory Load for Large Simulations	30
7 Conclusions	30

1. Introduction

Radiation plays an essential role in most astrophysical problems. Even in this era of multi-messenger astronomy, electromagnetic radiation is still the dominant way for us to observe astrophysical objects via photometry, spectroscopy, polarimetry, or interferometry. More importantly, radiation interferes with the dynamics of matter through emission, absorption, and scattering. Photons exchange energy with matter in the form of heating, cooling, photoionization and photodissociation, and exchange momentum with matter via radiation pressure or radiation force (Mihalas & Mihalas 1984). For example, radiative heating and cooling determines the thermodynamics and thickness of most astrophysical disks and streams, and significantly alters, e.g. substructures in protoplanetary disks (Zhang et al. 2024), accretion onto protostars or mass-transferring binary stars (Geroux et al. 2016), circularization of the stellar debris in tidal disruption events (Hayasaki et al. 2016), and circumbinary-disk accretion onto supermassive black hole binaries (Tiwari et al. 2025). Ionizing radiation regulates star formation and thermodynamics of the intergalactic medium, thereby controlling galaxy formation, especially at high redshifts (Borrow et al. 2023). Under certain conditions, radiation forces dominate the dynamics, driving outflows in cool (Habing 1996) and hot stars (Castor et al. 1975), active galactic nuclei (AGN; Murray et al. 1995), and super-Eddington accretion flows around compact objects (Jiang & Dai 2024). For many complex astrophysical scenarios, it is therefore crucial to perform multi-dimensional numerical simulations with (magneto)hydrodynamics (MHD) fully coupled with accurate radiation transport to understand the physical processes and provide accurate predictions for the observables.

1.1. Overview: Challenges and Available Methods for Radiation Transport

Radiation transport in radiation MHD (RMHD) simulations is difficult for three reasons caused by the vast range of scales involved: (1) dimension, (2) length-scale, and (3) time-scale. (1) Dimension: The radiation field is not only a function of space and time, but also direction and frequency (Mihalas & Mihalas 1984). This means that if we aim to extend any existing MHD simulation to full RMHD simulation, the number of numerical quantities will expand by one to two orders of magnitude. This poses a major challenge not only to calculate those quantities, but also save them with limited computational power and memory storage (Jiang et al. 2014). (2) Length-scale: The mean free path of photon generally differs from the length-scale of MHD processes by many orders of magnitude. When the photon mean free path is much larger than the length-scale of gas, matter is transparent to light (‘optically thin’), and photons can travel freely at the speed of light. At the other extreme, when the photon mean free path is much smaller than the length-scale of gas,

matter is opaque to light (‘optically thick’), and photons are frequently absorbed and re-emitted or scattered, resulting in a diffusive random-walk of photons. An even more challenging regime is the transition zone from optically-thick to optically-thin, from which the observed light escapes. An accurate radiation transport scheme is expected to capture the physics correctly in all those three regimes, despite the significant differences in physics and mathematical properties of the equation (Stone et al. 1992; Teyssier 2015; Jiang 2021). (3) Time-scale: In the optically-thin regime, radiation travels at the speed of light, which is orders of magnitude larger than the gas speed for non-relativistic simulations. Furthermore, typically in the optically thick regime, the heating and cooling can change the energy content of the plasma at a timescale faster than the normal MHD processes, which poses a numerical challenge in coupling the radiation and gas (Teyssier 2015).

Given the three challenges, one has to make a tradeoff between speed and accuracy for radiation transport methods in RMHD simulations. Motivated by the wave-particle duality of photons and geometrical optics, we broadly separate those methods into three categories (see also Wunsch 2024), namely to treat radiation as (1) particles, (2) rays, or (3) fluids, as summarized in Table 1.

The particle description mainly stands for the Monte Carlo radiation transport (see e.g. Noebauer & Sim 2019, for a review), which generates randomly-sampled photon packets and follows them as they propagate through matter. It is often used for post-processing simulations to make predictions for observables, where detailed microphysics such as scattering and line transport are important (Noebauer & Sim 2015). But it has not been the main stream for multi-dimensional RMHD simulations due to Poisson noise and slow propagation of photon packets in optically-thick regions (Nayakshin et al. 2009; Camps & Baes 2018).

The ray description integrates intensities along straight lines, analogous to the rays of light. This is done by interpolating between cell centers and their projections on the rays (Stone et al. 1992; Freytag et al. 2012). In typical forward ray-tracing methods, the rays originate from each radiation source and end at the simulation boundaries or at the points where the radiation is completely absorbed (Abel & Wandelt 2002; Wise & Abel 2011). For a small number of radiation sources (e.g., some cases in star formation), forward ray-tracing is efficient to calculate heating, cooling, ionization, etc. (Abel & Wandelt 2002; Wise & Abel 2011). However, for a large number of radiation sources, or when every cell is effectively a radiation source, other methods are more efficient. In contrast to forward ray-tracing, short characteristics creates rays from active cell points and traces them only to nearby active mesh points (Stone et al. 1992; Mellema et al. 2006; Davis et al. 2012; Freytag et al. 2012). This method is more diffusive than others and trades accuracy for stability (Stone et al. 1992; Davis et al. 2012; Freytag et al. 2012), because multiple interpolations are needed between cell centers and their projections on the rays, but the fact that the calculations are completely local makes the scheme faster than others (Stone et al. 1992; Mellema et al. 2006; Davis et al. 2012). These ray-based methods perform reasonably well in both optically-thick and thin media, but the huge number of radiation quantities that need to be calculated is still an issue (Abel & Wandelt 2002).

The fluid description of radiation transport, also known as the moment-based methods, does not calculate the intensities but the radiation energy density E_r , radiation flux F_r , and radiation pressure tensor \mathbf{P}_r . This drastically reduces the number

Table 1: Summary and comparison of radiation transport methods. See the main text for details. For a summary of codes using different methods, see e.g. Wunsch (2024).

Category	Particle	Ray	Fluid	Ray-fluid hybrid
Method name	Monte Carlo	Ray-tracing Characteristics	Flux-limited diffusion M1 closure	Variable Eddington tensor Discrete ordinates
<i>Physics</i>				
Accurate direction of radiation?	✓	✓	× ($\tau \lesssim 1$)	✓
Accurate at different optical depths τ ?	× ($\tau \gg 1$)	✓	× ($\tau \lesssim 1$)	✓
Time-and-velocity-dependent?	✓	×	✓	✓
Detailed microphysics (e.g. anisotropic scattering)?	✓	×	×	×
Known difficulties	Poisson noise; Slow transport ($\tau \gg 1$)	Ray-effect* ($\tau \ll 1$)	Filling shadows; Merging crossing beams; Colliding radiation fronts	Ray-effect* ($\tau \ll 1$)
<i>Computational cost for a sophisticated grey 3D simulation (1= comparable to hydro, order-of-magnitude estimate)</i>				
Relative cost	×100	×10	×1	×10
<i>Implementation in AREPO</i>				
AREPO module name	AREPO-MCRT ^a	SPRAT ^b	AREPO-RT ^c	AREPO-IDORT (This work) ^d

Notes. ^(a) Artificial radiation peaks along discrete directions if the number of discretized angles is insufficient, see e.g. Figure 16. ^(a) Smith et al. (2020). ^(b) Jaura et al. (2018, 2020); see also Greif (2014). ^(c) Kannan et al. (2019); Zier et al. (2024a); see also Bauer et al. (2015). ^(d) see also Petkova & Springel (2011) for a semi-implicit source-dependent variance of the discrete ordinates method.

of radiation quantities to be calculated and saved, albeit at the price of making assumptions of the relations between E_r , F_r , \mathbf{P}_r . The simplest method is the flux-limited diffusion (hereafter FLD, e.g. Levermore & Pomraning 1981), which treats the radiation as a diffusion problem, where the radiation flux is always directed along the gradient of radiation energy density. A more sophisticated method is the M1 closure (Levermore 1984), which solves for E_r and F_r simultaneously, but still uses analytical approximations for the Eddington tensor $\mathbf{f}_{\text{Edd}} \equiv \mathbf{P}_r/E_r$ to reproduce the asymptotic limits in both optically-thick and thin regimes. However, due to the diffusion description, FLD cannot cast shadows since the radiation field will diffuse into the shadow (Menon et al. 2022). The approximated Eddington tensor of M1 causes the light to behave like a fluid, resulting in nonphysical phenomena such as merging two crossing radiation beams into one because the radiation is forced to only have one distinguished direction at one location (Sądowski et al. 2013), creating artificial shocks when two radiation fronts meet (Thomas & Pfrommer 2022), or generating unsteady vortices resembling the Karman vortex street in the shadows (Menon et al. 2022). It is also not clear whether FLD and M1 can correctly capture the radiation field in the transition zone between optically-thick and thin regimes (Mihalas & Mihalas 1984). In particular for M1, it has been shown that the Eddington tensor near the photosphere is always overestimated in the radiating homogeneous sphere test (Smit et al. 1997; O’Connor 2015; Murchikova et al. 2017; Anninos & Fragile 2020).

A way to combine the advantages of different methods is to solve the radiation transport problem twice using two methods. This is demonstrated using the Variable Eddington Tensor scheme (hereafter VET, e.g. Stone et al. 1992; Jiang et al. 2012; Menon et al. 2022), which solves for \mathbf{f}_{Edd} using another radiation transport method (ray-based short characteristics in practice), and then solves for both E_r and F_r as in the moment-based methods.

Along this line, in recent years, a novel discrete ordinates radiation transport method has emerged in computational astrophysics, credited to the continuous efforts by Jiang et al. (2014) and Jiang (2021, 2022). This method resembles the ray-based short characteristics: It discretizes the radiation field in angular space and solves for intensities along each direction. The calculations are locally confined within neighbouring cells during each iteration. It also resembles the moment-based methods, as it solves the time-dependent radiation transport equation taking into account the Lorentz transformation and isotropic scattering. The intensities can be calculated using the same mesh as MHD in a finite-volume manner as one solves for energy in the mesh-based MHD simulation, which avoids the interpolation-induced diffusion in the ray-based methods. This method shares the same features of ray-based methods and moment-based VET scheme, that (1) it performs well in all optical depths, and (2) it is relatively computationally expensive and memory intensive. Compared to the VET scheme, it does not solve the radiation transport twice but only once, therefore is more physically self-

consistent. The semi-implicit version of this method (Jiang et al. 2014) has been generalized for moving-mesh codes (Chang et al. 2020), and the fully implicit version (Jiang 2021) (hereafter J21) has been generalized for general relativity (White et al. 2023).

All of those methods face a similar time-scale challenge, that (1) the light propagates much faster than the plasma in optically-thin regime, and (2) the energy exchange between radiation and gas happens much faster than the propagation of fast MHD waves in optically-thick regime. These two time-scale differences correspond to the transport terms and source terms in the radiation transport equation, respectively. Therefore, a fully explicit time-integration where the radiation module and MHD module share the same timestep is often not adequate in RMHD simulations. A way to circumvent this for the transport terms is to adopt a ‘Reduced Speed of Light Approximation’ with subcycling. This approach reduces the speed of light in radiation transport to increase the radiation timestep allowed by explicit time-integration, while keeping the hierarchy of different timescales (e.g. Skinner & Ostriker 2013). However, great caution is needed to use this approximation (Gnedin 2016), which sometimes leads to significant errors (Deparis et al. 2019; Ocvirk et al. 2019; Cain 2024). Alternatively, one can adopt an implicit scheme for the transport terms, which leaps backwards in time and attempts to predict the quantities at the end of the timestep. Besides the transport terms, the source terms also need special treatments, since the temperature field or thermochemistry often needs to be solved simultaneously with the radiation field because they are strongly coupled together (Sekora & Stone 2010; Rosdahl et al. 2013; Jiang et al. 2012, 2014; Kannan et al. 2019; Jiang 2021). Those source terms can also be dealt with either explicitly with subcycling (e.g. Rosdahl et al. 2013; Zier et al. 2024a) or implicitly (e.g. Jiang et al. 2014; Kannan et al. 2019). Generally, implicit methods are conceptually more complex and require a more sophisticated scheme to perform well in parallel computing.

1.2. Objective: Towards a More Accurate General-purpose 3D Moving-mesh Radiation Magnetohydrodynamic Code

Besides accurate radiation transport, most complex astrophysical systems demand a wide range of length-scale and time-scale to be covered in one single simulation, which is often very challenging. In this work, we focus on the 3D moving-mesh MHD code AREPO (Springel 2010; Pakmor et al. 2011, 2016; Weinberger et al. 2020). It was initially designed for cosmological simulations of galaxy formation (e.g. IllustrisTNG; Springel et al. 2018; Pillepich et al. 2018; Nelson et al. 2018; Naiman et al. 2018; Marinacci et al. 2018). This was made possible largely due to the unique features of AREPO: (1) Voronoi mesh construction with arbitrary refinement and derefinement criterion; (2) Local time-stepping, where different parts of the simulation can take different timesteps according to local conditions, while conserving the total energy and momentum; (3) Moving-mesh, where the mesh follows the gas velocity in a quasi-Lagrangian way. These three features facilitate global 3D (M)HD simulations for astrophysical systems of arbitrary geometry involving highly supersonic flows and multi-scale resolutions both in space and time.

Therefore, besides galaxy formation, the AREPO code has also shown unique potentials in simulating other multi-scale systems sometimes with supersonic speeds, such as planet-disk interactions (Muñoz et al. 2014), disk instability and circumbinary disks (Zier & Springel 2022b, 2023; Muñoz et al. 2019;

Siwek et al. 2023), binary star interactions (Ohlmann et al. 2016; Schneider et al. 2019; Ryu et al. 2024a), neutron star mergers (Lioutas et al. 2024), type Ia and core-collapse supernovae (Pakmor et al. 2022; Chan et al. 2018), tidal disruption events (Goicovic et al. 2019; Ryu et al. 2024b; Vynatheya et al. 2024), star formation (Mocz et al. 2017; Mayer et al. 2024), multiphase gas (Sparre et al. 2019; Das et al. 2024), and AGN jets (Bourne & Sijacki 2017; Weinberger et al. 2017; Talbot et al. 2024). An extreme case of the vast length-scale AREPO can simulate within one single simulation is presented in Morán-Fraile et al. in prep., for double-detonated white dwarfs, covering a length-scale hierarchy of more than 6 orders of magnitude, comparable to the most radical simulations by GIZMO (Hopkins et al. 2024) or AthenaK (Guo et al. 2023). It is therefore promising to use AREPO as a general-purpose RMHD code to simulate the aforementioned problems, where radiation influences the multi-scale dynamics.

So far, there are multiple radiation transport modules implemented in AREPO, as summarized in the last row of Table 1. These include the semi-implicit source-dependent discrete ordinates method (Petkova & Springel 2011), explicit source-dependent ray-tracing method (Greif 2014), explicit short characteristics method (SPRAI; Jaura et al. 2018, 2020), explicit moment-based M1 closure (Bauer et al. 2015), semi-implicit moment-based M1 closure (AREPO-RT; Kannan et al. 2019; Zier et al. 2024a), and semi-implicit Monte-Carlo method (AREPO-MCRT; Smith et al. 2020). However, all of the current radiation transport modules in AREPO are specialized in ionizing radiation for either star formation or cosmological simulations, and therefore with thermochemistry often hard-coded to couple with radiation transport. This makes it difficult to use existing radiation modules to deal with general problems. Also, current implementations are not applicable for some problems, e.g. when there are too many radiation sources, intersecting radiation fronts, or radiation-dominated flows.

It is therefore clear that a new implementation is needed to push forward AREPO towards a general-purpose 3D moving-mesh RMHD code, where radiation transport is treated accurately in all regimes with minimal assumptions. In this paper, we aim to bridge this gap by introducing AREPO-IDORT, an implicit discrete ordinates radiation transport fully compatible with all the main features of AREPO. To this end, we generalize the implicit discrete ordinates radiation transport scheme developed by J21 for the 3D adaptive mesh refinement finite-volume code ATHENA++ (Stone et al. 2020). The reasons we choose this method are: (1) It produces accurate results across all optical depths; (2) It is fully implicit, and therefore does not suffer from artifacts introduced by the reduced speed of light approximation; (3) It exploits a finite-volume approach, which can be easily generalized to an unstructured mesh compared to e.g. ray-based methods; (4) It has been successfully applied to a wide range of problems, which aligns with our intention for a general-purpose code. Examples using the J21 method include, but are not limited to, planet formation (Zhu et al. 2021), protoplanetary disks (Zhang et al. 2024), stellar envelopes (Goldberg et al. 2022a), supernovae (Goldberg et al. 2022b), neutron star accretion (Zhang et al. 2022), tidal disruption events (Huang et al. 2023), AGN disks (Chen et al. 2023), and circumbinary disks (Tiwari et al. 2025).

We improve the scheme by J21 in multiple aspects by supporting: (1) an unstructured moving mesh, (2) local time-stepping, and (3) general equations of state. Our scheme also achieves fast performance. In Section 2, we derive the radiation transport equations from first principles with minimal as-

sumptions. We describe the grey radiation transport scheme in Section 3, where we summarize the flow of our scheme in Section 3.4 for direct usage. In Section 4, we present extensive test problems covering all regimes of optical thickness and dominant energy content, with a special focus on the performance of the scheme on an unstructured moving mesh with local time-stepping. We then show a global 3D radiation hydrodynamic model of a red supergiant star in Section 5, which for the first time covers the entire convective envelope while resolving the radiation flux near the photosphere. Finally, we discuss the caveats of our scheme and future plans to improve and generalize it further in Section 6. We summarize and conclude in Section 7 and point out additional possible applications of our new scheme in different fields of astrophysics that only very few existing codes can simulate efficiently.

2. Basic Equations

In this section, we review the equations involved in the radiation transport processes. We first state the general forms of radiation transport equations in Section 2.1. Then in Section 2.2, assuming isotropic scattering and a Planck source function, we derive the radiation transport equations used to develop our scheme. Radiation is coupled to the total energy and momentum of the system, along with the MHD and gravitational processes. Therefore, we describe the equations of RMHD in Section 2.3.

2.1. General Equations of Radiation Transport

The general form of radiation transport equation is

$$\frac{\partial I_\nu}{\partial t} + c\mathbf{n} \cdot \nabla I_\nu = c(\eta_\nu - \chi_\nu I_\nu), \quad (1)$$

where I_ν is the specific intensity at the frequency ν along the direction given by the unit vector \mathbf{n} , t the time, and c the speed of light. The emissivity η_ν and the extinction coefficient χ_ν here are defined in the rest frame. Adopting the convention that the source function is $S_\nu \equiv \eta_\nu/\chi_\nu$ and the opacity is $\kappa_\nu \equiv \chi_\nu/\rho$ where ρ is the fluid density, this equation can be written as

$$\frac{\partial I_\nu}{\partial t} + c\mathbf{n} \cdot \nabla I_\nu = c\rho\kappa_\nu(S_\nu - I_\nu). \quad (2)$$

Since the source function and the opacity are often given in the frame comoving with the fluid at a velocity \mathbf{v} , it is natural to convert quantities to the comoving frame (denoted with a prime \prime) by the Lorentz transformation (Mihalas & Mihalas 1984)

$$I'_\nu(\mathbf{n}') = \Gamma^3 I_\nu(\mathbf{n}), \quad (3)$$

$$S'_\nu = \Gamma^3 S_\nu, \quad (4)$$

$$\kappa'_\nu = \Gamma^{-1} \kappa_\nu, \quad (5)$$

$$\nu' = \Gamma \nu, \quad (6)$$

$$\mathbf{n}' = \Gamma^{-1} \left(\mathbf{n} - \frac{1 + \Gamma}{1 + \gamma} \gamma \boldsymbol{\beta} \right), \quad (7)$$

where

$$\Gamma(\mathbf{n}, \mathbf{v}) \equiv \gamma(1 - \mathbf{n} \cdot \boldsymbol{\beta}), \quad (8)$$

$$\gamma = 1/\sqrt{1 - \beta^2}, \quad (9)$$

$$\boldsymbol{\beta} = \mathbf{v}/c. \quad (10)$$

Therefore, the radiation transport equation in a mixed-frame expression reads

$$\frac{\partial I_\nu}{\partial t} + c\mathbf{n} \cdot \nabla I_\nu = c\rho\kappa'_\nu\Gamma^{-2}(S'_\nu - I'_\nu). \quad (11)$$

The zeroth-, first-, and second-moment of I_ν are related to the radiation energy density, radiation flux, and radiation pressure tensor per frequency via

$$E_\nu \equiv \frac{1}{c} \int I_\nu d\Omega, \quad (12)$$

$$\mathbf{F}_\nu \equiv \int I_\nu \mathbf{n} d\Omega, \quad (13)$$

$$\mathbf{P}_\nu \equiv \frac{1}{c} \int I_\nu \mathbf{n} \mathbf{n} d\Omega, \quad (14)$$

where Ω is the solid angle. Their counterparts in the comoving frame are

$$E'_\nu \equiv \frac{1}{c} \int I'_\nu d\Omega', \quad (15)$$

$$\mathbf{F}'_\nu \equiv \int I'_\nu \mathbf{n}' d\Omega', \quad (16)$$

$$\mathbf{P}'_\nu \equiv \frac{1}{c} \int I'_\nu \mathbf{n}' \mathbf{n}' d\Omega', \quad (17)$$

where

$$d\Omega' = \Gamma^{-2} d\Omega. \quad (18)$$

Taking the zeroth- and first-moment of the radiation transport equation (11), we obtain

$$\frac{\partial}{\partial t} E_\nu + c\mathbf{v} \cdot \frac{\mathbf{F}_\nu}{c} = \rho \int [\kappa'_\nu(S'_\nu - I'_\nu)] d\Omega', \quad (19)$$

$$\frac{\partial}{\partial t} \frac{\mathbf{F}_\nu}{c} + c\mathbf{v} \cdot \mathbf{P}_\nu = \rho \int [\kappa'_\nu(S'_\nu - I'_\nu)] \mathbf{n} d\Omega'. \quad (20)$$

The frequency-integrated quantities are defined as

$$I = \int I_\nu d\nu, \quad (21)$$

$$E_\tau = \int E_\nu d\nu, \quad (22)$$

$$\mathbf{F}_\tau = \int \mathbf{F}_\nu d\nu, \quad (23)$$

$$\mathbf{P}_\tau = \int \mathbf{P}_\nu d\nu. \quad (24)$$

By integrating over the frequency, the radiation transport equation and the moment equations become

$$\frac{\partial I}{\partial t} + c\mathbf{n} \cdot \nabla I = c\rho\Gamma^{-3} \int [\kappa'_\nu(S'_\nu - I'_\nu)] d\nu', \quad (25)$$

$$\frac{\partial}{\partial t} E_\tau + c\mathbf{v} \cdot \frac{\mathbf{F}_\tau}{c} = \rho \int \left\{ \int [\kappa'_\nu(S'_\nu - I'_\nu)] d\nu' \right\} \Gamma^{-1} d\Omega', \quad (26)$$

$$\frac{\partial}{\partial t} \frac{\mathbf{F}_\tau}{c} + c\mathbf{v} \cdot \mathbf{P}_\tau = \rho \int \left\{ \int [\kappa'_\nu(S'_\nu - I'_\nu)] d\nu' \right\} \Gamma^{-1} \mathbf{n} d\Omega'. \quad (27)$$

2.2. Radiation Transport Equations under Assumptions

For the rest of this work, we assume:

1. Isotropic and coherent scattering in the comoving frame;
2. The source function is the Planck function;
3. The fluid is moving at non-relativistic speed ($\beta \ll 1$).

Under the first two assumptions, the source terms on the right hand sides of the equations can be further expressed in terms of scattering opacity $\kappa'_{\nu',s}$, absorption opacity $\kappa'_{\nu',a}$, Planck function $B'_{\nu'}$, and the zeroth moment

$$J'_{\nu'} = \int I'_{\nu'} d\Omega' / (4\pi) = cE'_{\nu'} / (4\pi), \quad (28)$$

which gives

$$\frac{\partial I}{\partial t} + c\mathbf{n} \cdot \nabla I = c\rho\Gamma^{-3} \int \left[\kappa'_{\nu',s}(J'_{\nu'} - I'_{\nu'}) + \kappa'_{\nu',a}(B'_{\nu'} - I'_{\nu'}) \right] d\nu', \quad (29)$$

$$\frac{\partial}{\partial t} E_{\mathbf{r}} + c\mathbf{\nabla} \cdot \frac{\mathbf{F}_{\mathbf{r}}}{c} = \rho \int \left[(\kappa'_{\nu',s} J'_{\nu'} + \kappa'_{\nu',a} B'_{\nu'}) \int \Gamma^{-1} d\Omega' - (\kappa'_{\nu',s} + \kappa'_{\nu',a}) \left(\int I'_{\nu'} \Gamma^{-1} d\Omega' \right) \right] d\nu', \quad (30)$$

$$\frac{\partial}{\partial t} \frac{\mathbf{F}_{\mathbf{r}}}{c} + c\mathbf{\nabla} \cdot \mathbf{P}_{\mathbf{r}} = \rho \int \left[(\kappa'_{\nu',s} J'_{\nu'} + \kappa'_{\nu',a} B'_{\nu'}) \int \Gamma^{-1} \mathbf{n} d\Omega' - (\kappa'_{\nu',s} + \kappa'_{\nu',a}) \left(\int I'_{\nu'} \Gamma^{-1} \mathbf{n} d\Omega' \right) \right] d\nu'. \quad (31)$$

Here, the Planck function is

$$B'_{\nu'} = \frac{2h\nu'^3}{c^2} \frac{1}{\exp(h\nu'/k_{\text{B}}T) - 1}, \quad (32)$$

where h is the Planck constant, k_{B} is the Boltzmann constant, and T is the local gas temperature. Assuming that the fluid is moving at non-relativistic speed ($\beta \ll 1$), we can expand the integral over directions as

$$\begin{aligned} \int \Gamma^{-1} d\Omega' &= \int \Gamma^{-3} d\Omega \\ &= \int [1 + 3\mathbf{n} \cdot \boldsymbol{\beta} + 6(\mathbf{n} \cdot \boldsymbol{\beta})^2 - 3\beta^2/2 + O(\beta^3)] d\Omega \\ &= 4\pi(1 + \beta^2/2) + O(\beta^3), \end{aligned} \quad (33)$$

$$\int \Gamma^{-1} \mathbf{n} d\Omega' = \int \Gamma^{-3} \mathbf{n} d\Omega = 4\pi\boldsymbol{\beta} + O(\beta^3), \quad (34)$$

$$\int I'_{\nu'} \Gamma^{-1} d\Omega' = 4\pi J'_{\nu'} (1 + \beta^2/2) + \boldsymbol{\beta} \cdot \mathbf{F}'_{\nu'} + O(J'_{\nu'} \beta^3), \quad (35)$$

$$\int I'_{\nu'} \Gamma^{-1} \mathbf{n} d\Omega' = \mathbf{F}'_{\nu'} + 4\pi J'_{\nu'} \boldsymbol{\beta} + O(J'_{\nu'} \beta^2). \quad (36)$$

To the second order of β for the energy, these yield

$$\frac{\partial}{\partial t} E_{\mathbf{r}} + c\mathbf{\nabla} \cdot \frac{\mathbf{F}_{\mathbf{r}}}{c} = \rho \int \left[\kappa'_{\nu',a} 4\pi(B'_{\nu'} - J'_{\nu'}) (1 + \beta^2/2) - (\kappa'_{\nu',s} + \kappa'_{\nu',a}) \boldsymbol{\beta} \cdot \mathbf{F}'_{\nu'} \right] d\nu', \quad (37)$$

$$\frac{\partial}{\partial t} \frac{\mathbf{F}_{\mathbf{r}}}{c} + c\mathbf{\nabla} \cdot \mathbf{P}_{\mathbf{r}} = \rho \int \left[\kappa'_{\nu',a} 4\pi(B'_{\nu'} - J'_{\nu'}) \boldsymbol{\beta} - (\kappa'_{\nu',s} + \kappa'_{\nu',a}) \mathbf{F}'_{\nu'} \right] d\nu', \quad (38)$$

and the Lorentz transformations of the radiation quantities give

$$\begin{aligned} E'_{\mathbf{r}} &= \frac{1}{c} \int \int I'_{\nu'} d\Omega' d\nu' = \frac{1}{c} \int \int \Gamma^2 I_{\nu} d\Omega d\nu \\ &= (1 + \beta^2) E_{\mathbf{r}} - 2\boldsymbol{\beta} \cdot \frac{\mathbf{F}_{\mathbf{r}}}{c} + \boldsymbol{\beta} \cdot \boldsymbol{\beta} \cdot \mathbf{P}_{\mathbf{r}} + O(E_{\mathbf{r}} \beta^3), \end{aligned} \quad (39)$$

$$\begin{aligned} \frac{\mathbf{F}'_{\mathbf{r}}}{c} &= \frac{1}{c} \int \int I'_{\nu'} \mathbf{n}' d\Omega' d\nu' = \frac{1}{c} \int \int \Gamma I_{\nu} \left(\mathbf{n} - \frac{1 + \Gamma}{1 + \gamma} \boldsymbol{\beta} \right) d\Omega d\nu \\ &= \frac{\mathbf{F}_{\mathbf{r}}}{c} - \boldsymbol{\beta} E_{\mathbf{r}} - \boldsymbol{\beta} \cdot \mathbf{P}_{\mathbf{r}} + O(E_{\mathbf{r}} \beta^2). \end{aligned} \quad (40)$$

By defining the frequency-integrated opacities

$$\kappa_{\text{P}} \equiv \frac{\int \kappa'_{\nu',a} B'_{\nu'} d\nu'}{\int B'_{\nu'} d\nu'}, \quad (41)$$

$$\kappa_{\text{E}} \equiv \frac{\int \kappa'_{\nu',a} E'_{\nu'} d\nu'}{\int E'_{\nu'} d\nu'}, \quad (42)$$

$$\kappa_{\text{F},i} \equiv \frac{\int \kappa'_{\nu',a} F'_{\nu',i} d\nu'}{\int F'_{\nu',i} d\nu'}, \quad i = 1, 2, 3, \quad (43)$$

$$\kappa_{\text{F},s,i} \equiv \frac{\int \kappa'_{\nu',s} F'_{\nu',i} d\nu'}{\int F'_{\nu',i} d\nu'}, \quad i = 1, 2, 3, \quad (44)$$

the moment equations become

$$\frac{\partial}{\partial t} E_{\mathbf{r}} + c\mathbf{\nabla} \cdot \frac{\mathbf{F}_{\mathbf{r}}}{c} = \rho \left\{ (\kappa_{\text{P}} 4\pi B' - \kappa_{\text{E}} c E'_{\mathbf{r}}) (1 + \beta^2/2) \right. \quad (45)$$

$$\left. - \boldsymbol{\beta} \cdot [(\kappa_{\text{F}} + \kappa_{\text{F},s}) \odot \mathbf{F}'_{\mathbf{r}}] \right\},$$

$$\frac{\partial}{\partial t} \frac{\mathbf{F}_{\mathbf{r}}}{c} + c\mathbf{\nabla} \cdot \mathbf{P}_{\mathbf{r}} = \rho \left\{ (\kappa_{\text{P}} 4\pi B' - \kappa_{\text{E}} c E'_{\mathbf{r}}) \boldsymbol{\beta} \right. \quad (46)$$

$$\left. - [(\kappa_{\text{F}} + \kappa_{\text{F},s}) \odot \mathbf{F}'_{\mathbf{r}}] \right\},$$

where $\mathbf{A} \odot \mathbf{B}$ is the element-wise Hadamard product of vectors \mathbf{A} and \mathbf{B} , and

$$B' = \int B'_{\nu'} d\nu' = \frac{caT^4}{4\pi}. \quad (47)$$

Here, $a = 8\pi^5 k_{\text{B}}^4 / (15c^3 h^3)$ is the radiation constant.

We further assume that

$$\kappa_{\text{F},i} \approx \kappa_{\text{F}}, \quad \kappa_{\text{F},s,i} \approx \kappa_{\text{s}}, \quad i = 1, 2, 3, \quad (48)$$

where κ_{s} is the scattering opacity. These assumptions only hold when the radiative fluxes of different frequencies are pointing to the same direction. For a general case, better treatment of opacities are needed, e.g., multigroup or direct frequency-dependent calculations.

In the optically thick regime where local thermal equilibrium (LTE) and radiative diffusion are good approximations, the energy-weighted opacity equals to the Planck mean opacity and the flux-weighted opacity equals to the Rosseland mean opacity, i.e., $\kappa_{\text{E}} \approx \kappa_{\text{P}}$ and $\kappa_{\text{F}} \approx \kappa_{\text{R}}$, where

$$\kappa_{\text{R}} \equiv \left[\frac{\int \kappa'_{\nu',a}{}^{-1} (\partial B'_{\nu'} / \partial T) d\nu'}{\int (\partial B'_{\nu'} / \partial T) d\nu'} \right]^{-1}, \quad (49)$$

is the Rosseland opacity. However, we develop the scheme for a more generalized scenario here, and therefore do not make such assumption.

The moment equations then read

$$\frac{\partial}{\partial t} E_r + c \nabla \cdot \frac{\mathbf{F}_r}{c} \quad (50)$$

$$= \rho \left[(\kappa_P 4\pi B' - \kappa_E c E_r') (1 + \beta^2/2) - (\kappa_F + \kappa_s) \boldsymbol{\beta} \cdot \mathbf{F}_r' \right],$$

$$\frac{\partial}{\partial t} \frac{\mathbf{F}_r}{c} + c \nabla \cdot \mathbf{P}_r = \rho \left[(\kappa_P 4\pi B' - \kappa_E c E_r') \boldsymbol{\beta} - (\kappa_F + \kappa_s) \mathbf{F}_r' \right]. \quad (51)$$

Based on the structure of these equations, it is then evident that in order to arrive at the same moment equations, the frequency-integrated radiation transport equation is

$$\frac{\partial I}{\partial t} + c \mathbf{n} \cdot \nabla I = c S_I, \quad (52)$$

$$S_I = \rho \Gamma^{-3} \left[(\kappa_P B' - \kappa_E J') + (\kappa_F + \kappa_s) (J' - I') \right]. \quad (53)$$

For numerical schemes, it is more useful to express the source terms in the rest frame. Plugging in the transformations of radiation energy density and radiation flux, we arrive at the final form of the moment equations

$$\frac{\partial}{\partial t} E_r + c \nabla \cdot \frac{\mathbf{F}_r}{c} = S_{r,E}, \quad (54)$$

$$\frac{\partial}{\partial t} \frac{\mathbf{F}_r}{c} + c \nabla \cdot \mathbf{P}_r = c S_{r,p}, \quad (55)$$

where

$$\begin{aligned} S_{r,E} &= \int S_I d\Omega \\ &= c\rho \left\{ \left[\left(\kappa_P \frac{4\pi B'}{c} - \kappa_E E_r' \right) (1 + \beta^2/2) + \kappa_E \boldsymbol{\beta} \cdot \frac{\mathbf{F}_r'}{c} \right] \right. \\ &\quad \left. - (\kappa_F + \kappa_s - \kappa_E) \boldsymbol{\beta} \cdot \left(\frac{\mathbf{F}_r'}{c} - \boldsymbol{\beta} E_r' - \boldsymbol{\beta} \cdot \mathbf{P}_r' \right) + O(\kappa E_r \beta^3) \right\}, \end{aligned} \quad (56)$$

$$\begin{aligned} S_{r,p} &= \frac{1}{c} \int S_I \mathbf{n} d\Omega \\ &= \rho \left[\left(\kappa_P \frac{4\pi B'}{c} - \kappa_E E_r' \right) \boldsymbol{\beta} \right. \\ &\quad \left. - (\kappa_F + \kappa_s) \left(\frac{\mathbf{F}_r'}{c} - \boldsymbol{\beta} E_r' - \boldsymbol{\beta} \cdot \mathbf{P}_r' \right) + O(\kappa E_r \beta^2) \right]. \end{aligned} \quad (57)$$

We note that those two moment equations cannot be solved alone, since there are three variables in only two equations. A closure relation between E_r and \mathbf{P}_r (or an effective ‘equation of state’ for radiation) must be provided to solve the moment equations, which is the essence of moment-based radiation transport methods. The radiation source terms derived here are consistent with those derived in [Krumholz et al. \(2007\)](#), but are slightly different from those documented in VET schemes ([Jiang et al. 2012](#); [Menon et al. 2022](#)). Based on the scaling argument in [Krumholz et al. \(2007\)](#), it is important to keep all the second order terms, and we recommend to use these source terms in the future development of the VET scheme.

2.3. Equations of Radiation Ideal Magnetohydrodynamics

The Euler equations of radiation ideal MHD can be written as

$$\frac{\partial}{\partial t} \mathbf{U} + \nabla \cdot \mathbf{F} = \mathbf{S}, \quad (58)$$

where the conserved quantities, their associated fluxes, and source terms are

$$\begin{aligned} \mathbf{U} &= \begin{pmatrix} \rho \\ \rho \mathbf{v} + \mathbf{F}_r/c^2 \\ E^* + E_r \end{pmatrix}, \quad \mathbf{F} = \begin{pmatrix} \rho v \\ \rho \mathbf{v} \mathbf{v} + \mathbf{P}^* - \mathbf{B} \mathbf{B} + \mathbf{P}_r \\ (E^* + P^*) \mathbf{v} - \mathbf{B}(\mathbf{v} \cdot \mathbf{B}) + \mathbf{F}_r \end{pmatrix}, \\ \mathbf{S} &= \begin{pmatrix} 0 \\ -\rho \nabla \Phi \\ -\rho \mathbf{v} \cdot \nabla \Phi \end{pmatrix}. \end{aligned} \quad (59)$$

Here, \mathbf{B} is the magnetic field, Φ is the gravitational potential, $E^* = E_g + \rho v^2/2 + B^2/2$ is the total MHD energy density, $\mathbf{P}^* = (P_g + B^2/2)\mathbf{I}$ is the total MHD pressure, where E_g and P_g are the internal energy density and gas pressure. This set of equations, coupled with the induction equation

$$\frac{\partial}{\partial t} \mathbf{B} - \nabla \times (\mathbf{v} \times \mathbf{B}) = 0 \quad (60)$$

and the radiation transport equation, form the system of radiation ideal MHD.

For the numerical methods, it is more useful to separate the radiation terms as radiation source terms $S_{r,E}$ and $S_{r,p}$ (equations (56) and (57)), such that the conserved quantities, fluxes, and source terms are

$$\mathbf{U} = \begin{pmatrix} \rho \\ \rho \mathbf{v} \\ E^* \end{pmatrix}, \quad \mathbf{F} = \begin{pmatrix} \rho v \\ \rho \mathbf{v} \mathbf{v} + \mathbf{P}^* - \mathbf{B} \mathbf{B} \\ (E^* + P^*) \mathbf{v} - \mathbf{B}(\mathbf{v} \cdot \mathbf{B}) \end{pmatrix}, \quad \mathbf{S} = \begin{pmatrix} 0 \\ -\rho \nabla \Phi - S_{r,p} \\ -\rho \mathbf{v} \cdot \nabla \Phi - S_{r,E} \end{pmatrix}. \quad (61)$$

3. Implicit Discrete Ordinates Solver

Implicit time integration allows the radiation solver to evolve the radiation field at a timestep not limited by the speed of light. This is at the expense of losing the short-timescale physics between the large timesteps, which is typically acceptable if the radiation varies at a timescale at least comparable to the dynamical timescale. The radiation transport equations, either in the angle-dependent form (52) or the moment form (54), (55), are linear in radiation quantities. This suggests that the radiation quantities in all the cells can be grouped into a vector, and the radiation transport equations form a linear solver involving a large sparse matrix. However, the radiation source term in the energy equation can be stiff ([Sekora & Stone 2010](#); [Jiang et al. 2012](#)), such that the gas temperature has to be evolved simultaneously with the radiation quantities by calculating the change in the internal energy density due to the radiation source terms

$$\begin{aligned} \frac{\partial}{\partial t} E_g &= -S_r + \mathbf{v} \cdot \mathbf{S}_r - \frac{1}{2} S_r \cdot \mathbf{S}_r = -\frac{1}{\gamma} \int S_I \Gamma d\Omega - \frac{1}{2} S_r \cdot \mathbf{S}_r \\ &= -c\rho \left(\kappa_P \frac{4\pi B'}{c} - \kappa_E E_r' \right) + O(\kappa E_r \beta^3). \end{aligned} \quad (62)$$

Both the internal energy density of the gas and the Planck function are non-linear functions of the gas temperature. Therefore, the equations are linear in radiation quantities but non-linear in gas temperature. For this work, we adopt an iterative solver to solve for the intensities based on [J21](#), and use the Newton-Raphson method to solve for the gas temperature. The scheme described here is only first-order accurate both in time and

space, as in (J21). This is because higher-order spatial reconstruction requires flux limiters to avoid oscillatory behavior, but flux limiters render the transport term non-linear, which is very difficult to solve implicitly (J21). Also, stiff source terms can be difficult to treat with higher-order implicit time integration (Sekora & Stone 2010; Jiang et al. 2012; Jiang 2021).

The implicit discrete-ordinate radiation transport described in this paper is based on the method in J21 implemented in ATHENA++ (Stone et al. 2020). This method solves for the specific intensities along discrete angles. It exploits the finite-volume approach, which makes the method particularly suitable for unstructured meshes. We extend the scheme to be fully compatible with the features of AREPO (Springel 2010; Pakmor et al. 2016; Weinberger et al. 2020): unstructured moving mesh with local time-stepping and general EOS. We first review the discretization (Section 3.1 and 3.2) and the derivation of the equations for the iterative solver with local time-stepping (Section 3.3). We present the detailed scheme in Section 3.4. Then we describe the source terms to be coupled back to the AREPO MHD solver (Section 3.5). We also briefly describe some optional features for the users to choose and experiment with (Section 3.6).

3.1. Discretization in Space, Time, and Angular Space

To numerically integrate the equations, all the radiation transport equations are discretized in space, time, and solid angle. We perform the radiation transport calculations on the same Voronoi mesh as the AREPO MHD solver uses, but the method applies to arbitrary meshes. For the Voronoi mesh, the cells are labeled in a 1D sequence. The specific intensities are defined at the volume center of each cell. The numbers of active cells and of directions are denoted as N_p and N_Ω , respectively. For the spatial discretization, the subscript i indicates the quantities of the active cell $i \in [0, N_p - 1]$. The i^{th} cell has N_i neighboring cells. Among those neighboring cells, the j^{th} cell is denoted by the subscript $j \in [0, N_i - 1]$. For local time-stepping, we further divide those N_i neighboring cells into \tilde{N}_i active cells and M_i passive cells, such that $N_i = \tilde{N}_i + M_i$. The active cells are cells holding the local timestep. The passive cells are cells with larger local timesteps and therefore the primitive variables are not updated in those cells. We use the subscript ij to indicate the quantities at the face between cell i and j . For angular discretization, the subscript $n \in [0, N_\Omega - 1]$ indicates the n^{th} direction among the 4π solid angles. For temporal discretization, we use the superscript m to indicate the primitive variables at the end of the last active timestep, and $m + 1$ as the primitive variables at the end of the current active timestep. For local time-stepping, the last active timestep is different for different cells.

We use the same angular discretization as the implementation in ATHENA++ (Davis et al. 2012; Jiang et al. 2014; Jiang 2021). The unit vector along each direction $\mathbf{n}_n = ((n_x)_n, (n_y)_n, (n_z)_n)$ is defined with respect to the (x, y, z) coordinates. Each direction is assigned a weight w_n for integrated quantities. We keep the weights fixed for all the cells and throughout the simulation. The angular discretization scheme is based on Bruls et al. (1999). The scheme guarantees that when the radiation field is isotropic, the radiation flux is strictly zero and the Eddington tensor $\mathbf{f}_{\text{Edd}} \equiv \mathbf{P}_r/E_r$ is strictly $1/3$ the unit matrix,

namely

$$\sum_{n=0}^{N_\Omega-1} w_n = 1, \quad (63)$$

$$\sum_{n=0}^{N_\Omega-1} (n_x)_n w_n = \sum_{n=0}^{N_\Omega-1} (n_y)_n w_n = \sum_{n=0}^{N_\Omega-1} (n_z)_n w_n = 0, \quad (64)$$

$$\sum_{n=0}^{N_\Omega-1} (n_x)_n^2 w_n = \sum_{n=0}^{N_\Omega-1} (n_y)_n^2 w_n = \sum_{n=0}^{N_\Omega-1} (n_z)_n^2 w_n = \frac{1}{3}. \quad (65)$$

This angular discretization ensures that each octant has $k(k+1)/2$ directions, where k is an arbitrary integer. The total number of angles can only take specific values as $4k(k+1)$, that is 8, 24, 48, 80, 120, etc. Therefore, although the Voronoi mesh does not have preferred directions, the discretized radiation field has, especially if only a small number of angles is chosen. It is generally recommended to choose a number of angles above 48 for 3D simulations to obtain a decent coverage of the sphere and to avoid ray-effects (i.e., peaks along the discretized directions in radiation and temperature fields due to the small number of directions selected; Huang et al. 2023; Zhang et al. 2024, see also our Figure 16). Based on the Lorentz transformation of the solid angle, we have $(w')_{n,i}^m = (\Gamma_{n,i}^m)^{-2} w_n$. However, as noted in J21, the normalization $\sum_{n=0}^{N_\Omega-1} (w')_{n,i}^m = 1$ is typically not satisfied to machine precision. This is corrected by

$$(w')_{n,i}^m = \frac{(\Gamma_{n,i}^m)^{-2} w_n}{\sum_{n=0}^{N_\Omega-1} (\Gamma_{n,i}^m)^{-2} w_n}. \quad (66)$$

We note that although the weight w_n in the lab frame does not depend on space and time, the weight $(w')_{n,i}^m$ in the comoving frame does, since the Lorentz factor depends on space and time.

We calculate the radiation energy density, radiation flux, and radiation pressure tensor by

$$(E_r)_i^{m+1} = \frac{4\pi}{c} \sum_{n=0}^{N_\Omega-1} I_{n,i}^{m+1} w_n, \quad (67)$$

$$(\mathbf{F}_r)_i^{m+1} = 4\pi \sum_{n=0}^{N_\Omega-1} I_{n,i}^{m+1} \mathbf{n}_n w_n, \quad (68)$$

$$(\mathbf{P}_r)_i^{m+1} = \frac{4\pi}{c} \sum_{n=0}^{N_\Omega-1} I_{n,i}^{m+1} \mathbf{n}_n \mathbf{n}_n w_n. \quad (69)$$

3.2. Discretized Equations

In a moving-mesh code with refinement and local time-stepping such as AREPO, it is essential to distinguish between the conserved quantities and primitive variables. We only update the primitive variables of the cell when the cell is active (i.e. synchronised), but the conserved quantities are always updated when they exchange fluxes with the neighboring cells. Here, we use (IV) as the conserved quantity corresponding to the primitive variable I . The conserved form of the discretized radiation transport equation can be written as

$$\begin{aligned} [I_n^{m+1} V^m - (IV)_n^m]_i = & - \sum_{j=0}^{N_i-1} [I_n(c\mathbf{n}_n - \mathbf{u})]_{ij}^{m+1} \cdot \mathbf{A}_{ij}^m \Delta t_{ij}^m \\ & + [(S_I)_n^{m+1} V^m c \Delta t^m]_i, \end{aligned} \quad (70)$$

where A_{ij} , $\Delta t_{ij} = \min(\Delta t_i, \Delta t_j)$ and \mathbf{u}_{ij} are the normal area vector, minimum timestep and the face velocity between cell i and j . The local timesteps are limited by the local MHD CFL condition and grouped into a power-of-two hierarchy (Springel 2010). For a fixed-mesh code, $\mathbf{u}_{ij} = 0$. For a code that uses global timesteps, we have $\Delta t_{ij}^m = \Delta t_i^m = \Delta t^m$. Here, V_i is the volume of the cell i , and the implicit source term is

$$(S_I)_{n,i}^{m+1} = (\rho \Gamma_n^{-3})_i^m \left[(\kappa_P)_i^m (B')_i^{m+1} - (\kappa_E)_i^m (J')_i^{m+1} + (\kappa_F + \kappa_s)_i^m (J' - I'_n)^{m+1} \right]. \quad (71)$$

The first moment of the specific intensities is discretized as

$$J' = \sum_{n=0}^{N_\Omega-1} I'_n w'_n, \quad (72)$$

where the specific intensities in the comoving frame are related to their counterparts in the lab frame via the Lorentz transformation

$$I'_n = \Gamma_n^4 I_n. \quad (73)$$

We do not separate the gas velocity advection term from the total transport term as in J21, because we find that the separation leads to unstable behavior with local time-stepping.

The discretized update to the specific gas internal energy is

$$(e_g^{m+1} - e_g^m)_i = -4\pi \left[\Delta t^m (\kappa_P^m B'^{m+1} - \kappa_E^m J'^{m+1}) \right]_i, \quad (74)$$

where $e_g^{m+1} = E_g^{m+1}/\rho^m = e_g(\rho^m, T^{m+1})$ and $B'^{m+1} = B'(T^{m+1})$. By coupling these two implicit equations together, we solve for the radiation field and the temperature field simultaneously. All the other physical quantities are kept unchanged from the last timestep. Specifically, the opacities are not solved implicitly. This is to ensure convergence and to avoid oscillatory behavior from the highly non-linear dependence of opacities on temperature. For passive cells, only the conserved radiation quantities (I_V) are changed, and all the other MHD quantities (e.g. temperature, internal energy, total energy, total momentum) are only updated by the next time the passive cells become active again.

3.3. Derivation of the Equations for the Iterative Solver

Let us focus on the specific intensity along one direction in one cell. It only depends on the other physical quantities of the cell, the specific intensities of the cell along other directions, and the specific intensities in neighboring cells along this direction. The iterative solver is constructed such that the specific intensities along this direction in neighboring cells are kept unchanged after the last iteration, in order to update the specific intensities along all directions in the target cell in the current iteration.

Specifically, the iterated equation is derived as follows. First, we consider the transport terms. The implicit transport term in the radiation transport equation is a linear combination of the specific intensities in the target cell and in neighboring cells. Therefore, it can be written as

$$\begin{aligned} & \left\{ \sum_{j=0}^{N_i-1} [I_n(c\mathbf{n}_n - \mathbf{u})]_{ij}^{m+1} \cdot \mathbf{A}_{ij}^m \Delta t_{ij}^m \right\} / V_i^m \\ & = \left(\sum_{j=0}^{N_i-1} C_{n,ij}^m \right) I_{n,i}^{m+1} + \left(\sum_{j=0}^{\tilde{N}_i-1} D_{n,ij}^m I_{n,j}^{m+1} \right) + \left(\sum_{j=0}^{M_i-1} D_{n,ij}^m I_{n,j}^m \right), \end{aligned}$$

where the coefficients C and D only depend on the grid configuration and the Riemann solver. The last two terms on the right hand side are separated according to whether the neighboring cell is active or not.

These coefficients in the transport terms are calculated by a modified HLLC solver as proposed by J21 based on Sekora & Stone (2010), where

$$\begin{aligned} [I_n(c\mathbf{n}_n - \mathbf{u})]_{ij}^{m+1} \cdot \boldsymbol{\mu}_{ij}^m & = \left(\frac{S^+}{S^+ - S^-} \right)_{n,ij}^m I_{n,i}^{m+1} (c\mathbf{n}_n - \mathbf{u}_{ij}^m) \cdot \boldsymbol{\mu}_{ij}^m \\ & - \left(\frac{S^-}{S^+ - S^-} \right)_{n,ij}^m I_{n,j}^{m+1} (c\mathbf{n}_n - \mathbf{u}_{ij}^m) \cdot \boldsymbol{\mu}_{ij}^m \\ & + \left(\frac{S^+ S^-}{S^+ - S^-} \right)_{n,ij}^m [I_j - I_i]_n^{m+1}. \end{aligned} \quad (75)$$

Here, \mathbf{u}_{ij}^m is the face velocity of the moving mesh calculated in the AREPO MHD finite-volume solver. The unit vector $\boldsymbol{\mu}_{ij}^m$ is normal to the face pointing from cell i to cell j , obtained from the Voronoi mesh construction. The maximum and minimum signal speeds are

$$(S^+)_{n,ij}^m = \begin{cases} c \left| \mathbf{n}_n \cdot \boldsymbol{\mu}_{ij}^m \right| \sqrt{\{1 - \exp[-(\tau_{ij}^m)^2]\}} / (\tau_{ij}^m)^2, & \mathbf{n}_n \cdot \boldsymbol{\mu}_{ij}^m \geq 0, \\ c \left| \mathbf{n}_n \cdot \boldsymbol{\mu}_{ij}^m \right| \sqrt{\{1 - \exp[-(\tau_{ij}^m)^4]\}} / (\tau_{ij}^m)^2, & \mathbf{n}_n \cdot \boldsymbol{\mu}_{ij}^m < 0, \end{cases} \quad (77)$$

$$(S^-)_{n,ij}^m = \begin{cases} -c \left| \mathbf{n}_n \cdot \boldsymbol{\mu}_{ij}^m \right| \sqrt{\{1 - \exp[-(\tau_{ij}^m)^4]\}} / (\tau_{ij}^m)^2, & \mathbf{n}_n \cdot \boldsymbol{\mu}_{ij}^m \geq 0, \\ -c \left| \mathbf{n}_n \cdot \boldsymbol{\mu}_{ij}^m \right| \sqrt{\{1 - \exp[-(\tau_{ij}^m)^2]\}} / (\tau_{ij}^m)^2, & \mathbf{n}_n \cdot \boldsymbol{\mu}_{ij}^m < 0. \end{cases} \quad (78)$$

This definition is designed to reduce the simple signal speed $c \left| \mathbf{n}_n \cdot \boldsymbol{\mu}_{ij}^m \right|$ by a factor of τ_{ij}^m in the optically thick limit while approaching an upwind flux in the optically thin limit (J21). Here, the effective optical depth at the face is defined as

$$\tau_{ij}^m = \alpha \rho_{ij}^m (\kappa_F + \kappa_s)_{ij}^m \Delta R_{ij}^m, \quad (79)$$

where α is a numerical parameter taken as $\alpha = 5$ by default (J21). All the face values on the right hand side of this equation are calculated as the average of the two values in i and j cells, namely $q_{ij}^m = (q_i^m + q_j^m)/2$. The effective cell radius is converted from the cell volume, namely $\Delta R_i^m = [3V_i^m/(4\pi)]^{1/3}$. We note that the cell 'volume' is different in 1D and 2D cases. Therefore, the coefficients are

$$\begin{aligned} C_{n,ij}^m & = \left(\frac{S^+}{S^+ - S^-} \right)_{n,ij}^m [(c\mathbf{n}_n - \mathbf{u}_{ij}^m) \cdot \boldsymbol{\mu}_{ij}^m - (S^-)_{n,ij}^m] \left(\frac{A\Delta t}{V} \right)_{ij}^m, \quad (80) \\ D_{n,ij}^m & = - \left(\frac{S^-}{S^+ - S^-} \right)_{n,ij}^m [(c\mathbf{n}_n - \mathbf{u}_{ij}^m) \cdot \boldsymbol{\mu}_{ij}^m - (S^+)_{n,ij}^m] \left(\frac{A\Delta t}{V} \right)_{ij}^m. \end{aligned} \quad (81)$$

The radiation transport equation can be further written as

$$\begin{aligned} I_{n,i}^{m+1} & = - \left(\sum_{j=0}^{N_i-1} C_{n,ij}^m \right) I_{n,i}^{m+1} - \left(\sum_{j=0}^{\tilde{N}_i-1} D_{n,ij}^m I_{n,j}^{m+1} \right) - \left(\sum_{j=0}^{M_i-1} D_{n,ij}^m I_{n,j}^m \right) \\ & + (IV)_{n,i}^m / V_i^m + [(S_I)_{n,i}^{m+1} c \Delta t^m]_i. \end{aligned}$$

(82)

(92)

We rewrite this in the context of iterations. The last iteration is denoted by a superscript l , while the current iteration is denoted as $l+1$:

$$I_{n,i}^{m+1,l+1} = - \left(\sum_{j=0}^{N_i-1} (C^+)_{n,ij}^m \right) I_{n,i}^{m+1,l+1} - \left(\sum_{j=0}^{N_i-1} (C^-)_{n,ij}^m \right) I_{n,i}^{m+1,l} - \left(\sum_{j=0}^{\bar{N}_i-1} D_{n,ij}^m I_{n,j}^{m+1,l} \right) - \left(\sum_{j=0}^{M_i-1} D_{n,ij}^m I_{n,j}^m \right) + (IV)_{n,i}^m / V_i^m + \left[(SI)_{n,i}^{m+1,l+1} c \Delta t^m \right]_i. \quad (83)$$

Here we further split the coefficients C according to whether they are positive or negative, namely $(C^+)_{n,ij}^m = \max(C_{n,ij}^m, 0)$ and $(C^-)_{n,ij}^m = \min(C_{n,ij}^m, 0)$. All the negative terms are grouped into the last iteration. This is to ensure the coefficients in front of the specific intensities are always above unity during the iterations for a more robust performance (see appendix of J21). The equation then reads

$$\left[1 + (g^+)_{n,i}^m \right] I_{n,i}^{m+1,l+1} = (I_c)_{n,i}^{m+1,l} + \left[(SI)_{n,i}^{m+1,l+1} c \Delta t^m \right]_i, \quad (84)$$

where

$$(g^+)_{n,i}^m = \sum_{j=0}^{N_i-1} (C^+)_{n,ij}^m, \quad (85)$$

$$(g^-)_{n,i}^m = \sum_{j=0}^{N_i-1} (C^-)_{n,ij}^m, \quad (86)$$

$$(I_{c2})_{n,i}^{m+1,l} = -(g^-)_{n,i}^m I_{n,i}^{m+1,l} - \left(\sum_{j=0}^{\bar{N}_i-1} D_{n,ij}^m I_{n,j}^{m+1,l} \right) - \left(\sum_{j=0}^{M_i-1} D_{n,ij}^m I_{n,j}^m \right), \quad (87)$$

$$(I_c)_{n,i}^{m+1,l} = (I_{c2})_{n,i}^{m+1,l} + (IV)_{n,i}^m / V_i^m. \quad (88)$$

Since the source terms are measured in the comoving frame, we multiply Equation (84) by Γ^4 , which yields

$$\left[1 + (g^+)_{n,i}^m \right] (I')_{n,i}^{m+1,l+1} = (\Gamma_{n,i}^m)^4 (I_c)_{n,i}^{m+1,l} + (c \Delta t \rho \Gamma_n)_i^m \left[(\kappa_P)_i^m (B')_i^{m+1,l+1} - (\kappa_E)_i^m (J')_i^{m+1,l+1} + (\kappa_F + \kappa_s)_i^m (J' - I')_i^{m+1,l+1} \right]. \quad (89)$$

This gives

$$\left[1 + g_n^+ + c \Delta t \rho (\kappa_F + \kappa_s) \Gamma_n \right]_i^m (I')_{n,i}^{m+1,l+1} = (\Gamma_{n,i}^m)^4 (I_c)_{n,i}^{m+1,l} + (c \Delta t \rho \Gamma_n)_i^m \left[(\kappa_P)_i^m (B')_i^{m+1,l+1} + (\kappa_F + \kappa_s - \kappa_E)_i^m (J')_i^{m+1,l+1} \right]. \quad (90)$$

We define the coefficient

$$f_{n,i}^m \equiv \frac{1}{1 + [g_n^+ + c \Delta t \rho (\kappa_F + \kappa_s) \Gamma_n]_i^m}, \quad (91)$$

such that the equation becomes

$$(I')_{n,i}^{m+1,l+1} = (f \Gamma^4)_{n,i}^m (I_c)_{n,i}^{m+1,l} + (c \Delta t \rho \Gamma_n f_n)_i^m \left[(\kappa_P)_i^m (B')_i^{m+1,l+1} + (\kappa_F + \kappa_s - \kappa_E)_i^m (J')_i^{m+1,l+1} \right].$$

Summing it up over the solid angle yields

$$(J')_i^{m+1,l+1} = \left[\sum_{n=0}^{N_\Omega-1} (w'_n f_n \Gamma_n^4)^m (I_c)_n^{m+1,l} \right]_i + \left(c \Delta t \rho \kappa_P \sum_{n=0}^{N_\Omega-1} w'_n f_n \Gamma_n \right)_i (B')_i^{m+1,l+1} + \left[c \Delta t \rho (\kappa_F + \kappa_s - \kappa_E) \sum_{n=0}^{N_\Omega-1} w'_n f_n \Gamma_n \right]_i (J')_i^{m+1,l+1}. \quad (93)$$

We note that this summation was not written correctly in equation (25) of J21 because it did not take into account the angular dependence of g_n^+ . This was later corrected in Jiang (2022). We now define another coefficient

$$h_i^m \equiv \frac{1}{1 - [c \Delta t \rho (\kappa_F + \kappa_s - \kappa_E) \sum_{n=0}^{N_\Omega-1} w'_n f_n \Gamma_n]_i^m}. \quad (94)$$

The equation then becomes

$$(J')_i^{m+1,l+1} = h_i^m \left[\sum_{n=0}^{N_\Omega-1} (w'_n f_n \Gamma_n^4)^m (I_c)_n^{m+1,l} \right]_i + \left(h c \Delta t \rho \kappa_P \sum_{n=0}^{N_\Omega-1} w'_n f_n \Gamma_n \right)_i (B')_i^{m+1,l+1}. \quad (95)$$

Plugging it into the equation for the specific gas internal energy, we get

$$(e_g)_i^{m+1,l+1} = (e_g)_i^m + (4\pi \kappa_E \Delta t h)_i^m \left[\sum_{n=0}^{N_\Omega-1} (w'_n f_n \Gamma_n^4)^m (I_c)_n^{m+1,l} \right]_i - \left[4\pi \kappa_P \Delta t \left(1 - h c \Delta t \rho \kappa_E \sum_{n=0}^{N_\Omega-1} w'_n f_n \Gamma_n \right) \right]_i (B')_i^{m+1,l+1}. \quad (96)$$

Taking

$$b_i^{m+1,l} = (e_g)_i^m + (4\pi \kappa_E \Delta t h)_i^m \left[\sum_{n=0}^{N_\Omega-1} (w'_n f_n \Gamma_n^4)^m (I_c)_n^{m+1,l} \right]_i, \quad (97)$$

$$k_i^m = - \left[\rho \kappa_P c \Delta t \left(1 - h c \Delta t \rho \kappa_E \sum_{n=0}^{N_\Omega-1} w'_n f_n \Gamma_n \right) \right]_i, \quad (98)$$

$$(e_B)_i^{m+1,l+1} = \frac{a(T_i^{m+1,l+1})^4}{\rho_i^m}, \quad (99)$$

we thus arrive at a non-linear equation for $T_i^{m+1,l+1}$ as

$$y(T) = e_g(T) - k e_B(T) - b = 0, \quad (100)$$

where e_g and e_B are functions of $T_i^{m+1,l+1}$. The solution can be obtained via the Newton-Raphson method if the specific heat capacity c_V can be directly read from the EOS table to give dy/dT . This is a small improvement upon the implementation in ATHENA++, where an ideal gas is assumed for the EOS and a fourth-order polynomial is solved for each interaction (J21). With $T_i^{m+1,l+1}$ at hand, we can go back to Equation (95) to directly obtain $(J')_i^{m+1,l+1}$, and then to Equation (92) for $(I')_{n,i}^{m+1,l+1}$, and finally obtain $I_{n,i}^{m+1,l+1}$ via the Lorentz transformation $I = \Gamma^{-4} I'$.

3.4. Detailed Scheme for the Radiation Transport Module

In this subsection, we describe the steps the scheme takes to calculate the radiation field.

At the beginning of the simulation, we discretise the angular space in the lab frame based on Section 3.1, which gives

$$\mathbf{n}_n, w_n, \quad (101)$$

and set the initial radiation field.

At the end of each timestep, we start the radiation transport solver. First, we loop over all the active faces between cells, and calculate all the coefficients from the modified HLLC Riemann solver that do not change during the iterations, including (Equations (80) and (81))

$$C_{n,ij}^m, D_{n,ij}^m, \quad (102)$$

by which we get

$$(g^+)_{n,i}^m = \sum_{j=0}^{N_i-1} (C^+)_{n,ij}^m, \quad (g^-)_{n,i}^m = \sum_{j=0}^{N_i-1} (C^-)_{n,ij}^m. \quad (103)$$

For the summation, we need to perform the first flux communication between tasks in the radiation module to add the coefficients to the correct cells. We save these coefficients for later use

$$(g^+)_{n,i}^m, (g^-)_{n,i}^m, C_{n,ij}^m, D_{n,ij}^m. \quad (104)$$

Second, we loop over all the active cells, and calculate all the coefficients that do not change during the iterations, including

$$\Gamma_{n,i}^m = (1 - \mathbf{n}_n \cdot \boldsymbol{\beta}_i^m) / \sqrt{1 - (\boldsymbol{\beta}_i^m)^2}, \quad (105)$$

$$(w')_{n,i}^m = \frac{(\Gamma_{n,i}^m)^{-2} w_n}{\sum_{n=0}^{N_\Omega-1} (\Gamma_{n,i}^m)^{-2} w_n}, \quad (106)$$

$$f_{n,i}^m = \frac{1}{1 + [g_n^+ + c\Delta t\rho(\kappa_F + \kappa_S)\Gamma_n]_i^m}, \quad (107)$$

$$h_i^m = \frac{1}{1 - [c\Delta t\rho(\kappa_F + \kappa_S - \kappa_E)\sum_{n=0}^{N_\Omega-1} w'_n f_n \Gamma_n]_i^m}, \quad (108)$$

$$(f_{I\Sigma})_{n,i}^m = [hc\Delta t\rho(\kappa_F + \kappa_S - \kappa_E) f_n \Gamma_n^{-3}]_i^m, \quad (109)$$

$$(f_{IB})_{n,i}^m = (hc\Delta t\rho\kappa_P f_n \Gamma_n^{-3})_i^m, \quad (110)$$

$$(f_{\Sigma I})_{n,i}^m = (w'_n f_n \Gamma_n^4)_i^m, \quad (111)$$

$$(f_{b\Sigma})_i^m = 4\pi(h\Delta t\kappa_E)_i^m, \quad (112)$$

$$k_i^m = \left[c\Delta t\rho\kappa_P \left(hc\Delta t\rho\kappa_E \sum_{n=0}^{N_\Omega-1} w'_n f_n \Gamma_n - 1 \right) \right]_i^m. \quad (113)$$

We save these coefficients for later use

$$f_{n,i}^m, (f_{I\Sigma})_{n,i}^m, (f_{IB})_{n,i}^m, (f_{\Sigma I})_{n,i}^m, (f_{b\Sigma})_i^m, k_i^m. \quad (114)$$

Then, we enter the iteration. The initial values are set to the values at the m th timestep. During each iteration, proceed as follows: Exchange the primitive radiation variables $I_{n,j}^{m+1,l}$ between tasks. Loop over all the active cells to get

$$(I_c)_{n,i}^{m+1,l} = (IV)_{n,i}^m / V_i^m - (g^-)_{n,i}^m I_{n,i}^{m+1,l}. \quad (115)$$

Then, we loop over all the active faces to apply the fluxes from neighboring cells

$$(I_c)_{n,i}^{m+1,l} = (I_c)_{n,i}^{m+1,l} - \left(\sum_{j=0}^{\tilde{N}_i-1} D_{n,ij}^m I_{n,j}^{m+1,l} \right) - \left(\sum_{j=0}^{M_i-1} D_{n,ij}^m I_{n,j}^m \right). \quad (116)$$

This requires another flux communication between tasks. Afterwards, we loop over all the active cells to calculate

$$(I_\Sigma)_i^{m+1,l} = \sum_{n=0}^{N_\Omega-1} (f_{\Sigma I})_{n,i}^m (I_c)_{n,i}^{m+1,l}, \quad (117)$$

$$b_i^{m+1,l} = (e_g)_i^m + (f_{b\Sigma})_i^m (I_\Sigma)_i^{m+1,l}. \quad (118)$$

For each active cell, we use the Newton-Raphson method to solve the non-linear equation for T

$$y(T) = e_g(\rho_i^m, T) - k_i^m e_B(\rho_i^m, T) - b_i^{m+1,l} = 0, \quad (119)$$

which gives the solution $T = T_i^{m+1,l+1}$ and the integrated Planck function $(B')_i^{m+1,l+1} = ca(T_i^{m+1,l+1})^4 / (4\pi)$. Then calculate the specific intensities as

$$I_{n,i}^{m+1,l+1} = f_{n,i}^m (I_c)_{n,i}^{m+1,l} + (f_{IB})_{n,i}^m (B')_i^{m+1,l+1} + (f_{I\Sigma})_{n,i}^m (I_\Sigma)_i^{m+1,l}. \quad (120)$$

When the maximum iteration number $N_{\text{iter}}^{\text{max}}$ is reached ($N_{\text{iter}}^{\text{max}} = 10$ is the default for steady-state 3D simulations), or when the convergence criterion is reached, i.e. (J21)

$$\frac{\sum_{i=0}^{N_p-1} \sum_{n=0}^{N_\Omega-1} |I_{n,i}^{m+1,l+1} - I_{n,i}^{m+1,l}|}{\sum_{i=0}^{N_p-1} \sum_{n=0}^{N_\Omega-1} |I_{n,i}^{m+1,l+1}|} < \epsilon = 10^{-8} \text{ (default)}, \quad (121)$$

we stop the iteration and set $I_{n,i}^{m+1}$. See Section 6.3 for a detailed discussion of the criterion and alternative choices. This global value of the convergence criterion requires another communication between tasks.

Finally after we exit the iteration, we update the conserved quantities

$$(IV)_{n,k}^{m+1} = \begin{cases} I_{n,k}^{m+1} V_k^m, & \text{cell k is active,} \\ (IV)_{n,k}^m + \Delta(IV)_{n,k}^{m+1}, & \text{cell k is passive but} \\ & \text{has adjacent active cells,} \end{cases} \quad (122)$$

where $\Delta(IV)_{n,k}^{m+1}$ is the change in the conserved quantity for the passive cell due to the exchanged fluxes between the passive cell and neighboring active cells. This step requires another flux communication between tasks just to apply the fluxes to passive cells. This way, we guarantee that the conserved quantity IV and its integrated values, e.g., radiation energy and radiation flux, are indeed conserved. But the local time-stepping may still introduce artificial energy transport or momentum transport between cells while conserving the total conserved quantities.¹ In total, within each timestep, the radiation module performs N_{iter} primitive radiation variable exchanges between tasks, $N_{\text{iter}} + 2$ flux exchanges between tasks, and 1 convergence criterion exchange between tasks, where N_{iter} is the number of iterations. Within each variable or flux exchange between tasks, $\mathcal{O}(N_\Omega)$ variables are exchanged per active cell or per active face.

¹ In particular, in the free-streaming regime, local time-stepping may yield accumulating radiation near the active-passive cell boundaries. This is tested in Section 4.2.2, where we do not see such artifacts, but more complex simulations are needed to test the free-streaming regime with local time-stepping.

3.5. Coupling to the MHD Solver via the Radiation Source Terms

The major difference between post-processing with radiative transfer and full radiation hydrodynamics is that the radiation field needs to be coupled back to the MHD solver for the energy and momentum exchange between radiation and fluid. There are two ways to express the radiation source terms. One is to calculate the radiation source terms as they appear in the radiation transport equations. The other is to express them in terms of time derivatives and the transport terms, which conserves the total energy and total momentum.

By default, we use the conservative form of the radiation source terms. The change in (IV) due to the transport terms are

$$(\Delta_{\text{tr}} IV)_{n,i}^{m+1} = -(g^+)_{n,i}^m I_{n,i}^{m+1} V_i^m + (I_c)_{n,i}^{m+1} V_i^m - (IV)_{n,i}^m. \quad (123)$$

Therefore, we have

$$(IV)_{n,i}^{m+1} - (IV)_{n,i}^m - (\Delta_{\text{tr}} IV)_{n,i}^{m+1} = (g^+)_{n,i}^m I_{n,i}^{m+1} V_i^m - (I_c)_{n,i}^{m+1} V_i^m. \quad (124)$$

This yields the radiation source terms as

$$\begin{aligned} (S_{\text{r,E}} V)_i^{m+1} &= (E_{\text{r}} V)_i^{m+1} - (E_{\text{r}} V)_i^m - (\Delta_{\text{tr}} E_{\text{r}} V)_i^{m+1} \\ &= \frac{4\pi}{c} V_i^m \sum_{n=0}^{N_{\Omega}-1} \left[(g^+)_{n,i}^m I_{n,i}^{m+1} - (I_c)_{n,i}^{m+1} \right] w_n, \end{aligned} \quad (125)$$

$$\begin{aligned} (S_{\text{r,p}} V)_i^{m+1} &= \frac{1}{c^2} \left[(F_{\text{r}} V)_i^{m+1} - (F_{\text{r}} V)_i^m - (\Delta_{\text{tr}} F_{\text{r}} V)_i^{m+1} \right] \\ &= \frac{4\pi}{c^2} V_i^m \sum_{n=0}^{N_{\Omega}-1} \left[(g^+)_{n,i}^m I_{n,i}^{m+1} - (I_c)_{n,i}^{m+1} \right] \mathbf{n}_n w_n. \end{aligned} \quad (126)$$

At the end of each hydro timestep, we perform the radiation transport calculations, and only for the active cells do we subtract the source terms from the total gas energy and total gas momentum of the equations to get the conserved quantities. Then we update the primitive variables for the active cells in the MHD part, and the primitive variables for the radiation module including opacities and intensities.

3.6. Optional Features

For the boundary conditions, our current implementation supports periodic and inflow/outflow boundaries. To use the periodic boundary condition for the radiation module, the hydrodynamic boundary has to be set as periodic as well, which applies to most scenarios. The inflow/outflow boundary condition for the radiation module is independent of the hydrodynamic boundary. However, the radiation inflow boundary has to be set manually in the source code, as there is no universal way to inject radiation into the computational domain. For an example that uses a mixture of periodic and inflow/outflow boundaries, see test 4.1.4. For another example that injects radiation in the middle of the simulation box, see Section 5. We currently do not support reflective boundary condition, as radiation is rarely reflective and this is more difficult to realize with an angle-dependent discrete ordinates method.

We offer an optional feature to solve the *time-independent* radiation transport equation with the implicit discrete ordinates solver. This is done by neglecting the time derivative term, gas velocities, face velocities, and setting $\Delta t = 1$ in the factors and coefficients. Specifically, we solve for

$$c\mathbf{n} \cdot \nabla I = c\rho \left[(\kappa_{\text{p}} B - \kappa_{\text{E}} J) + (\kappa_{\text{F}} + \kappa_{\text{S}})(J - I) \right]. \quad (127)$$

By default, this is used to set the initial conditions for the radiation field, where we assume the radiation field starts to evolve from an initial equilibrium state. It can also be used to directly compare with the ray-tracing results, and to provide the Eddington tensor for a VET scheme. It can be further exploited for post-processing, in particular if multi-group radiation transport is feasible in the future. For this time-independent version, we also implement an option to couple the radiation source terms to the MHD solver as heating/cooling terms and radiation forces.

Moreover, we implement different options to test various numerical choices for specific problems. For example, the gas advection term can be solved explicitly as done in J21, which is expected to suppress numerical diffusion from gas advection but only works for global time-stepping. The coupling source terms can be solved in the non-conservative form, although caution is needed when using this with local time-stepping. The radiation transport step can be solved without coupling it to the gas temperature, although this typically creates large errors in our tests. Finally, it is possible to run the radiation solver only on globally synchronised timesteps despite using local timesteps for MHD. The timesteps taken in the radiation module are replaced by the globally synchronised timestep instead of the local timestep of the cell or the face. This will become a poor approximation when gas dynamics changes the radiation field on the timescales of MHD processes.

4. Test Problems

Test problems are essential for debugging new schemes and demonstrating the capabilities and limitations of numerical schemes. Here, we repeat most of the test problems in J21 for direct comparisons between AREPO and ATHENA++ results, with a few additional tests for broader contexts. Most of those tests can also be found in the method papers for the VET scheme (Davis et al. 2012; Jiang et al. 2012) and the semi-implicit discrete ordinates scheme (Jiang et al. 2014) for ATHENA++.

We perform all the tests on the moving Voronoi mesh except for test 4.3.3. For 2D tests, the mesh is initialized in a honeycomb-like configuration (Figure 1). This is done by constructing the cell centers in a Cartesian grid first, and then shifting every second row by half the cell size. In the evolving radiation tests and radiation hydrodynamic tests, we switch on local time-stepping. For the cases where the background medium is fixed or too homogeneous for automatic local time-stepping, we force different timesteps in different parts of the computational domain, as illustrated in Figure 1. For outflow boundary conditions, we set the incoming intensities to be zero and copy the outgoing intensities from the last active cells to the ghost cells, as in J21. The radiation constant a and the speed of light c are sometimes set to other values for exploring different regimes easily, which are specified in different tests. For all the tests, we do not distinguish between the flux-weighted opacity κ_{F} and the Rosseland opacity κ_{R} , and also do not distinguish between the energy-weighted opacity κ_{E} and the Planck opacity κ_{P} .

We normally adopt the angular discretization as described in Section 3.1 for 1D and 3D tests. However, for 2D tests, we use another set of angular bins for better coverage of the angular space. When we also need to keep the Eddington tensor to be $1/3$ for isotropic radiation in 2D, we set up the directions in two groups. One group is confined in the 2D plane ($n_z = 0$) and uniformly distributed on a unit circle where $n_x = \cos\theta$, $n_y = \sin\theta$. The other group shares the same set of θ as the first group, but has $n_x = \sqrt{1/3} \cos\theta$, $n_y = \sqrt{1/3} \sin\theta$, $n_z = \sqrt{2/3}$. When the Eddington tensor constraint is not needed for a purely optically-

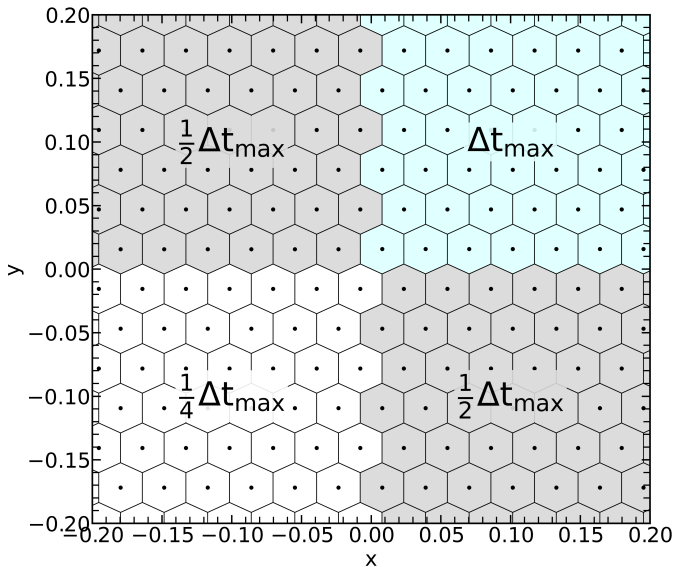


Fig. 1: Illustration of the forced local time-stepping on the initial honeycomb mesh in 2D tests. We use the hierarchical time-stepping in AREPO. The top right octant holds the normal timestep Δt_{\max} allowed by either maximum timestep limit or CFL condition for hydrodynamics. The diagonal octants are updated with timesteps $\Delta t_{\max}/2$, and the bottom left octant is updated with a timestep $\Delta t_{\max}/4$.

thin medium (e.g., Section 4.1.1), we only use the first group for the angular discretization.

We present the test results based on their categories:

1. We first test whether the code can capture the radiation field in a steady state with a fixed background (Section 4.1) by solving the *time-independent* radiation transport equation, where we set the transport terms to exactly balance the source terms. We use the time-independent flavour (Section 3.6) of our scheme for these tests. The tests explore different regimes, including 2D optically-thin medium, 1D optically-thick-to-thin medium with pure absorption, pure scattering, and a standard 2D shadow test.
2. Afterwards, we test the evolving radiation field with a fixed background (Section 4.2) by solving the time-dependent radiation transport equation. We demonstrate 2D dynamic diffusion for optically-thick regime and 2D expanding multi-source radiation bubble test for optically-thin-dominated regime.
3. Then we test the coupling between radiation and gas by performing radiation hydrodynamic tests (Section 4.3). We explore 2D thermal equilibrium, 2D linear waves, 1D radiation shocks, and 2D irradiated clouds.

Most of the tests can be directly compared with the figures in J21, since we almost always adopt the same setup. However, we use the honeycomb mesh for initial 2D mesh configuration, and switch on the moving mesh with local time-stepping for the second (evolving radiation) and third categories of tests (radiation hydrodynamics). In particular, except for tests in Section 4.2.1, 4.3.1 and 4.3.2, FLD and M1 will not produce accurate results for all the other tests due to the inaccurate representation for the direction of radiation. These are demonstrated in e.g. Sądowski et al. (2013), Murchikova et al. (2017), Thomas & Pfrommer (2022) and Menon et al. (2022) for some of the tests.

4.1. Steady-state Tests with Fixed Gas Background

4.1.1. 2D Crossing Beams in Optically-thin Vacuum

This test is designed to show how many iterations it takes for our scheme to converge in the optically thin medium. As already noted in J21, the iterative solver easily converges when the source terms dominate over the transport terms because the matrix of the coefficients is diagonally-dominant, which is typically the case in the optically-thick regime. However, in the optically-thin regime, we need many iterations for the information of the radiation field to propagate through the computational domain. Here, we show that if we have approximately N cells per dimension (so that the total cell number is $O(N^3)$ in 3D simulations), the safe choice would be to run $2N$ iterations to ensure a correct radiation field in the optically-thin regime.

To illustrate this extreme case, we set up a 2D box spanning $[-0.5, 0.5] \times [-2.0, 2.0]$ with two light beams injected from the bottom. We choose an angular resolution of 4 rays confined in the 2D plane, and two different spatial resolutions of 64×256 and 256×1024 . All the opacities are set to zero throughout the simulation for a vacuum background, and the intensities are also initialized to be zero. For the beams at the bottom boundary, we set the specific intensities at $x = -0.1, y = -2.0, n_x = -1/\sqrt{2}, n_y = 1/\sqrt{2}$ and $x = 0.1, y = -2.0, n_x = 1/\sqrt{2}, n_y = 1/\sqrt{2}$ to be $0.8c$. All the other intensities at the bottom boundary are set to be zero. We use a periodic boundary in the x direction and an outflow boundary at the top. The constants are set to be $a = 1, c = 10^3$, but the values do not matter for the test.

In Figure 2, we show the radiation energy density distribution for the crossing-beam tests. Two different spatial resolutions are shown in two rows, and three columns are for 20, 200, 2000 iterations. Panel (c) adopts the same resolution as J21, and thus can be directly compared with their figure 3. As illustrated in panel (f) compared with (c), increasing the resolution fourfold in both dimensions reduces the numerical diffusion, thereby suppressing the spreading of light beams. This was also demonstrated in figure 6 in Davis et al. (2012) for the short-characteristic scheme and figure 6 in Jiang et al. (2014) for the semi-implicit discrete ordinates scheme. Furthermore, we illustrate the propagation of radiation with increasing iterations from left to right. The sharp boundaries in the left column are likely a mesh effect from the background honeycomb mesh. Even after 200 iterations (middle column), the radiation field is still not converged since the information is not propagated to the top of the box. Our tests suggest that in the optically-thin regime, radiation only propagates through approximately one layer of cells in one to two iterations. Therefore, for the optically-thin radiation to be correctly captured, simulations with higher spatial resolution would also require more rounds of iterations.

This test shows that our scheme can correctly capture the direction of radiation in the optically-thin regime. If other moment-based method were applied to this problem, the FLD method will fill the domain with a more uniform radiation field, whilst the M1 method will merge the two crossing beams into one (e.g. figure 3 in Asahina et al. 2020). We also illustrate that increasing spatial resolution suppresses the numerical diffusion of our scheme, albeit at the cost of more rounds of iterations in the optically-thin regime.

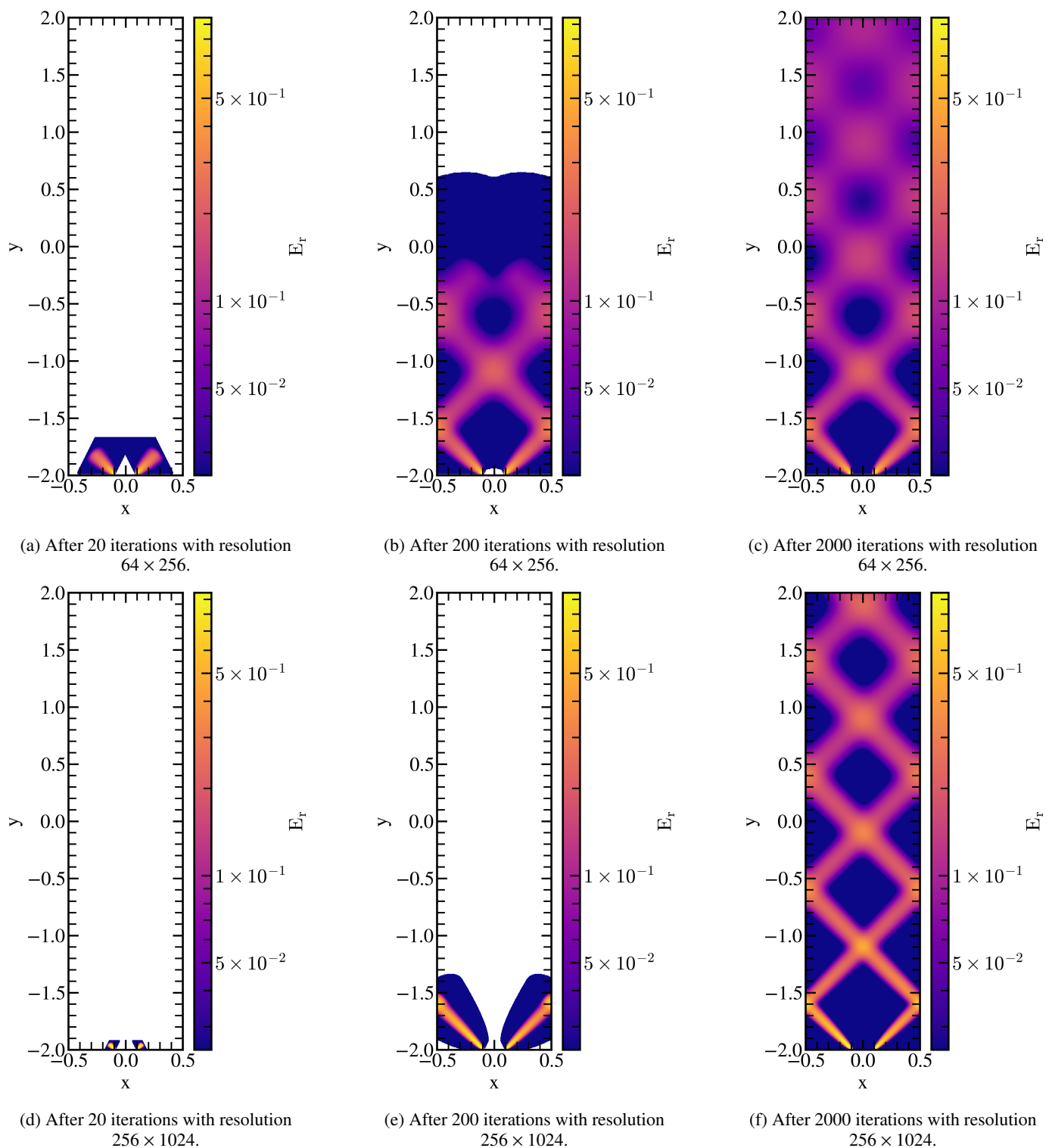


Fig. 2: 2D crossing-beam tests with different spatial resolutions (rows) and different numbers of iterations (columns). The color shows the radiation energy density distribution when two light beams are injected from the bottom of the simulation box. White indicates that the radiation energy density is zero as the initial condition. From left to right, different columns show increasing iterations. Information of the radiation field approximately propagates through one layer of cells per one or two iterations, so the iteration needed also depends on resolution, as demonstrated in Figure (b) compared to (e). The light beams spread due to numerical diffusion when propagating through the box. Figure (a-c) uses the same resolution as figure 3 in J21 for direct comparison. Figure (d-f) increases the resolution fourfold in both dimensions, thereby reducing the numerical diffusion.

4.1.2. 1D Absorption-dominated Homogeneous Sphere in Spherical Coordinates

With this test, we demonstrate the transition from the optically-thick to the optically-thin region with pure black body emission

and absorption. It also serves as a showcase for our scheme in 1D spherical coordinates for future tests on radiation hydrodynamic simulations of 1D stars, winds, accretion or shock waves, etc.

To construct the initial condition for this test, we adopt exactly the same setup as in J21. We use 1000 mesh points covering $r \in [0.05, 7]$ in 1D spherical coordinates and 40 directions for the radiation module. We setup a homogeneous sphere of radius $R_0 = 1$, density $\rho_0 = 1$, temperature $T_0 = 1$, and absorption opacity $\kappa_R = \kappa_P = 10$ with zero scattering opacity. Outside of the sphere, we set zero opacities such that the background is effectively vacuum to radiation. We initialize the intensities to be the isotropic value $caT_0^4/(4\pi)$. We fix the intensities as their isotropic value at the left boundary, and use an outflow boundary on the right. The constants are set to be $a = 1, c = 100$, but the values do not matter for the test.

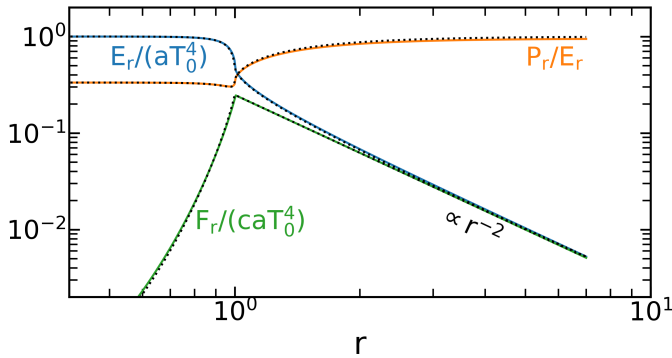


Fig. 3: 1D absorption-dominated homogeneous sphere test. Different solid colored lines show the profiles of normalized radiation energy density $E_r/(aT_0^4)$, normalized radiation flux $F_r/(caT_0^4)$, and the radial component of the Eddington tensor P_r/E_r as functions of the radius r . All of the simulated results align with the analytical solutions indicated by black dotted lines. Divided by $r = 1$, the radiation field transits from radiative diffusion in LTE inside the optically-thick sphere to free-streaming in the optically-thin vacuum.

For our scheme to work in 1D spherical coordinates, we use a specific set of angular discretization and take care of the additional transport terms arising from the curvature of the coordinate system, as described in Section 3.2.4 in J21. Since we directly take this part of the code from the public version of ATHENA++², we do not describe the method again, but refer the interested readers to J21 and the ATHENA++ code.

There is an analytical solution to this problem (Smit et al. 1997). The specific intensities depend on the radial coordinate r and the directional unit vector \mathbf{n} as

$$I(r, \mathbf{n}) = \frac{caT_0^4}{4\pi} \{1 - \exp[\rho_0 \kappa_R s(r, n_r)]\}, \quad (128)$$

where n_r is the radial component of \mathbf{n} and

$$s(r, n_r) = \begin{cases} rn_r + R_0 g(r, n_r), & r < R_0, \\ 2R_0 g(r, n_r), & r \geq R_0 \text{ \& \ } \sqrt{1 - (R_0/r)^2} \leq n_r \leq 1, \\ 0, & \text{otherwise,} \end{cases} \quad (129)$$

$$g(r, n_r) = \sqrt{1 - (r/R_0)^2 (1 - n_r^2)}. \quad (130)$$

² <https://github.com/PrincetonUniversity/athena>

In Figure 3, we show the profiles describing the radiation field inside and outside of the homogeneous sphere, which fits well with the analytical solutions (black dotted lines). Inside the optically-thick sphere, the radiation follows radiative diffusion in LTE, where the radiation temperature is the same as the gas temperature, with the radiation pressure being 1/3 of the radiation energy density and a radiation flux proportional to the radiation energy density gradient. Outside of the photosphere at $r > R_0$, the radiation field transits to free-streaming, where the profiles asymptotically approach $P_r = E_r$ and $F_r = cE_r \propto r^{-2}$, which indicates a constant luminosity. The radiation field takes 1000 iterations to pass through the 1000 mesh points, which supports the conclusion we reached in Section 4.1.1 that radiation only propagates through one cell in one iteration.

This test illustrates that our scheme correctly simulates the radiation field in the transition zone between optically-thick and optically-thin regions, which is crucial for simulations of stellar atmospheres, transients, and disk photospheres. For this test, the M1 closure method always overestimates the Eddington tensor near the photosphere (Smit et al. 1997; O’Connor 2015; Murchikova et al. 2017; Anninos & Fragile 2020), indicating cautions when simulating immediate surroundings of stellar photospheres or transients using M1 radiation transport.

4.1.3. 1D Scattering-dominated Non-LTE Atmosphere

This test aims to show the transition from optically-thick to optically-thin region when the medium is dominated by scattering. When the source term is dominated by scattering, the intensity is also influenced by radiation coming from other directions, such that standard ray-tracing breaks down and many rounds of iterations are needed to capture the radiation field properly.

We use exactly the same setup as in J21 by adopting 1280 mesh points covering $x \in [-10, 10]$ in 1D and 8 directions for the radiation module. We fix the density profile to be $\rho = 10^{-3} \exp(10 - x)$ and a uniform temperature field $T = T_0 = 1$. The opacities are also set uniformly in the computational domain, with absorption opacity $\kappa_R = \kappa_P = \epsilon$ and scattering opacity $\kappa_S = 1 - \epsilon$, where ϵ is a small value for the scattering-dominated atmosphere. We initialize the intensities to be the isotropic value $caT_0^4/(4\pi)$. We fix the intensities as their isotropic value at the inner boundary of the atmosphere, and use an outflow boundary for the outer boundary of the atmosphere. The constants are set to be $a = 1, c = 1$, but the values do not matter for the test.

The analytical solution to this problem is (J21)

$$E_r = aT_0^4 \left[1 - \frac{\exp(-\sqrt{3}\epsilon\tau)}{1 + \sqrt{\epsilon}} \right], \quad (131)$$

where the optical depth from the right boundary is $\tau = \int_x^{10} \rho(\kappa_R + \kappa_S) dx = \int_x^{10} \rho dx = 10^{-3} [\exp(10-x) - 1]$. In Figure 4, we show the radiation energy density as a function of the optical depth. The solid lines show the simulation results, with different opacities indicated in different colors. They agree well with the analytical solutions shown in black dotted lines. The radiation transits from LTE in the optically-thick region (right) to the non-LTE optically-thin atmosphere (left) where the radiation has a much smaller temperature than the gas. As noted in Davis et al. (2012), Jiang et al. (2014) and J21, greater deviation from LTE requires significantly more rounds of iterations. For example, our scheme needs about 10^3 iterations for the $\epsilon = 10^{-1}$ case to converge to the analytical solution, while the $\epsilon = 10^{-8}$ case needs about 10^6 iterations. This is similar to the finding in J21, where they

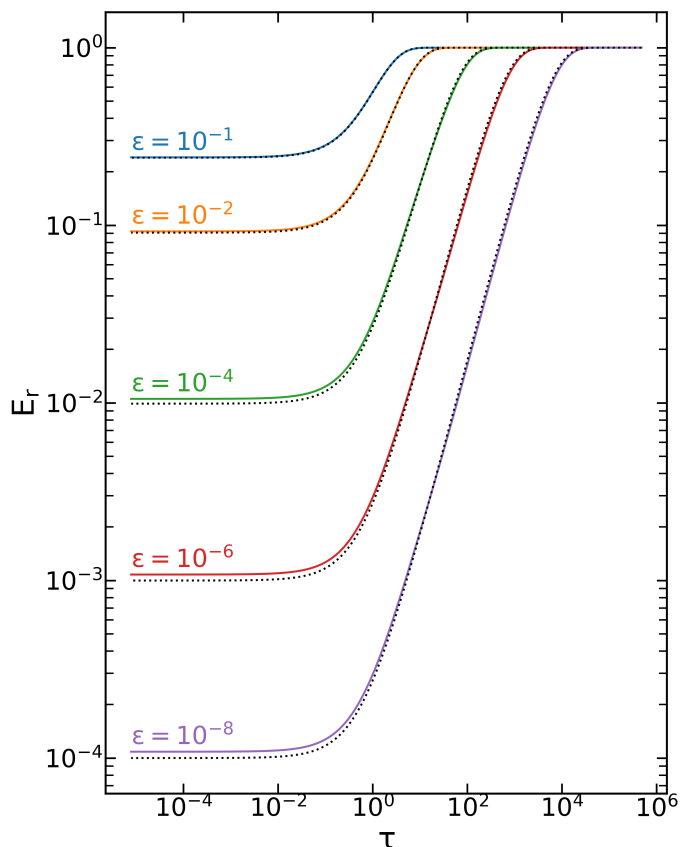


Fig. 4: 1D scattering-dominated non-LTE atmosphere tests for different absorption opacity ϵ and scattering opacity $1 - \epsilon$. The solid lines show the radiation energy density E_r as functions of the optical depth τ , transiting from LTE in the optically-thick region (right) to the non-LTE optically-thin atmosphere (left). The dotted black lines show the analytical solutions. As the atmosphere becomes more scattering-dominated (top to bottom indicated by different colors), the radiation temperature deviates from the gas temperature more in a more extended region. This test also demonstrates that significant scattering can reduce the radiation coming from an optically-thick region.

showed that the discrete ordinates scheme is slower at convergence for this particular test compared to short characteristics.

With this test, we show that our scheme produces the correct radiation field in scattering-dominated medium regardless of the optical thickness, but is rather expensive in the optically-thin regime. Such scenario is important for systems involving dust scattering, e.g. wind driving in cool stars (Habing 1996) and observational signatures of protoplanetary disks (Zhu et al. 2019).

4.1.4. 2D Shadow Test

The shadow test is a classic test to demonstrate the difference between different radiation transport methods, in particular FLD, M1, and other more accurate methods. FLD and M1 do not give the correct answer to this problem (e.g., figure 13 in Menon et al. 2022). For FLD, the radiation is directed along the radiation energy density gradient, thereby filling the shadow. M1 treats the radiation like fluid, so the two radiation beams collide and merge into one, and non-stationary radiation vortices are sometimes observed behind the optically-thick object.

We setup the simulation box similar to J21. The box covers $[-0.5, 0.5] \times [-0.3, 0.3]$ with two parallel rays cast from the left. We use a spatial resolution of 512×256 and 24 angles consisting of two groups of angular sets to ensure correct Eddington tensors in both optically-thick and optically-thin regime. We describe the elliptical optically-thick cloud and the near-vacuum background with a density distribution of $\rho(x, y) = 1 + 9 / \{1 + \exp[10((x/0.1)^2 + (y/0.06)^2 - 1)]\}$, a temperature distribution $T(x, y)$ that creates uniform pressure $P = \rho T = 1$, and a pure absorption opacity $\kappa_R = \kappa_P = \rho T^{-3.5}$. The density and temperature background is therefore $\rho_0 = 1, T_0 = 1$. This ensures that the total optical depth is approximately one across the background but reaches more than 10^5 across the cloud (J21). We initialize the intensities to be the isotropic value $caT^4/(4\pi)$. From the left boundary, we inject two parallel rays of radiation by setting intensities along the directions $\pm 15^\circ$ confined in the 2D plane to be $1031.3ca$ for each ghost cell, set other intensities to be zero, and use an outflow boundary condition for the right boundary. We adopt periodic boundary conditions in the vertical direction. The constants are set to be $a = 10^{-7}, c = 1.9 \times 10^5$, but the values do not matter for the test. We set the maximum iteration number to be 2000.

In Figure 5, we show the relaxed radiation field when an optically-thick cloud is immersed in two parallel rays of light at $\pm 15^\circ$. The top, middle, and bottom panels illustrate the normalized radiation energy density, the xx component, and the yy component of the Eddington tensor, respectively. In the optically-thin background, the radiation energy follows the injected value, and the direction follows the injected rays nearly-parallel to the x axis. In the optically-thick cloud, the radiation temperature is in equilibrium with the gas temperature of the cloud, and the radiation field is nearly isotropic with an Eddington tensor of 1/3 on the diagonal. Immediately behind the cloud, a triangular shadow is formed. Two extended wings at $\pm 15^\circ$ can also be found behind the cloud with half of the injected radiation energy density, because the injected rays coming from the same direction are blocked by the cloud. In the middle of the two wings, the injected rays are not blocked by the cloud, and therefore the radiation energy density holds the injected value as the unblocked background. We illustrate in this test that the shadow behind optically-thick objects is correctly captured in our scheme, and the results are almost identical to J21.

4.2. Evolving-radiation Tests with Fixed Gas Background

4.2.1. 2D Dynamic Diffusion

This test is an essential test to demonstrate if the scheme can capture radiative diffusion in the optically-thick regime even in a moving medium. If the fluxes are not carefully calculated for scattering-dominated regime, the numerical diffusion can easily dominate over the physical diffusion, resulting in a much shorter diffusion time-scale (Jiang et al. 2013, 2014; Jiang 2021). This is especially true for the discrete ordinates method, since the equations are not by design the diffusion equations as solved in FLD. The test also shows that exploiting local time-stepping does not change the diffusion time-scale or introduce any discontinuous artifacts in the radiation field.

We use the same setup in J21 but extend the box in 2D, because we aim to perform the test on a moving Voronoi mesh, which can only be constructed in 2D and 3D. We adopt a slim box with a spatial resolution of 1280×16 covering $[-10, 10] \times [-0.125, 0.125]$. We use the default angular discretization not specific to 2D with 8 directions to reduce the computational cost,

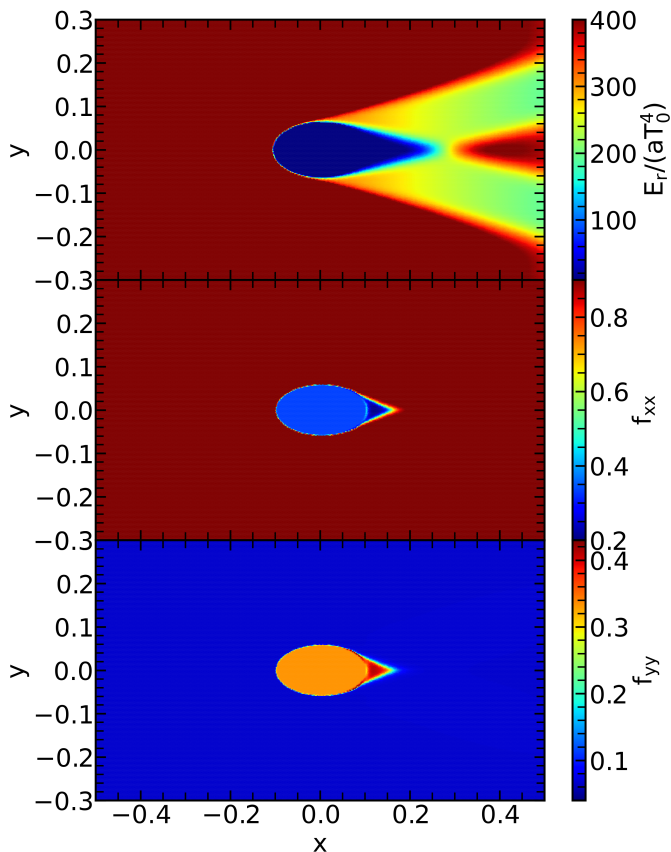


Fig. 5: 2D shadow test. We inject two parallel rays of light at $\pm 15^\circ$ from the left, which cast a shadow behind the central optically-thick cloud. The top, middle, and bottom panels show the normalized radiation energy density $E_r/(aT_0^4)$, component of the Eddington tensor along xx direction f_{xx} , and component of the Eddington tensor along yy direction f_{yy} , respectively. Inside the optically-thick cloud, the radiation field is nearly isotropic such that the diagonal components of the Eddington tensor are $1/3$. The radiation field becomes more anisotropic in the shadow. Outside the shadow in the background, the radiation follows the trajectories of injected rays with a small amount of numerical diffusion.

since the radiation field is almost isotropic. The uniform background is fixed with a constant density $\rho = 1$, a constant temperature $T = 1$, a constant horizontal velocity $v^x = 1$, a constant scattering opacity $\kappa_s = 4 \times 10^4$ and zero absorption opacities. The intensities are initialized to be the isotropic values associated with a radiation energy density of Gaussian-peak shape $E_r(x, y) = \exp(-40x^2)$, $x \in (-0.5, 0.5)$ with a floor of $E_r(x, y) = \exp(-10)$, $|x| \geq 0.5$. We use periodic boundary conditions for all boundaries. The constants are set to be $a = 1$, $c = 1000$ such that the diffusion time-scale of the peak $t_{\text{diff}} \sim \rho\kappa_s/c = 40$ is comparable to the gas advection time-scale $t_{\text{adv}} \sim L^x/v^x = 20$ where $L^x = 20$ is the horizontal size of the box. We find that the numerical parameter in the signal speed (Equation (79)) needs to be increased to $\alpha = 20$ to obtain accurate results in 2D. We manually apply a three-level hierarchy of local time-stepping as illustrated in Figure 1.

The dynamic diffusion of the radiation peak is shown in Figure 6 for time $t = 0, 4, 8, 16$ in different colors. We sort the 2D data points according to their x coordinates, and plot the radiation energy density E_r as a function of x . Initially, the radia-

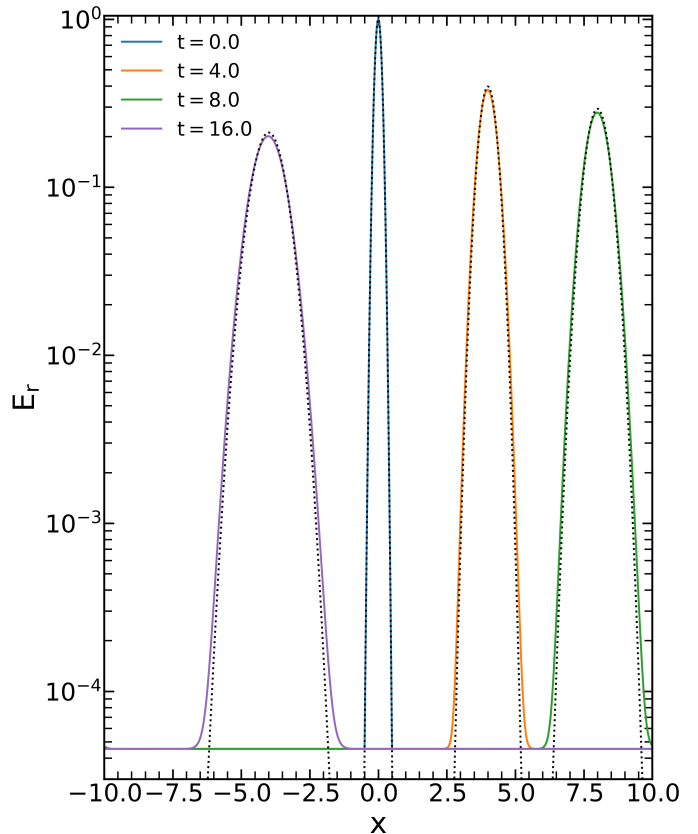


Fig. 6: 2D dynamic diffusion test. The plot shows the radiation energy density E_r as a function of the x coordinate at different times. We initialize the radiation field as an energy density Gaussian peak at the center (blue). As the radiation field evolves, the peak is dragged along with the moving fluid, and in the mean time spreads due to radiative diffusion. The shapes of the peaks agree well with the analytical solutions (black dotted lines), which suggests that the dynamic diffusion is well-captured by our scheme even on an unstructured moving mesh with forced local time-stepping.

tion is concentrated at the box center as a narrow Gaussian peak (blue). As the radiation field evolves in the uniformly moving background gas, the radiation peak is advected with the gas at the gas speed $v^x = 1$. Meanwhile, the peak spreads due to radiative diffusion in the optically-thick medium. The profiles of the radiation peaks at different times coincide with the analytical solutions (black dotted lines). For local time-stepping, we do not observe artifacts at the boundaries between regions that hold different timesteps, and the diffused shape of the peak is not changed by forced local time-stepping. Therefore, we have demonstrated that dynamic diffusion can be correctly captured in our scheme, even on an unstructured moving mesh with forced local time-stepping.

4.2.2. 2D Expanding Multi-source Radiation Bubbles

With this test, we aim to show the propagation of radiation in the optically-thin region emitted by multiple optically-thick radiation sources, especially when the radiation only propagates through a small portion of the simulation box in one timestep. Such setup provides an idealized showcase motivated by the test in Thomas & Frommer (2022), with implications for the ioniz-

ing radiation in star-forming regions or in the epoch of reionization. This test also demonstrates how the numerical diffusion spreads the radiation in optically-thin region, and how local time-stepping does not jeopardize the results.

We construct the initial condition in a 2D box of $[-0.5, 0.5] \times [-0.5, 0.5]$ with a spatial resolution of 1024×1024 and 200 directions consisting of two groups of angular sets. For radiation sources, we setup 20 optically-thick homogeneous spheres with varying radii and temperatures. Their locations, radii, and temperatures seem to be randomly distributed, but are actually determined by deterministic functions (available at Zenodo: doi: [10.5281/zenodo.15032138](https://doi.org/10.5281/zenodo.15032138)). This is for the test to be reproducible with other methods, an improvement we made upon the test in [Thomas & Pfrommer \(2022\)](#). The whole domain is in pressure balance with a uniform pressure $P = 1$, and the density is determined from $\rho = P/T$, where the temperature $T(x, y)$ is different in each sphere and in the background. The background is fixed to have a temperature of 10^{-3} and zero opacity, such that it is effectively vacuum to radiation. Inside each homogeneous sphere, we set the absorption opacity to satisfy $\kappa_R = \kappa_P = 10^5/\rho$ with zero scattering opacity, such that the optical depth across each sphere is at least 10^3 . We initialize the intensities to be the isotropic value $caT^4/(4\pi)$. All boundaries are set to be outflow for radiation, and we only evolve the radiation field. We choose the constants to be $a = 1, c = 10$, such that the light-crossing time for the box is $t_c = 0.1$ and the CFL timestep is approximately $\Delta t_{\text{CFL}} = 4 \times 10^{-5}$ for a CFL number of 0.4 when the signal speed is the speed of light. We set the maximum iteration number to be 200 per timestep.

It is important to demonstrate the power of the implicit scheme to overcome the small timesteps when propagating radiation even if local time-stepping is used. Therefore, we choose a maximum timestep of 0.001, about 25 times larger than the CFL timestep limited by the speed of light. This results in a three-level timestep hierarchy of 0.00078, 0.00039, 0.000195 distributed in the 2D plane as illustrated in Figure 1. In Figure 7, we show the expansion and merging process of radiation bubbles. The 20 radiation sources with varying sizes and luminosities are shown in panel a. The radiation bubbles expand at the speed of light (panel b), merge (panel c), and eventually fill the simulation box (panel d). The radiation field is dominated by radiation from the luminous sources clustered at the top and lower-right of the box, which is designed to mimic the clustering of massive stars. We find no artifact at the boundaries between regions holding different timesteps. We also compare the figures with another test that adopts global time-stepping, and find almost identical results. We therefore conclude that local time-stepping does not change the simulation results when the radiation is free-streaming in the optically-thin region, but more complex simulations are needed to confirm this.

In panel b, for each individual expanding bubble, we predict its size as $R_0 + ct$ and plot them as blue circles, where R_0 is the size of the individual source and t is the time of the simulation. The radiation energy density falls off as r^{-2} and follows analytical prediction shown in Section 4.1.2. We therefore only plot the predicted bubble sizes for those that are luminous enough to have a radiation energy density at the radiation front larger than the colorbar floor. The bubble sizes in the simulation generally agree with the predicted ones, indicating that the bubbles indeed expand at the speed of light, even though we take much larger timesteps than the CFL condition. However, the radiation fronts are not sharp but more extended due to the numerical diffusion. This seems to suggest that, if our method is applied to more complicated reionization simulations, the surroundings may be ion-

ized sooner than what nature does. But this may not be an issue, because the radiation energy density in the diffused part falls off quickly with radius, and is generally orders of magnitude smaller than the radiation energy density at the radiation front.

This test also demonstrates the accuracy of our method in simulating a complicated radiation field propagating at the speed of light. For example, in panel c and d, we show that the intense radiation leaves shadows behind the dim optically-thick sources, and the shadows are pointed towards different directions depending on their relative positions to the luminous clusters. [Thomas & Pfrommer \(2022\)](#) also illustrated that, due to the fluid-like description of M1 closure, it predicts the collision of radiation bubbles, which generates rarefaction waves and shock fronts that artificially enhance or decrease the radiation energy locally. But with our method, the radiation bubbles pass each other as light is supposed to behave (see also the discrete ordinates results in [Thomas & Pfrommer 2022](#)).

4.3. Radiation Hydrodynamic Tests for Radiation-gas Coupling

4.3.1. 2D Thermal Equilibrium in a Uniform Medium

This test is a simple demonstration of the coupling between radiation and gas. Specifically, we test the exchange of energy and momentum between radiation and gas.

We setup the problem the same way as in [J21](#) with a 2D box covering $[0, 1] \times [0, 1]$. We set the spatial resolution to be 32×32 , with 24 directions for the angular resolution consisting of two groups of angular sets. The box is filled with uniform medium of density $\rho = 1$, temperature T_0 , horizontal velocity v_0^x , absorption opacity $\kappa_R = \kappa_P = \kappa_a$ and zero scattering opacity. The intensities are initialized to be the isotropic value set by the radiation energy density $E_{r,0}$, which is out of thermal equilibrium. All boundaries are set to be periodic for both fluid and radiation. We choose $a = 1$ with three sets of different parameters: (1) $T_0 = 1, E_{r,0} = 100, v_0^x = 0, \kappa_a = 100, c = 100$; (2) $T_0 = 100, E_{r,0} = 1, v_0^x = 0, \kappa_a = 1, c = 100$; (3) $T_0 = 1, E_{r,0} = 1, v_0^x = 3, \kappa_a = 1, c = 10$.³ The thermal relaxation time-scale can be calculated for different parameter sets as $t_0 = 1/(c\rho\kappa_a)$. We manually apply a three-level hierarchy of local time-stepping as illustrated in Figure 1.

In Figure 8, we show the results of three tests. The first two panels illustrate the swift relaxation to thermal equilibrium in static media, either for optically-thick (left panel) or for optically-thin regime (middle panel). The averaged radiation energy density E_r (red) and averaged aT_{gas}^4 (black) reach the same value as the analytical solution (grey dotted). This proves that the total energy is conserved and the energy is exchanged between gas and radiation. The time evolution to the equilibrium value is not correctly displayed in the left panel, because the hydro timestep is about $10 t_0$, and the system reaches thermal equilibrium in one timestep, although physically it should take much less time. In the middle panel, the system reaches the approximate equilibrium state much faster than t_0 , because the initial deviation from equilibrium is orders of magnitude larger than the equilibrium value, which accelerates the initial thermal relaxation process. However, if we plot the temperature in linear scale, it is evident that the system is still approaching the exact equilibrium state at the end of the simulation, because the ultimate

³ In [J21](#), they recorded that the last test is performed with $c = 100$. We have checked that in our case, this parameter will not produce the equilibrium E_r and v^x as reported in [J21](#). This is likely a typo, because if we choose $c = 10$ the results agree very well.

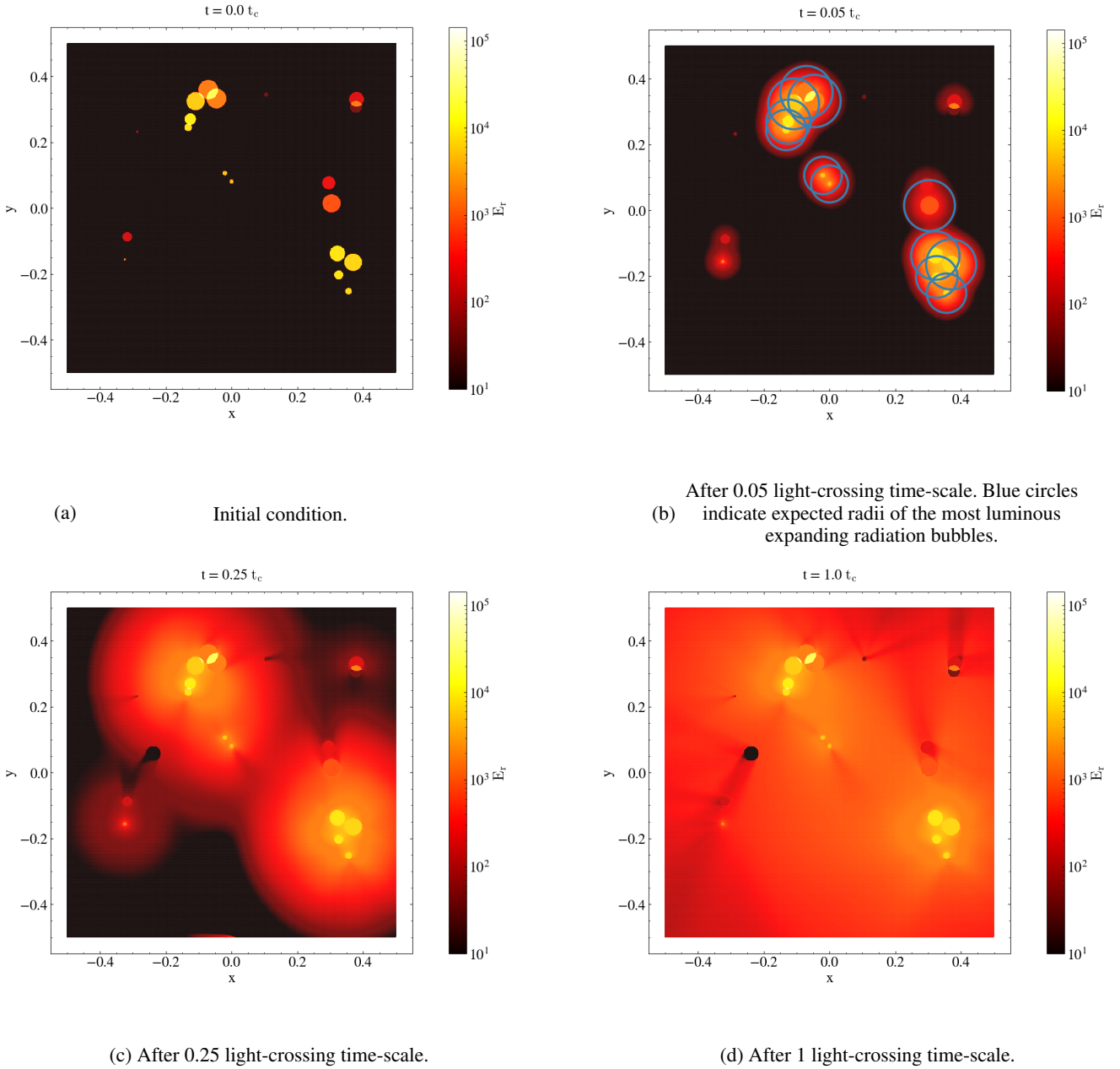


Fig. 7: 2D expanding multi-source radiation bubble test, with a maximum timestep 25 times larger than the CFL condition among the three levels of local timestep hierarchy. The colors show the radiation energy density distribution. We follow the propagation of 20 radiation bubbles in vacuum until the light crosses the whole box. The bubbles are emitted from 20 optically-thick sources with different luminosities seemingly randomly distributed (panel a). The radiation does propagate at the speed of light, but the radiation fronts are slightly spread by numerical diffusion compared to the expected fronts (blue circles in panel b). The radiation bubbles run into each other and merge (panel c). Eventually, they fill the simulation box, leaving small shadows behind the dim optically-thick sources (panel d). As shown in the expansion of the bubbles, most of the radiation comes from the luminous sources clustered at the top and bottom right.

thermal relaxation timescale is t_0 . In the right panel, we examine the thermal equilibrium in a uniformly moving medium and show the relative errors of different quantities compared to their expected values. The relaxed radiation energy density E_r (blue) and the horizontal velocity v^x (orange) fit well with the values reported in J21 to the reported precision. The average total energy density (green) and the average total horizontal momentum density (red) also do not change within the relative errors of 10^{-7} . Even though this test does not guarantee the conservation of en-

ergy and momentum in sophisticated simulations, it shows that the energy and momentum are conserved in the simple test even on an unstructured moving mesh with forced local timesteps.

4.3.2. 2D Linear Waves

The linear wave test is a basic test to show the accuracy of the code and the convergence order of the scheme. It can also expose the errors introduced by the moving-mesh noises that affect the

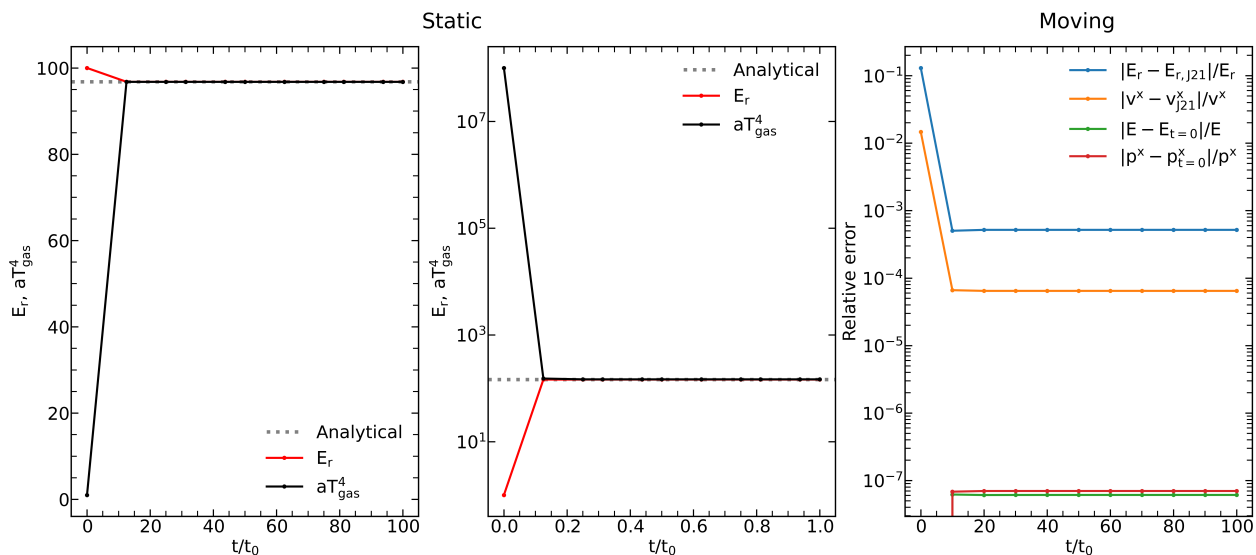


Fig. 8: 2D thermal equilibrium test. We start with a radiation field and a temperature field very far from equilibrium with each other, and they quickly reach thermal equilibrium state as the system evolves. All the x axes indicate the time t of the simulation in unit of the thermalization time-scale t_0 . In the first two panels, we explore thermal equilibrium in static media, and show that E_r (red) and aT_{gas}^4 (black) become equal at a value consistent with the analytical solutions (grey dotted). In the last panel, we show the relative error of different values: the radiation energy density compared to the **J21** reported value (blue), the horizontal velocity compared to the values reported in **J21** (orange), the average total energy density compared to its initial value (green), and the average total horizontal momentum density compared to its initial value (red). The relative errors show that our results are consistent with the values reported in **J21** to the precision they reported, and that the total energy and total momentum are conserved at 10^{-7} level even with local timesteps on an unstructured moving mesh.

convergence, especially in radiation-dominated optically-thick waves.

We perform the tests similar to **J21** by setting up 2D boxes spanning $[0, 1] \times [0, 1]$. We vary the spatial resolution from 16×16 to 256×256 , and fix the angular resolution as 8 directions using the default angular discretization not specific to 2D setup. We set the uniform background with density $\rho_0 = 1$, temperature $T_0 = 1$, gas pressure P_0 , and absorption opacity $\kappa_R = \kappa_P = \kappa_a$. The equation of state is chosen to be $P = \rho T$ with an adiabatic index $5/3$. On top of the uniform background, we add perturbations with an amplitude of 10^{-3} via eigenmodes with a wavelength the size of the box, calculated from the dispersion relation detailed in Appendix B of **Jiang et al. (2012)**. We initialize the intensities to be the equilibrium values calculated from the time-independent version of our scheme, as we find that this procedure reduces the errors for radiation-dominated optically-thick waves. All boundaries are set to be periodic. Two physical parameters to this problem are the optical depth per wavelength $\tau_a = \rho_0 \kappa_a$, and the ratio between radiation energy density and gas pressure aT_0^4/P_0 . We thus fix the speed of light as $c = 10$, and vary a and κ_a . We manually apply a three-level hierarchy of local time-stepping as illustrated in Figure 1.

We evolve the system for one period, and compare the results with the analytical solutions. In Figure 9, we measure the L1 norm of the absolute error in density, and plot it against the number of cells in the horizontal dimension. For gas-dominated waves (left panel), the convergence curve follows N^{-2} , as expected for second-order accurate hydro solver in **AREPO**. However, we find the same trend for radiation-dominated waves (right panel), even though the errors should be dominated by the first-order accurate radiation solver, as shown in **Jiang et al. (2012, 2014)** and **J21**. Such excellent performance is unexpected, and deserves further investigation. We find that the convergence gen-

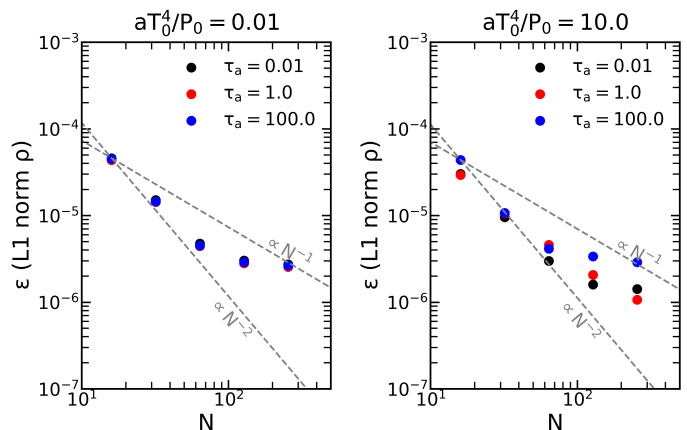


Fig. 9: 2D linear wave test showing the convergence with increasing spatial resolution. We explore different physical parameters of $\tau_a = 0.01, 1, 100$ in different colors and $aT_0^4/P_0 = 0.01, 10$ in different panels. The L1 norm of the absolute error in density generally decreases with increasing number of cells in the horizontal dimension. The curves fall off as N^{-2} , until they saturate at 10^{-6} level, where the errors are dominated by moving-mesh noises as discussed in the main text.

erally saturates at 10^{-6} , even for pure hydro tests not shown here. This is because the moving-mesh noises introduce errors at 10^{-6} level, which is also why we set the perturbations with amplitudes 10^{-3} instead of 10^{-6} as in **Jiang et al. (2012, 2014)** and **J21**. However, the moving-mesh noises do not show up in 1D tests, such as those demonstrated in **Springel (2010)** and **Weinberger et al. (2020)**. In multi-dimensional tests, the moving-mesh noises may be suppressed by using higher-order

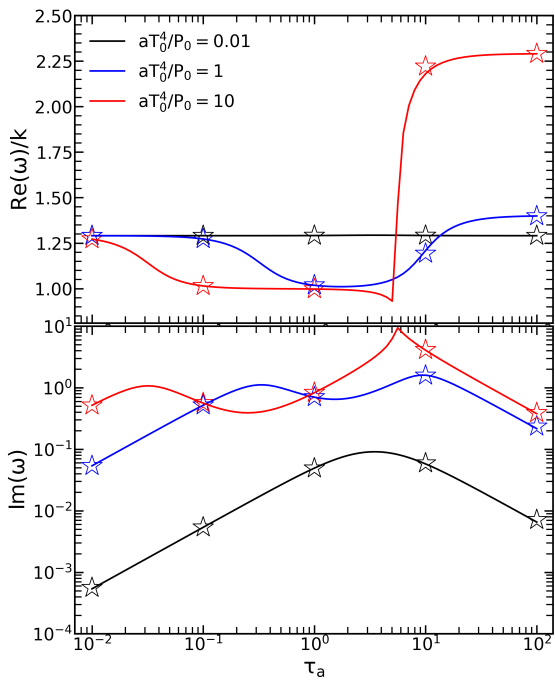


Fig. 10: 2D Linear wave test showing the phase speed (top) and the damping rate (bottom) of waves. We use the simulation results with resolution 256×256 (stars), which agree well with the analytical solutions (solid lines).

flux integration (Zier & Springel 2022a). We also find that a numerical parameter of $\alpha = 5$ is not enough to obtain sufficiently accurate results for the most optically-thick tests with $\tau_a = 100$. The results presented here adopt $\alpha = 50$ for $aT_0^4/P_0 = 10$, $\tau_a = 100$ test, $\alpha = 20$ for the rest of $\tau_a = 100$ tests, and $\alpha = 5$ for the others. In Figure 10, we present the phase velocity (top panel) and the damping rate (bottom panel) of the waves for different choices of optical depths τ_a and aT_0^4/P_0 . We take the last snapshot of each test, fit the density perturbation with a sinusoidal curve, and obtain the phase and the amplitude, by which we calculate the phase velocity and the damping rate. The results shown (stars) are calculated with resolution 256×256 , and agree with analytical solutions (solid lines). We find no difference between the test results that adopt forced local time-stepping and those that do not (not presented here to avoid duplication).

4.3.3. 1D Radiation Shocks

Shock tube tests are standard tests for non-linear numerical schemes for hydrodynamics and MHD. However, in radiation hydrodynamics or RMHD, the evolution of shocks are more complex, and no analytical solutions can be used to verify numerical results for shock tube tests (Jiang et al. 2012). Therefore, we resort to the steady-state radiation shock test (e.g. Jiang et al. 2012, 2014; Jiang 2021; Menon et al. 2022). The test checks the capability of the code to keep the radiation shock structure calculated from analytical solutions. This is the only time-dependent test where we do not use the moving-mesh or local time-stepping, because we find that the moving-mesh is squeezed near the boundaries such that the mesh construction becomes difficult.

In particular, the setup is almost identical to the radiation shock test in Jiang et al. (2014). We use a 1D slab of length 0.115847 filled by 4096 mesh points and 24 directions cover-

ing the full unit sphere. We set the pre-shock parameters to be $\rho_0 = T_0 = E_{r,0} = 1$ and velocity $v_0 = M$, where we vary the Mach number to be $M = 1.2, 2, 3$. The absorption opacity is chosen to satisfy $\kappa_R = \kappa_P = 577.4/\rho$. We set a non-standard equation of state $P = \rho T/\gamma$ to be consistent with Ferguson et al. (2017), where the adiabatic index is $\gamma = 5/3$. The initial conditions are taken from the analytical solutions (Ferguson et al. 2017), and the intensities are initialized via our time-independent radiation transport calculations. The left boundaries are set to keep the pre-shock quantities, and we use an outflow boundary condition for the right boundary. The constants are set to be $a = 10^{-4}$, $c = 1.73 \times 10^3$.

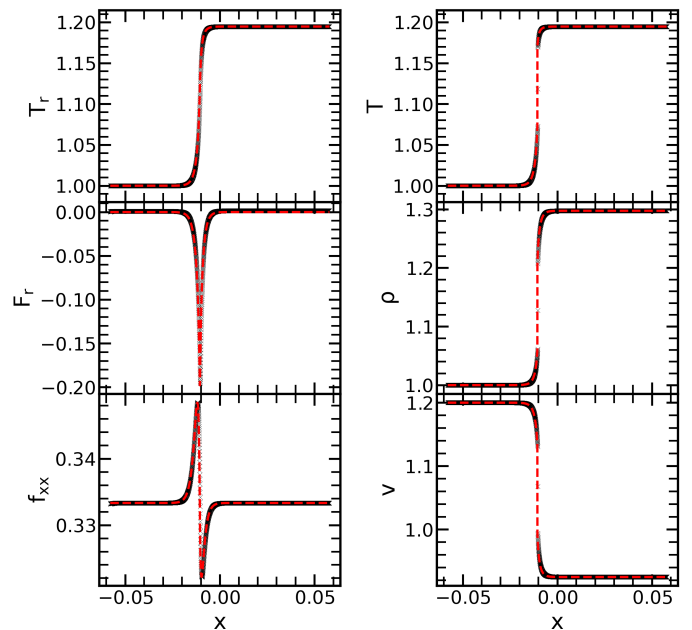


Fig. 11: 1D radiation shock test with Mach number $M = 1.2$. We show the profiles of radiation temperature $T_r = (E_r/a)^{1/4}$, gas temperature T , radiation flux F_r , density ρ , xx component of the Eddington tensor f_{xx} , and velocity v . The simulation results (black) align with the analytical solutions (red dashed).

In Figure 11, 12 and 13, we show the shock structures for Mach number $M = 1.2, 2, 3$, respectively, after three flow-crossing times. Different panels show the radiation temperature $T_r = (E_r/a)^{1/4}$, gas temperature T , radiation flux F_r , density ρ , xx component of the Eddington tensor f_{xx} , and velocity v . The shock structures after three flow-crossing times (black) are identical to the initial profiles (red dashed) calculated from analytical solutions. A common feature is that the radiation fluxes are always pointing from downstream to upstream, which cool the post-shock downstream gas and heat up the pre-shock upstream gas. When the upstream Mach number is close to unity (Figure 11), radiative heating and cooling are not significant so that the gas temperature still increases monotonically from upstream to downstream. However, for Mach number $M = 2$ (Figure 12), the upstream gas near the shock front is heated up and the downstream is cooled, such that the immediate post-shock gas temperature exceeds the far downstream gas temperature, resulting in a spike in gas temperature typically referred to as the Zel'dovich spike (Zel'dovich & Raizer 1967). For both of those cases, the immediate pre-shock gas temperature is still lower than the far downstream gas temperature, which is called a subcritical shock. For Mach number $M = 3$ (Figure 13), the immediate pre-shock

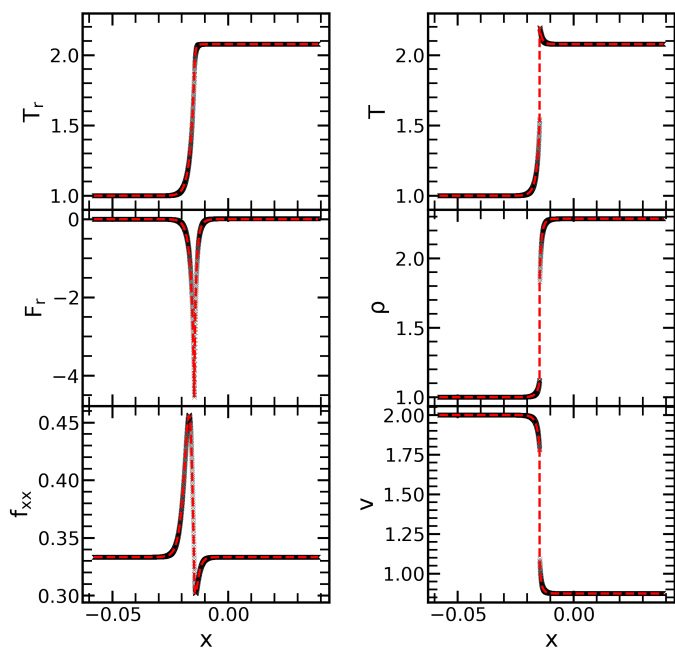


Fig. 12: Same as Figure 11 but for Mach number $M = 2$.

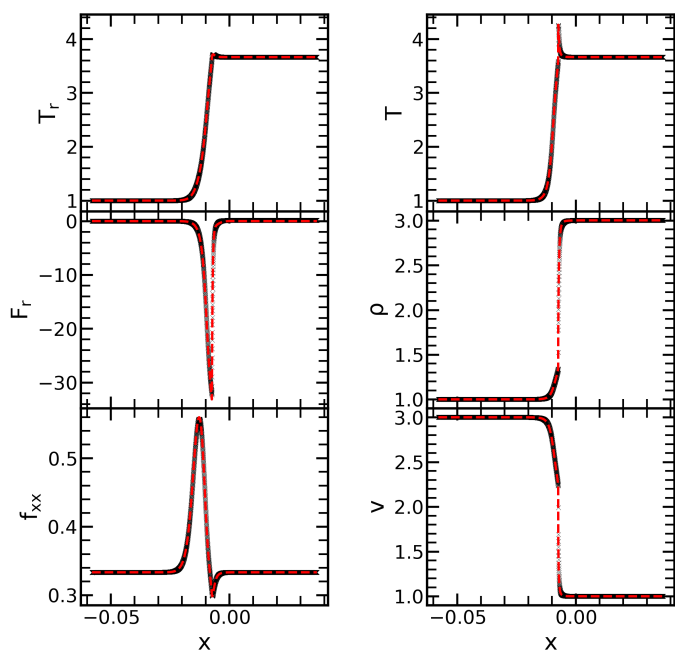


Fig. 13: Same as Figure 11 but for Mach number $M = 3$.

gas temperature becomes the same as the far downstream gas temperature, termed as the supercritical shock. Another common feature is that the Eddington tensor is above $1/3$ at the immediate pre-shock region, but below $1/3$ at the immediate post-shock region, which indicate a jump in radiation pressure at the shock front. The plots can be directly compared with the results in Jiang et al. (2014), which show identical profiles.

4.3.4. 2D Irradiated Cloud

This simplified test demonstrates the capability of our scheme to perform radiation hydrodynamic simulations, where radiative heating has a significant impact on the gas dynamics.

We use the same setup adopted for the 2D shadow test in Section 4.1.4. The relaxed radiation field in the shadow test is used as the initial condition, and we switch on the time-dependent radiation module coupled to the hydro solver to perform a radiation hydrodynamic simulation. We switch on the local time-stepping and allow the code itself to decide the local timesteps. In order to keep the scheme stable, we find it necessary to set a maximum timestep of 0.0003 to limit the timestep jump in neighboring cells to a factor of two. This results in a three-level time-stepping hierarchy.

In Figure 14, we show the density distribution at simulation time $0.06t_0, 0.1t_0, 0.16t_0$, where $t_0 = 1$ is the sound-crossing time-scale across the box. The optically-thick cloud, which is initially in pressure balance with its surroundings, is compressed by a radiation pressure 0.1% of the gas pressure. The surface of the cloud is also heated up, driving an outflow from the irradiated side. Meanwhile, the compressed heated side drives shocks that propagate inwards, which compress the gas further, and eventually destroy the cloud. Our results can be directly compared with figure 5 in J21. The two results are nearly identical, except that our results show sharper edges because we switch on mesh refinement with a target mass resolution $1/(512 \times 256)$ while J21 fixed the mesh without adaptive mesh refinement. Similar simulations can also be found in Jiang et al. (2012) and Proga et al. (2014).

5. Astrophysical Example: Global 3D Convective Envelope of a Red Supergiant Star

To demonstrate the potential of our scheme to simulate complex astrophysical systems, we present a global 3D grey radiation hydrodynamic simulation of a $10 M_\odot$ red supergiant star that simulates the entire convective envelope and simultaneously marginally resolves the stellar photosphere. Such simulation is very challenging because it involves physics with orders-of-magnitude span in both length-scale and time-scale. 3D simulations of red supergiants have been performed before by e.g. Freytag et al. (2002, 2024) and Chiavassa et al. (2011) using the CO5BOLD code (Freytag et al. 2012), and by Goldberg et al. (2022a) using the ATHENA++ code (Stone et al. 2020), which are considered the current state-of-the-art 3D models for red supergiants (Chiavassa et al. 2024).

We show that, with our new scheme, we can surpass the current state-of-the-art in the following ways:

1. We conduct the global 3D simulation for the star that (1) simulates the entire 4π sphere and (2) retains a large simulation box to capture the atmospheric structure. The first point is important for the global convective structure and synthetic interferometric observations (e.g. Chiavassa et al. 2009), whilst the second point is essential for studying wind launching, circumstellar material, and shock breakout (e.g. Goldberg et al. 2022b). The CO5BOLD models achieve the first but not the second, whereas the ATHENA++ models achieve the second but not the first. We manage to attain both because our scheme (a) achieves fast performance that enables global 3D simulations with reasonable computational cost, and (b) supports Voronoi mesh construction in AREPO which enables very flexible mesh sizes.

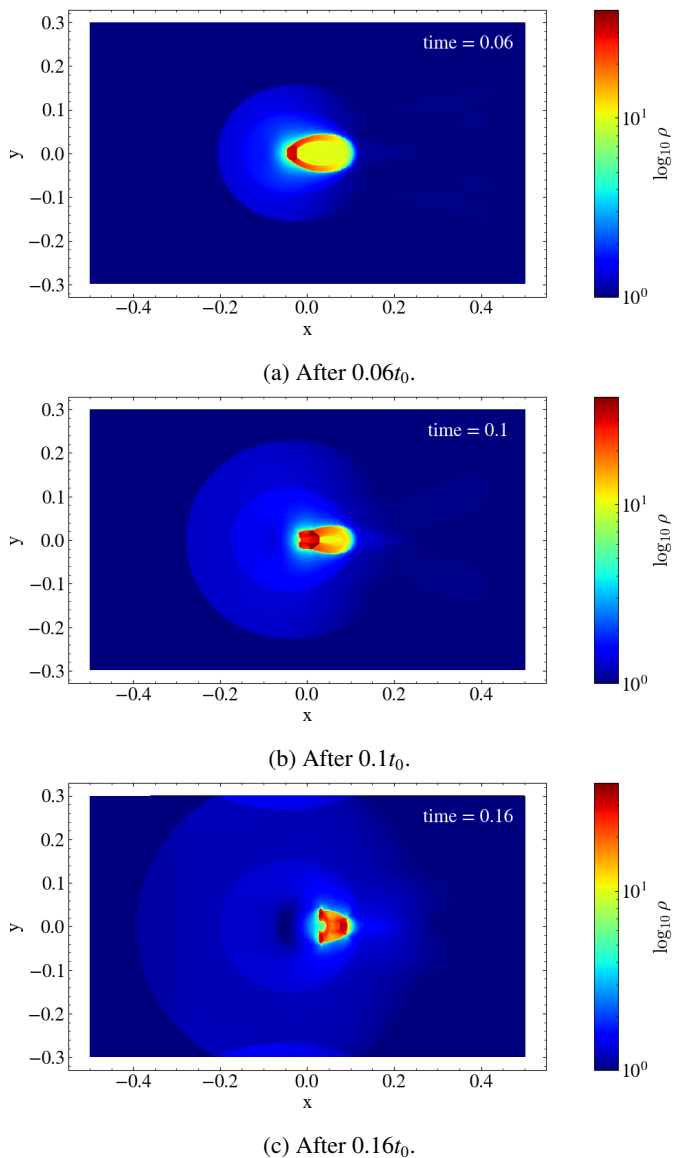


Fig. 14: 2D irradiated cloud test. The plots show the density profile at time $t = 0.06t_0, 0.1t_0, 0.16t_0$, where $t_0 = 1$ is the sound-crossing time-scale across the box. We use the same setup in the 2D shadow test (Section 4.1.4), where we inject two parallel rays of radiation from the left boundary. The radiation acts as a pressure that pushes the cloud. It also heats the cloud on one side, which evaporates the surface and sends out an outflow. In the meantime, the heated side sends in shocks that propagate inside the cloud, which eventually destroy the cloud. The figure can be directly compared to figure 5 in J21.

2. Our simulation include the entire convective envelope down to the bottom.⁴ This is to ensure that the specific entropy of the convective envelope matches the internal condition of

⁴ It is commonly assumed that only simulating the upper part of the convective envelope does not jeopardize the convective structure, because the convection is primarily driven by surface radiative cooling (Stein & Nordlund 1989) and the deep thermal timescale is so high that the bottom envelope is not thermally relaxed even if we can simulate it. Both of these arguments are true. However, if the bottom boundary is not correctly treated, the specific entropy of the efficient convection zone will not be physical, thereby affecting the whole convective envelope.

red supergiants, which is a general challenge that remains to be solved in previous simulations (Chiavassa et al. 2024). We manage to solve this by simulating the entire convective envelope. This is because our scheme supports local time-stepping in AREPO, which allows us to simulate the deep interior of the star where the local dynamical timescale is orders of magnitude lower than the surface dynamical timescale. Local time-stepping in 3D simulations of stellar atmospheres has only been implemented recently (e.g. the DISPATCH framework; Nordlund et al. 2018), albeit only for local box simulations (Eitner et al. 2024) or global simulations with simple cooling functions (Popovas et al. 2022). Here, we illustrate the advantage of local time-stepping in global 3D simulations of stellar surface convection with more accurate radiation transport.

3. We demonstrate that it is possible to marginally resolve the red supergiant photosphere in global 3D simulations, such that the outgoing luminosity matches the input energy source. This is important because it determines the surface cooling rate, which controls the convective structure and the atmospheric temperature. We can achieve this because our scheme (1) supports the flexible Voronoi mesh construction of AREPO that can be easily refined in arbitrary regions, and (2) is accurate in the transition region between optically-thick to thin regimes. Our surface resolution of $1.5 R_\odot$ is 5 times higher than the $8 R_\odot$ surface resolution used in ATHENA++ red supergiant models (Goldberg et al. 2022a), and also slightly higher than the $2 R_\odot$ surface resolution used in latest CO5BOLD red supergiant models (Ahmad et al. 2023). On average, we have 3 cells per photon mean free path at the photosphere, and once in a while 6 cells per photon mean free path during the simulation.

Below we describe the setup and test simulations. We limit ourselves to a brief demonstration. In a separate upcoming paper (Ma et al. in prep.), we will discuss the scientific findings in detail.

5.1. Numerical Setup

For the initial condition, we take a $10 M_\odot$ non-rotating red supergiant star at $Z = 0.02$ metallicity evolved to the stable core helium burning stage using the 1D stellar evolution code MESA (Paxton et al. 2011, 2013, 2015, 2018, 2019; Jermyn et al. 2023). Since the inner part of the star is too dense and therefore too computationally expensive for 3D simulations, we replace the inner $5\% R_{\text{bol,MESA}}$ with a point mass and a modified polytrope of polytropic index $\gamma = 4/3$ that is stably stratified following Ohlmann et al. (2017). Here, $R_{\text{bol,MESA}}$ is the MESA bolometric stellar radius. The star itself is placed at the middle of the simulation box, surrounded by a background filled with low density $\rho_{\text{bg}} = 10^{-17} \text{ g cm}^{-3}$ and low temperature $T_{\text{bg}} = 1800 \text{ K}$ pseudo-vacuum. We choose the box size to be $300 R_{\text{bol,MESA}}$ and use periodic boundary conditions on all sides for the hydrodynamic quantities but not for gravity. Effectively there is no boundary, because only waves exceeding 60 km s^{-1} can reach the box boundary within 20 years of simulation time, while the typical outgoing convective speed is below 30 km s^{-1} .

To supply an energy source and to keep the inner part stable during the simulation, we introduce an ‘artificial core’ region in our simulation (inner $7\% R_{\text{bol,MESA}}$) that extends beyond the radius where we modified the initial profile. Within the artificial core, we apply a constant radiative luminosity ($10^{4.6} L_\odot$, the surface luminosity of the MESA profile taken as the initial condition) to the radiation transport module. This is achieved by using a ra-

radiation flux profile that follows $F_r = L_{s,\text{MESA}}/(4\pi r^2)$, where r is the distance from the center and F_r is the radial component of the radiation flux. The intensities are constructed such that the radiation energy density is in equilibrium with local temperature T and gives the correct radiation flux F_r assuming Eddington approximation, i.e., $I_n = caT^4/(4\pi) + 3F_r(\mathbf{n}_n \cdot \hat{\mathbf{r}})/(4\pi)$, where $\hat{\mathbf{r}}$ is the unit vector along the radial direction. Inside the artificial core, we also actively damp the core velocities throughout the simulation, such that $\rho\dot{\mathbf{v}} = -\rho\mathbf{v}/\tau_c$, where we choose a damping timescale τ_c to be 5% of the global sound-crossing timescale of the MESA star. We find that the core damping is necessary to keep the hydrostatic structure of the core beyond 150 global dynamical timescales. We note that this artificial core sits well within the radiative zone (inner 12%), below the convective envelope in the 1D profile. We therefore simulate the entire convective envelope and a part of the radiative zone below in our computational domain.

For the production run shown here, we use the *time-independent* version of our scheme, where we assume the transport term exactly balances the source terms and solve Equation (127). This is still valid for non-relativistic simulations such as the simulation presented here. We find that it is still necessary to implicitly evolve the temperature field simultaneously with the radiation field. We include the radiation energy and radiation pressure assuming LTE in the equation of state for density $\rho > 10^{-8} \text{ g cm}^{-3}$ and smoothly transit to a pure gas equation of state for density $\rho < 10^{-10} \text{ g cm}^{-3}$, such that the radiation is not included in the equation of state in the optically-thin regime. In the hydrodynamic solver, we include the radiation source terms in the energy equation for radiative heating/cooling, and only include them in the momentum equation for $\rho < 10^{-8} \text{ g cm}^{-3}$ with a compensating transition region between $10^{-10} - 10^{-8} \text{ g cm}^{-3}$ to take into account the possible radiation forces in the optically-thin regime. Given that the radiative diffusion timescale is orders of magnitude larger than the local timesteps, we only switch on the radiation transport module on the globally synchronised timesteps to save computational time. At local timesteps that are not synchronised, we only evolve the hydrodynamics and not the radiation field in active cells. This approach does not guarantee energy or momentum conservation, but as we show in Figure 15, it does not lead to significant deviations from conservation laws. We have also attempted to use the time-dependent version of our scheme with local time-stepping on the moving mesh, which did not introduce notable errors by the scheme itself. However, we find that the inner boundary condition for the time-dependent radiation transport module is difficult to set while keeping the inner core region stable for more than 50 sound-crossing timescales. We therefore choose to use the time-independent scheme, and defer the possibility of using the time-dependent scheme to future explorations.

Radiation transport is performed with 80 directions. This is slightly smaller than the 120 directions adopted in the ATHENA++ red supergiant simulation (Goldberg et al. 2022a), but we find that it does not lead to significant ray-effects. This is demonstrated in Figure 16, where 24 or 48 directions lead to noticeable radiation peaks in the optically-thin atmosphere of the star. Since the radiation is coupled to the temperature field, this also leads to peaks in temperature field in the stellar atmosphere later on in the simulations. We thus choose 80 directions to save computational cost and memory cost while avoiding significant ray-effect.

The simulation includes full self-gravity, uses the OPAL equation of state (Rogers & Nayfonov 2002), and Rosseland and Planck opacities κ_R, κ_P from high-temperature Los Alamos

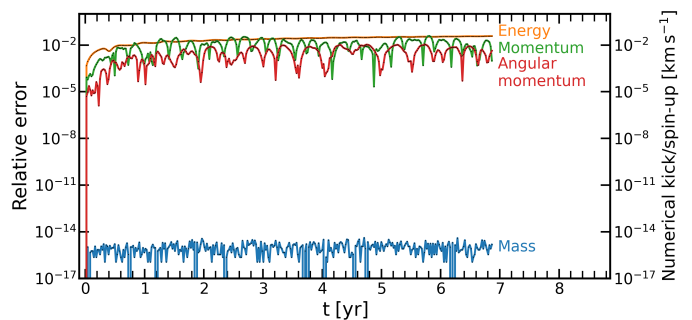


Fig. 15: Relative error in conserved global quantities as functions of time for the $10 M_{\odot}$ 3D AREPO red supergiant model. The total mass (blue) is conserved to near machine precision. As we apply the damping term in the artificial core, the total energy (thermal + radiation + kinetic + gravitational potential), momentum, and angular momentum are not expected to be conserved. Therefore, we observe a relative error at the order of 1% in total energy (orange) compared to its initial value. The momentum and angular momentum are initialized to be zero, so the concept of relative error is not applicable. Here, we normalize the momentum along the z axis by $M_{\text{MESA}}v_0 = 2 \times 10^{39} \text{ g cm s}^{-1}$, and normalize the angular momentum along the z axis by $0.1 M_{\text{MESA}} R_{\text{bol,MESA}} v_0 = 5.3 \times 10^{51} \text{ erg s}$, where we take a reference $v_0 = 1 \text{ km s}^{-1}$. The green and red curves therefore indicate that the star receives a fluctuating numerical ‘kick’ along the z axis of about 0.01 km s^{-1} , and a fluctuating numerical ‘spin up’ along the z axis of about 0.01 km s^{-1} or $10^{-11} \text{ rad s}^{-1}$, which are negligible compared to their normal values of any physical origin for red supergiants.

OPLIB table (Colgan et al. 2016)⁵ blended with low-temperature Ferguson et al. (2005) table⁶. We assume $\kappa_E \approx \kappa_P$ and $\kappa_F \approx \kappa_R$, which are not good approximations in the optically-thin regime. But this is the standard approach for 3D grey simulations of stellar atmosphere (Freytag et al. 2012; Goldberg et al. 2022a). We enable local time-stepping for hydrodynamics and gravity on the moving Voronoi mesh in the simulation, which is the main reason that we can afford to run simulations that include the entire convective envelope.

To pass the initial relaxation phase of the simulation, we change the damping terms and the surface resolution during the relaxation. For the initial 10 dynamical timescales of the star, we apply a global damping term to the momentum across the simulation box to aid relaxation following Ohlmann et al. (2017). We drop the global damping afterwards, but we keep the strong damping in the artificial core until the end of the simulation. We use a target mass resolution of $3.4 \times 10^{-6} M_{\odot}$. We have checked that this leads to sufficient resolution near the artificial core, but not sufficient to resolve the stellar surface. We therefore adopt several nested layers for the maximum cell volume as the (de-)refinement criterion. In the spherical shell between $0.2 - 3 R_{\text{bol,MESA}}$, we further constrain the maximum cell size to be $7.4 R_{\odot}$. We find that this is still not enough to resolve the photosphere, in a sense that the outgoing luminosity from the 3D simulation is two times larger than the input luminosity in the artificial core. Therefore, after about 25 global dynamical timescale of the MESA star, we further decrease the maximum cell

⁵ <https://aphysics2.lanl.gov/apps/> The opacity due to electron scattering is included in the Rosseland opacity table.

⁶ https://www.wichita.edu/academics/fairmount_las/physics/Research/opacity.php

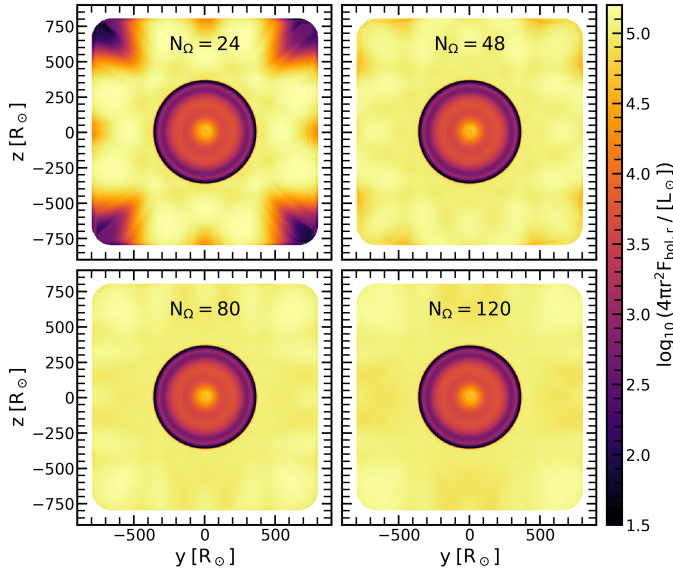


Fig. 16: Demonstration of the ray-effect in the $10 M_{\odot}$ 3D AREPO red supergiant model. Different panels show 2D slices of the star when the number of directions N_{Ω} in the radiation transport module is taken as 24, 48, 80, 120. The color shows the radial radiative luminosity $4\pi r^2 F_{\text{bol},r}$. Inside the star, the radiation is close to the diffusion limit, and the radiative flux is not sensitive to the number of directions chosen. Across different panels, the radiative fluxes inside the star agree with each other at a relative error below 10^{-10} . However, in the optically-thin atmosphere of the star where radiation propagates freely, a small number of directions lead to radiation peaks along the discretized directions. We generally do not find significant ray-effect for $N_{\Omega} = 80$ and 120.

size to be $2 R_{\odot}$ between $0.9 - 1.5 R_{\text{bol,MESA}}$, and $1.5 R_{\odot}$ between $0.95 - 1.15 R_{\text{bol,MESA}}$. We find that this is enough to marginally resolve the stellar photosphere, in a sense that the time-averaged outgoing luminosity matches the input.

5.2. Results

The relaxation process is shown in the bolometric lightcurve of the 3D AREPO red supergiant model in Figure 17, where we show the bolometric luminosity L_{bol} as a function of time. The bolometric luminosity is calculated by taking the radial component of the radiation flux from the AREPO output (denoted as $F_{r,r}$), and averaging the quantity $4\pi r^2 F_{r,r}$ over all the cells between $4 - 5 R_{\text{bol,MESA}}$, where r is the distance from each cell to the box center.⁷ Eventually after 3.5 yr, the 3D star reaches a steady state, as shown in the zoom-in plot in Figure 17. On top of other variability, the bolometric luminosity exhibits a regular pulsation pattern around the input luminosity value. The pulsation is likely driven by the κ -mechanism (Eddington 1917; Cox & Whitney 1958; Baker & Kippenhahn 1962; Zhevakin 1963) where the opacity increases with temperature due to hydrogen recombination (Heger et al. 1997; Joyce et al. 2020), but detailed analyses are deferred to future work.

⁷ Alternatively, it may seem more intuitive to calculate the bolometric luminosity by integrating the normal radiation flux over all the box boundaries. However, since the box boundary is far away from the star with very low resolution, it is more accurate to calculate the luminosity closer to the star, as we describe in the main text.

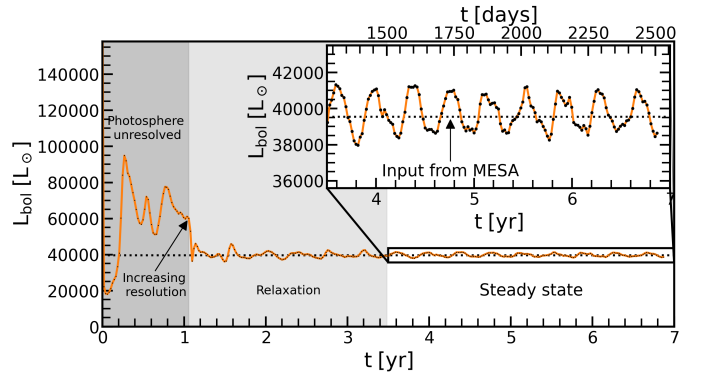


Fig. 17: Bolometric lightcurve of the $10 M_{\odot}$ 3D AREPO red supergiant model. We start the simulation at time $t = 0$. During the initial relaxation phase $t = 0 - 1.1$ yr, the resolution near the stellar surface is not enough to resolve the photosphere, and the bolometric luminosity L_{bol} does not saturate around the input luminosity (dotted black horizontal line). Therefore, at $t = 1.1$ yr (indicated by the arrow), we suddenly increase the surface resolution from $7.4 R_{\odot}$ to $1.5 R_{\odot}$. We find that this is enough for L_{bol} to drop to the target value. After $t > 3.5$ yr, the bolometric luminosity settles into a regular variable state around the input luminosity, as shown in the zoom-in plot. The black dots on the orange line show the snapshots used to draw the lightcurve, which are equally spaced by 7.6 days. The overall variability is likely due to the self-excited pulsation of the model, which merits further analyses.

Taking a steady-state simulation snapshot at time 3.4 yr, we show different timescales and optical depth as functions of radial coordinates in Figure 18. We compute the shell-averaged timescales through radial binning, i.e., taking the average value of quantities in small bins of radial coordinates, weighted by either mass or volume. The shell-average of quantity q weighted by mass is denoted as $\langle q \rangle_m(r) \equiv \left[\sum_{|r_i - r| < \delta R/2} (q_i \times \Delta m_i) \right] / \left[\sum_{|r_i - r| < \delta R/2} \Delta m_i \right]$, where Δm_i is the mass enclosed in each cell, $\delta R = R_{\text{bol,MESA}}/1000$ is the size of the bin, and the sum is taken over all the cells i whose radial distance r_i from the center fall into the bin. Similarly, the shell-average of quantity q weighted by volume is denoted as $\langle q \rangle_V(r) \equiv \left[\sum_{|r_i - r| < \delta R/2} (q_i \times \Delta V_i) \right] / \left[\sum_{|r_i - r| < \delta R/2} \Delta V_i \right]$, where ΔV_i is the volume enclosed in each cell. We define the shell-averaged convective timescale $\langle t_{\text{conv}} \rangle$, radial pressure scale height $\langle H_p \rangle$, thermal timescale $\langle t_{\text{th}} \rangle$, and Rosseland optical depth $\langle \tau_{\text{Ross}} \rangle$ as follows:

$$\langle t_{\text{conv}} \rangle(r) \equiv \frac{\alpha_{\text{MLT}} \langle H_p \rangle(r)}{\sqrt{\langle v_r^2 \rangle_m(r)}}, \quad (132)$$

$$\langle H_p \rangle(r) \equiv - \left(\frac{\langle \nabla P \cdot \hat{r} \rangle_V}{\langle P \rangle_V} \right)^{-1}, \quad (133)$$

$$\langle t_{\text{th}} \rangle(r) \equiv \frac{\sum_{r_i > r} (c_p T \Delta m)_i}{L_{\text{bol}}}, \quad (134)$$

$$\langle \tau_{\text{Ross}} \rangle(r) \equiv \sum_{r_i > r} \left[\frac{(\kappa_R + \kappa_s) \Delta m}{4\pi r^2} \right]_i, \quad (135)$$

where c_p is the specific heat capacity at constant pressure, \hat{r} is the unit vector in the radial direction and we take $\alpha_{\text{MLT}} = 3$. The pulsation period is found by taking the Fourier transformation of the relaxed bolometric light curve (Figure 17) and identifying the period of the highest peak in the power spectrum.

In Figure 18, we shade the artificial core in grey, and only analyze the regions outside of the artificial core. Throughout the convective envelope, the convective timescale (blue) is mostly comparable with the pulsation period (black). This indicates that convection will interact with pulsation, and 1D treatments of both processes may not be adequate to capture the physics. The thermal timescale (red) is smaller than the convective timescale at the top of the convective envelope, but is still orders of magnitude larger at the bottom of the envelope. This is beyond reach for the total simulation time (grey dotted horizontal line). However, we argue that it does not mean the inner part of the envelope is out of thermal equilibrium in 3D simulations. As long as we start the simulation from a profile close to the real thermal equilibrium state, it is unlikely for the simulation to deviate too much from reality. This is why it is essential to take the initial condition from a 1D stellar evolution code, as opposed to relaxing the simulation from a previous 3D simulation of different parameters (as done e.g. in C05BOLD simulations; Ahmad et al. 2023). Nevertheless, the simulation duration is still an order of magnitude larger than the convective timescale and the pulsation period, and therefore the simulation is dynamically relaxed to the steady state. We further show the scatter plot of local timesteps taken by all the cells in the simulation. The smallest timestep is taken by the innermost cells in the artificial core. The bottom of the convective envelope takes a timestep 16 times smaller than the largest timestep in the outer envelope. This is why simulating the entire envelope is beyond reach for 3D codes that only employ global time-stepping.

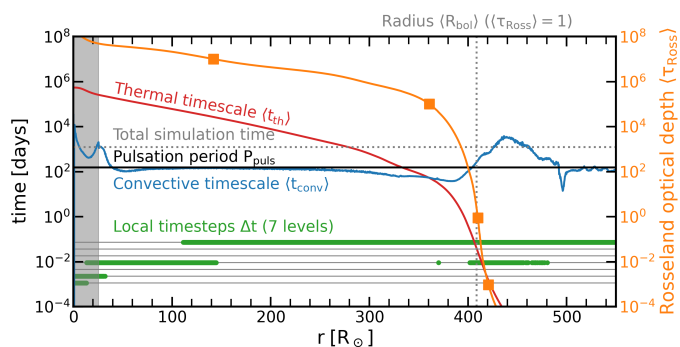


Fig. 18: Shell-averaged timescales and Rosseland optical depth profile of the $10 M_{\odot}$ 3D AREPO red supergiant model at time 3.4 yr. We show the local timestep distribution in green that occupies 7 levels of hierarchy, which enables us to simulate the entire convective envelope. The artificial core within $7\% R_{\text{bol,MESA}}$ is shaded in grey (see main text). We further show different timescales across the envelope: the convective timescale (blue), pulsation period (black), and thermal timescale (red), as defined in the main text. The smallest timestep is 5 orders of magnitude smaller than the convective timescale and the pulsation period, and 6 orders of magnitude smaller than the total simulation time, which showcases the vast range of timescales covered in the simulation. In orange, we show the shell-averaged Rosseland optical depth $\langle \tau_{\text{Ross}} \rangle$, which is a steep function of radial coordinate near the bolometric photosphere (grey dotted vertical line, defined as where $\langle \tau_{\text{Ross}} \rangle = 1$). We mark different optical depths in orange squares to indicate the approximate locations of the 2D maps shown in Figure 19.

In Figure 18, we further show the shell-averaged Rosseland optical depth (orange). We mark the averaged bolometric photosphere (grey dotted vertical line), defined as where the

grey optical depth reaches unity. From outside the grey stellar photosphere to just beneath the photosphere, the optical depth increases steeply by more than 10 orders of magnitude. It is therefore essential to have enough resolution near the photosphere to resolve the region where photons escape. Here, we only marginally resolve this region such that the outgoing luminosity matches the input. We also mark the location of $\langle \tau_{\text{Ross}} \rangle = 10^7, 10^5, 1, 10^{-3}$ with orange squares, where we take the simulation data to plot the tomography of the star in Figure 19. Besides the highest optical depth $\langle \tau_{\text{Ross}} \rangle = 10^7$ that is located at about $1/3$ stellar radii, all the others are located rather close to the photosphere. But as we show in Figure 19, they display distinct flow patterns across different optical depths.

The fact that we simulate the entire envelope while marginally resolving the photosphere means that we can resolve the flow patterns both in the deep convection envelope and in the atmosphere. In Figure 19, we present a tomography of our 3D AREPO red supergiant model probed at different layers of optical depths along the x axis. We take a model snapshot in the steady state at 3.4 yr, interpolate it onto a Cartesian grid, and calculate the Rosseland optical depth $\tau_{\text{Ross},x}(x, y, z) = \int_{-\infty}^x \rho(x, y, z)(\kappa_{\text{R}} + \kappa_{\text{s}})(x, y, z) dx$ by integrating along the x axis from infinity to negative infinity. In Figure 19, we scan through different optical depths from the deep stellar interior to the bolometric photosphere, and eventually into the stellar atmosphere. As illustrated in Figure 19, none of the temperature maps looks alike across different optical depths. This is in part because radiative cooling and heating gradually becomes important compared to adiabatic expansion as a fluid parcel travels from the deep convective envelope to the upper stellar atmosphere, which will be detailed in the upcoming paper (Ma et al. in prep.). The distinct morphology across optical depths will have profound implications for interpreting spectroscopic and interferometric observations of red supergiants, which will be explored in the future.

6. Discussion on Caveats and Directions for Future Development

6.1. From Grey to Multigroup

The radiation transport scheme described in this work is currently limited to the grey approximation, where the frequency-integrated Rosseland and Planck opacities are used to calculate the bolometric intensities. However, in many astrophysical scenarios, different radiation sources emit in distinct frequency bands. For example, for irradiated exoplanets such as hot Jupiters, the radiation from internal heating is released in infrared (IR), whereas the irradiation from the host star is concentrated in optical (Guillot 2010). For problems involving photoionization and photo-dissociation such as protoplanetary disks (e.g. Woitke et al. 2016), star formation (e.g. Chon et al. 2024) or the epoch of reionization (e.g. Stark 2016), strong ultraviolet and X-ray radiation is emitted from (proto)stars which ionize surrounding atoms and dissociate molecules, while in the meantime the dust absorbs the optical and UV radiation and re-emits in IR. For tidal disruption events, the optical/UV emission and X-rays are observed to have distinct blackbody temperatures and thus emitted from distinct regions (Gezari 2021). In general, grey frequency-integrated opacities based on the Planck function are merely crude approximations in the optically-thin regions (Malygin et al. 2014; Jiang 2022, 2023), and frequency-dependent opacities are needed for more accurate treatments.

Since the frequency-by-frequency radiation transport is too expensive even in 1D simulations, it is more feasible to adopt a

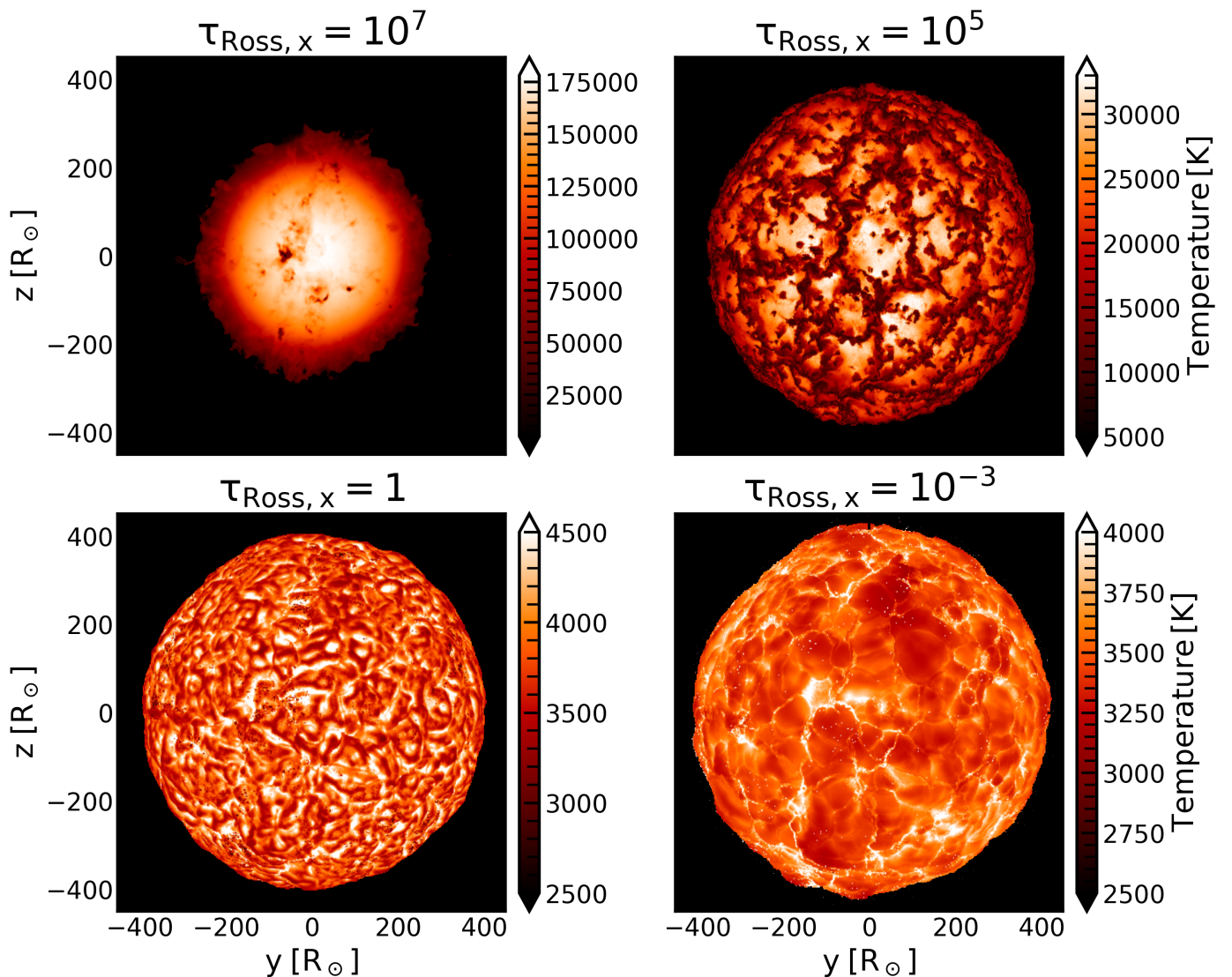


Fig. 19: Tomography of the $10 M_{\odot}$ 3D AREPO red supergiant model showing 2D temperature maps at different optical depths at time 3.4 yr. We scan through the star along the x axis, taking the integrated Rosseland optical depths of 10^7 , 10^5 , 1 , 10^{-3} . The optical-depth tomography scans from deep inside the star all the way to the atmosphere outside of the bolometric photosphere. The convective pattern changes substantially. This plot highlights the importance of simulating the entire convective envelope and simultaneously marginally resolving the photosphere, which gives us the unprecedented advantage of obtaining the first comprehensive picture of red supergiants from deep inside to high up in the atmosphere, with significant consequences for observational signatures.

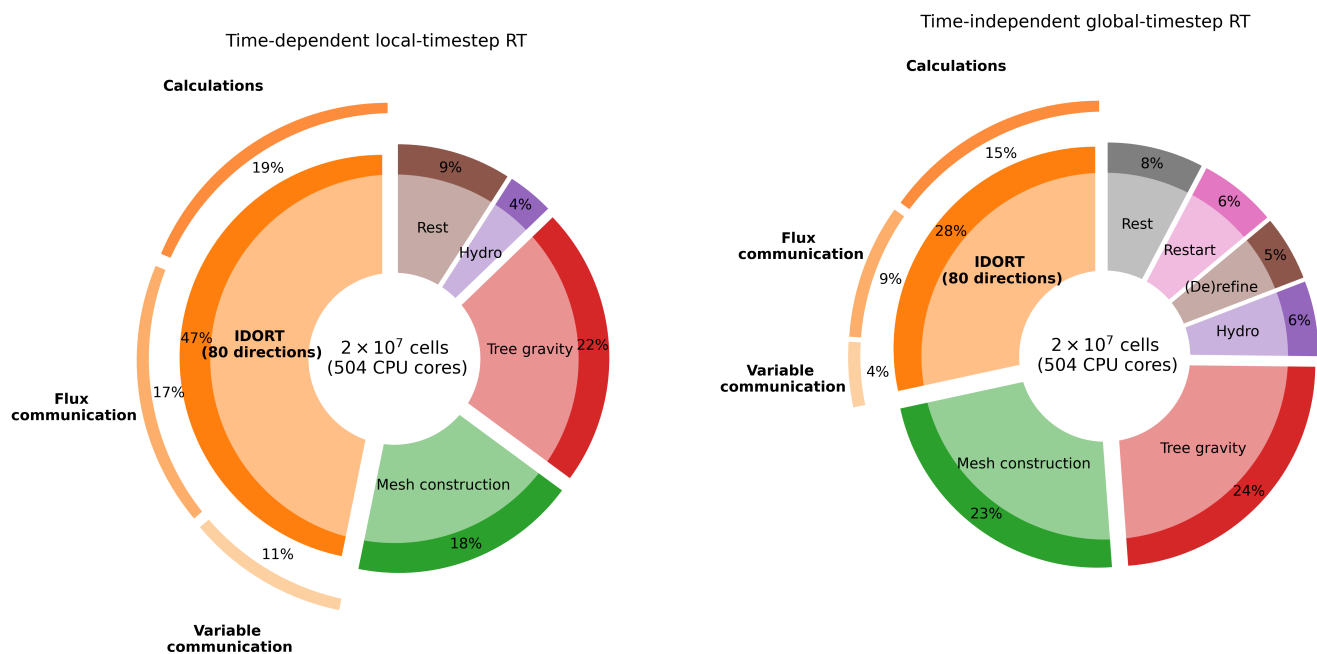
multigroup approach by solving the radiation transport in several frequency bins (Mihalas & Mihalas 1984). The implicit discrete ordinates scheme in J21 has already been extended to multigroup with Compton scattering in Jiang (2022). The multigroup extension in ATHENA++ was successfully applied to accretion disks around AGN (Secunda et al. 2024) and stellar-mass black holes (Mills et al. 2024), which demonstrates the potential of the scheme. Given that the multigroup extension does not require a structured static mesh, we expect that it will be straightforward to extend our scheme to multigroup.

6.2. From Fast to Faster: GPU Acceleration and Node-to-node Communication

The speed of our scheme depends on the specific problem. But in general, the computational cost is approximately proportional to $O(N_p N_{\Omega} N_{\text{iter}})$, where N_p is the number of cells, N_{Ω} the number

of angles, and N_{iter} the number of iterations to reach the convergence criterion.

To demonstrate that our method can be fast for complex 3D simulations, in Figure 20 we show the fraction of CPU hours spent by each module in AREPO for the 3D red supergiant simulation described in Section 5. With $N_p = 2 \times 10^7$, $N_{\Omega} = 80$, $N_{\text{iter}} = 10$, we find that the radiation module takes about 47% of the computational cost, whilst 18% is spent on tree-particle-mesh gravity, 22% on Voronoi mesh construction, and 4% on the hydro solver. This means that, in this complex 3D example, including radiation only increases the computational cost by a factor of two, and even less if the radiation transport is only applied at the globally synchronised timestep. If our scheme were to be applied to a simplified 3D simulation on a fixed mesh with a simple treatment of gravity, a RMHD simulation is 10 – 20 times as expensive as a pure MHD simulation, which is the typical cost of accurate on-the-fly radiation transport.



(a) For time-dependent version of the radiation module applied at each local timestep.

(b) For time-independent version of the radiation module applied only at the globally synchronised timestep.

Fig. 20: Percentage of CPU hours spent by each module in AREPO for the 3D red supergiant simulation in Section 5. With 80 directions, the *time-dependent* version of the radiation transport module takes about 1/2 of the computational cost if applied at each local timestep. The *time-independent* version of the radiation transport module takes only 1/4 of the total computational cost if applied only at the highest timestep, and most of the costs are still dominated by the standard gravity solver and mesh construction in AREPO.

Such performance is in fact very fast considering that we use 80 angles. For reference, the explicit M1 radiation transport AREPO-RT with 3 frequency bins (Kannan et al. 2019) takes 50% of the computing time in the THESAN-1 reionization simulation on CPUs (Zier et al. 2024a). The relative cost of our scheme is similar, but our reported cost adopts a large number of 80 angles. It should be noted though that our scheme will be much less efficient for reionization simulations due to the large number of iterations needed for optically-thin regions. The general relativistic extension of the J21 scheme was reported to occupy 80% – 96% of the total cost for 3D linear wave tests with 128 angles (including communications; White et al. 2023), which is comparable to our scheme. Using the J21 scheme to simulate circumbinary disks, Tiwari et al. (2025) reported that the RMHD simulation is an order of magnitude more expensive than the MHD simulation, also consistent with our estimate for fixed-mesh simulation without self-gravity.

A useful comparison to make is between the cost of 3D red supergiant simulations in ATHENA++ and that of AREPO, where the physical processes are similar despite different setups. Using the scheme of J21 in ATHENA++, Goldberg et al. (2022a) reported that each 3D red supergiant simulation of 16-year duration takes two months to finish on 80 skylake nodes on Pleiades supercomputer, or about 10 million CPU hours. In comparison, given the current CPU usage, our simulation of 16-year duration will take one month to finish on 504 CPU cores (7 nodes) on the NHR@FAU Fritz supercomputer, or about 0.4 million CPU hours, which is 25 times cheaper than the ATHENA++ simulation. It should be noted that this speed difference is largely due to different setups. Even though our simulation uses more expensive gravity and mesh construction modules with more mesh points,

Goldberg et al. (2022a) used a more stringent convergence criterion for the radiation transport.⁸ The communication overhead due to a larger number of CPU cores used in Goldberg et al. (2022a) may also play a role in the difference of computational cost. Therefore, we conclude that our red supergiant simulation with AREPO is at least not slower, if not faster, compared to Goldberg et al. (2022a) with ATHENA++.

The fast performance of our scheme is largely because of our optimized iterative solver and communication between tasks. The iterative solver for the intensities effectively solves for a linear system where the intensities can be grouped into a long vector and the coefficients form a large matrix. Those coefficients do not change during iterations, and thus only need to be calculated once and then saved to be directly used in later iterations, as motivated by Whitehouse et al. (2005).⁹ This approach helps reduce the cost for actual calculations without heavily burdening the memory load. After optimizing the actual calculations, the cost of the radiation module is dominated by the communication

⁸ We use full self-gravity and adaptive Voronoi mesh construction with 2×10^7 total mesh points in AREPO. This setup is supposed to be much more expensive than the ATHENA++ setup in Goldberg et al. (2022a), where they used spherically-averaged gravity without adaptive mesh refinement and 10^7 total mesh points. On the other hand, we stop the iterative solver after 10 iterations, which typical yields a relative error of $10^{-4} - 10^{-5}$. In comparison, Goldberg et al. (2022a) stop the iteration after the relative error reaches 10^{-6} , which sometimes takes 20–50 iterations (Y.-F. Jiang, priv. comm.).

⁹ For specific problems such as fast transients, star formation, or reionization, the opacity also needs to be updated together with radiation and temperature field, and different coefficients are needed. This is to be explored in the future.

between tasks, where we need to exchange primitive variables as well as fluxes. In the procedure described in Section 3.4, we have optimized our scheme such that there is no redundant variable exchange or flux exchange. Specifically, (1) we only exchange fluxes and not the radiation primitive variables (intensities) when we pre-calculate the coefficients. (2) During each iteration, we exchange the intensities, and then only exchange neighboring fluxes for I_c and not the conserved variables IV . (3) After the iterations, we exchange the intensities, and then only apply fluxes for active-passive faces to update the conserved variables IV for passive cells with neighboring active cells.

Despite the fast performance, the radiation module will dominate the computational cost if we aim for multigroup radiation (Section 6.1), since the cost will be at least multiplied by the number of frequency bins N_ν . The true cost will be even higher because more iterations may be needed to reach convergence. Although it is possible to reduce the number of angles as a compromise, it is not advisable to reduce the number of angles below 48 for complex 3D simulations, especially when there are optically thin regions in the simulation (see e.g. the convergence tests in Huang et al. 2023; Zhang et al. 2024). We therefore expect that radiation module will dominate the computational cost for more than 3 frequency bins.

A possible solution was given in Zier et al. (2024a), where they ported the M1 radiation transport AREPO-RT (Kannan et al. 2019) onto GPUs with node-to-node communications and achieved a factor of 10 – 20 speedup. Typically, GPUs are much more efficient than CPUs when dealing with millions of simple and identical operations that can be performed independently in parallel. This is especially relevant for our scheme, since we need to calculate the intensity per cell per angle per frequency bin, which yields $O(N_p N_\Omega N_\nu)$ almost identical operations. Furthermore, the cost of our implementation is still dominated by task-to-task communication, which exchanges information between different cores. With modern computing nodes with over 100 cores per node, using shared memory within each node and only performing node-to-node communication can significantly reduce the computational cost spent in communication. Since the subcycling approach in explicit M1 AREPO-RT is in its essence very similar to the iterative solver in our scheme, the data structure and workflow in Zier et al. (2024a) can be mostly adopted for our scheme. Such acceleration techniques will be explored along with the multigroup extension.

6.3. Convergence Criterion and Iterative Solver

The convergence criterion used in this work

$$\frac{\sum_{i=0}^{N_p-1} \sum_{n=0}^{N_\Omega-1} |I_{n,i}^{m+1,l+1} - I_{n,i}^{m+1,l}|}{\sum_{i=0}^{N_p-1} \sum_{n=0}^{N_\Omega-1} |I_{n,i}^{m+1,l+1}|} < \epsilon \quad (136)$$

is directly inherited from J21. However, it has two limitations. First, it only constrains part of the simulation domain where the intensities are large, which typically happens in the high-density optically-thick regions. Second, it only checks whether the relative error between two sequential iterations l and $l+1$ is small, i.e., whether the iterations have converged to a solution, but it does not check how well the converged solution satisfies the original radiation transport equation (70). Therefore, it is important to further check the residual of the radiation transport

equation

$$\begin{aligned} \delta(IV)_{n,i}^{m+1} \equiv & [I_n^{m+1} V^m - (IV)_n^m]_i + \sum_{j=0}^{N_i-1} [I_n(c\mathbf{n}_n - \mathbf{w})]_{ij}^{m+1} \cdot A_{ij}^m \Delta r_{ij}^m \\ & - [(S_I)_n^{m+1} V^m c \Delta t^m]_i. \end{aligned} \quad (137)$$

Specifically, since the radiation source terms are the relevant quantities for 3D simulations in practice, we propose to check the relative residuals of the zeroth (radiation energy) and first moments (radiation flux) of the radiation transport equation

$$\frac{\sum_{i=0}^{N_p-1} |\delta(E_r V)_i^{m+1}|}{\sum_{i=0}^{N_p-1} |(E_r V)_{n,i}^m|} < \epsilon_{E_r V}, \quad (138)$$

$$\frac{\sum_{i=0}^{N_p-1} |\delta(\mathbf{F}_r V)_{n,i}^{m+1}|}{\sum_{i=0}^{N_p-1} |(\mathbf{F}_r V)_i^m|} < \epsilon_{\mathbf{F}_r V}, \quad (139)$$

where

$$\delta(E_r V)_i^{m+1} \equiv \frac{4\pi}{c} \sum_{n=0}^{N_\Omega-1} \delta(IV)_{n,i}^{m+1} w_n, \quad (140)$$

$$\delta(\mathbf{F}_r V)_i^{m+1} \equiv 4\pi \sum_{n=0}^{N_\Omega-1} \delta(IV)_{n,i}^{m+1} \mathbf{n}_n w_n. \quad (141)$$

For the 3D simulation presented in Section 5, we typically find relative errors at the order of 10^{-3} in radiation energy and 10^{-2} in radiation flux after 10 iterations. This is because we have chosen a robust iterative solver with a relatively slow convergence speed as the default solver and that the radiation field does not change significantly. As already discussed in the Appendix of J21, if we do not separate the positive coefficients from negative ones for the diagonal terms (see Section 3.3), the convergence speed will be much faster. If we adopt this alternative solver that converges faster, the relative errors are at the order of 10^{-7} in radiation energy and 10^{-3} in radiation flux after 10 iterations. However, we do find that this alternative solver is prone to divergence for the 3D simulation in Section 5. Therefore, we have chosen to keep the original iterative solver as the default one, but bear in mind that this leads to slow convergence and relatively larger errors in radiation energy and flux. We have also chosen to keep the original convergence criterion (maximum 10 iterations on top of Equation (121)) as the default one, but print the relative residuals in the terminal output for debugging purposes. One future direction is to find an alternative implicit solver that converges faster, which is further discussed in the next subsection.

6.4. Faster Convergence and Higher-order Accuracy: Alternative Implicit Solvers

The computational cost of our scheme almost scales with the number of iterations N_{iter} . To correctly capture the radiation field in the optically-thin regions, a large N_{iter} is typically needed (see e.g. test problems 4.1.1, 4.1.3, 4.2.2). It is thus desirable to accelerate the convergence of the implicit scheme. Furthermore, our scheme is only first-order accurate both in time and space, as directly inherited from the J21 scheme. As explained in J21, this is to avoid oscillatory behaviors when the source terms are stiff and when flux-limiters for higher-order spatial reconstruction are difficult to treat implicitly. However, the low-order accuracy renders the scheme diffusive (see e.g. test problems 4.1.1 and 4.2.2).

A potential direction for the future is to look for alternative implicit solvers that have been successfully applied to other astrophysical problems. For example, implicit methods are also adopted to simulate compressible low-Mach stellar convection, e.g., the SEVEN-LEAGUE HYDRO code (Miczek et al. 2015; Leidi et al. 2022) or the MUSIC code (Viallet et al. 2016; Goffrey et al. 2017). The Crank-Nicolson time-integration used in those codes yields second-order accuracy in time, but it remains to be explored how to incorporate it with the moving-mesh construction in AREPO (Pakmor et al. 2016). Second-order spatial reconstruction was also shown to be possible with implicit schemes adopting Newton-Raphson methods with preconditioners (Viallet et al. 2016; Leidi et al. 2022), but saving the gradients will pose a serious challenge to memory load. Furthermore, since the Jacobian matrix for our radiation transport problem is huge, it is attractive to adopt a Jacobian-free method to avoid overloading the memory (e.g. Viallet et al. 2016), although the construction of a preconditioner and massive parallelization are challenging to realize compared to the iterative solver adopted in this work.

6.5. Heavy Memory Load for Large Simulations

Large simulations such as cosmological simulations are usually bound by physical memory (Weinberger et al. 2020; Kannan et al. 2022). As our first attempt to overcome the memory issue, we avoid saving gradients for radiation quantities by using a first-order spatial reconstruction, and free most of the saved radiation quantities after radiation transport calculations except for the conserved radiation quantity IV and primitive radiation variable I . However, when the radiation module is active, we still temporarily save at the order of $\mathcal{O}(10N_p N_\Omega N_\nu)$ quantities. A minor improvement is to avoid saving the angle-dependent coefficients (Section 3.4), which reduces the temporarily saved quantities to $\mathcal{O}(N_p N_\Omega N_\nu)$. This is especially relevant if we attempt to move the scheme to GPUs, since the coefficients are supposed to be computed fast and we aim to limit the amount of data exchanged between tasks. Another way to explore is to save the radiation quantities as single precision instead of double precision, as mentioned in Kannan et al. (2022). Nevertheless, more aggressive approaches will be needed if we aim to reduce the number of saved radiation quantities by an order of magnitude. It is foreseeable that, given the memory limit, a VET method closed either by our time-independent discrete-ordinates method or by ray-tracing may be a more practical choice for large simulations, in particular when the simulation is dominated by optically-thin regimes (e.g. reionization).

7. Conclusions

In this paper, we describe an accurate implicit discrete ordinates radiation transport scheme for general-purpose multi-dimensional RMHD simulations on an unstructured moving mesh. We extend and optimize the original finite-volume fixed-mesh scheme developed by J21, and implement the scheme in the moving-mesh MHD code AREPO (Springel 2010; Pakmor et al. 2016; Weinberger et al. 2020). Compared to J21, our new scheme supports

1. An unstructured moving mesh;
2. Local time-stepping;
3. General equations of state.

Our scheme also achieves fast performance. For a 3D red supergiant simulation in Section 5, we reach a relative computational

cost of RMHD : MHD $< 2 : 1$ for moving-mesh with full gravity, and an estimated cost of RMHD : MHD = $10 : 1$ for fixed-mesh with simple gravity. We perform an extensive list of tests to demonstrate these new features and the accuracy of our scheme in optically-thick, optically-thin, or the transition region in between (Section 4). Most of those tests were also performed in J21 and some in Davis et al. (2012) and Jiang et al. (2012, 2014), and the results show clear consistencies, which demonstrates that our scheme performs well even on an unstructured moving mesh with local time-stepping.

We collect our thoughts on future code developments in Section 6. The immediate follow-ups are to extend our scheme to multigroup based on Jiang (2022) and further speedup with GPUs and node-to-node communication based on Zier et al. (2024a). We expect both of these extensions will be relatively straightforward, since both our scheme and the Jiang (2022) multigroup scheme are direct descendants of J21, and the Zier et al. (2024a) speedup was developed for another radiation transport module in AREPO (Kannan et al. 2019). Further uncharted territories include improving the convergence, order of accuracy, and memory load, for which we discuss alternative implicit solvers and trimming the unnecessary storage.

By combining the unique features of AREPO with an accurate radiation transport, we hope that our scheme will open up possibilities to perform moving-mesh RMHD simulations for a vast variety of astrophysical problems where radiation plays an important role. The flexible mesh sizes and local time-stepping provide the rare ability to explore a large dynamic range in both space and time. This is particularly relevant for star formation (Grudić et al. 2021; Chon et al. 2024; Mayer et al. 2024), tidal disruption events (Ryu et al. 2023; Price et al. 2024; Steinberg & Stone 2024), accretion around supermassive black holes (Hopkins et al. 2024; Guo et al. 2023; Jiang & Dai 2024), and galaxy formation and reionization in the early Universe (Vogelsberger et al. 2020; Kannan et al. 2022, 2023), where radiative feedback and/or radiation force are dynamically important. In addition, the moving mesh offers an excellent tool to simulate systems with bulk supersonic motions. This typically happens in gravitationally-bound multi-body systems, such as binary star interactions (Schneider et al. 2019; Röpke & De Marco 2023), astrophysical disks and their interactions with planets, stars, black holes (Benítez-Llambay & Masset 2016; Muñoz et al. 2019; Zhu et al. 2021; Chen et al. 2023; Yao et al. 2024), where the interactions can take the form of radiative heating/cooling or radiation pressure. Supplemented by recent AREPO implementations of non-ideal MHD (Zier et al. 2024b,c) and unique adaptive mesh refinement in shearing box (Zier & Springel 2022a), we expect that many difficult astrophysical problems can now be tackled using moving-mesh RMHD simulations with AREPO. As the ‘first light’ of this prospective endeavor, we are exploring the trans-sonic convection and pulsation in global 3D simulations of red supergiant stars with our new scheme (see Section 5 for a preview), which will be detailed in a forthcoming paper (Ma et al. in prep.).

Acknowledgements. We thank Yan-Fei Jiang for sharing some test problems and helpful discussions. We thank Sebastian Ohlmann for sharing the module to construct stable 3D AREPO giant stars. We thank Andrea Chiavassa for insights on red supergiant simulations. We thank Volker Springel for helpful discussions and giving us access to AREPO and to the computational resources. We thank Paul Ricker, Rahul Kannan, Aaron Smith, Oliver Zier, Thomas Guillet, Daniel Price, Xue-Ning Bai, Robert Andassy, and Giovanni Leidi for discussions on implicit methods and radiation transport with local timesteps. We thank Mike Lau, Jared Goldberg, Taeho Ryu, Sunmyon Chon, Aniket Bhagwat for discussions on 3D radiation hydrodynamic simulations in different fields of astrophysics. This re-

search project was partly conducted using computational resources (and/or scientific computing services) at the Max-Planck Computing & Data Facility. The authors gratefully acknowledge the scientific support and HPC resources provided by the Erlangen National High Performance Computing Center (NHR@FAU) of the Friedrich-Alexander-Universität Erlangen-Nürnberg (FAU) under the NHR project b234dd. NHR funding is provided by federal and Bavarian state authorities. NHR@FAU hardware is partially funded by the German Research Foundation (DFG) – 440719683. The idea for this work was conceived when the author was attending the Interacting Supernovae workshop at the Munich Institute for Astro-, Particle and BioPhysics (MIAPbP) which is funded by the Deutsche Forschungsgemeinschaft (DFG, German Research Foundation) under Germany’s Excellence Strategy – EXC-2094 – 390783311. This work was initiated at the 2023 MPA-Kavli Summer Program in Astrophysics supported by the Max Planck Institute for Astrophysics (MPA) and the Kavli Foundation. Part of this work was done when the author was attending the TDE24 program at Kavli Institute for Theoretical Physics (KITP), which is supported in part by grant NSF PHY-2309135.

Software: AREPO (Springel 2010; Pakmor et al. 2016; Weinberger et al. 2020), MESA (Paxton et al. 2011, 2013, 2015, 2018, 2019; Jermyn et al. 2023), Astropy (Astropy Collaboration et al. 2013, 2018, 2022), NumPy (Harris et al. 2020), SciPy (Virtanen et al. 2020), Matplotlib (Hunter 2007), Jupyter (Kluyver et al. 2016)

Data availability: All the test problems and MESA inlists are available at Zenodo: doi: [10.5281/zenodo.15032138](https://doi.org/10.5281/zenodo.15032138). The radiation module is merged into the master branch or the IDORT branch of AREPO. To use the code, please see the description in Zenodo and contact the first author.

References

- Abel, T. & Wandelt, B. D. 2002, *Monthly Notices of the Royal Astronomical Society*, 330, L53
- Ahmad, A., Freytag, B., & Höfner, S. 2023, *Astronomy and Astrophysics*, 669, A49
- Anninos, P. & Fragile, P. C. 2020, *The Astrophysical Journal*, 900, 71
- Asahina, Y., Takahashi, H. R., & Ohsuga, K. 2020, *The Astrophysical Journal*, 901, 96
- Astropy Collaboration, Price-Whelan, A. M., Lim, P. L., et al. 2022, *The Astrophysical Journal*, 935, 167
- Astropy Collaboration, Price-Whelan, A. M., Sipőcz, B. M., et al. 2018, *The Astronomical Journal*, 156, 123
- Astropy Collaboration, Robitaille, T. P., Tollerud, E. J., et al. 2013, *Astronomy and Astrophysics*, 558, A33
- Baker, N. & Kippenhahn, R. 1962, *Zeitschrift für Astrophysik*, 54, 114
- Bauer, A., Springel, V., Vogelsberger, M., et al. 2015, *Monthly Notices of the Royal Astronomical Society*, 453, 3593
- Benítez-Llambay, P. & Masset, F. S. 2016, *The Astrophysical Journal Supplement Series*, 223, 11
- Borrow, J., Kannan, R., Garaldi, E., et al. 2023, *Monthly Notices of the Royal Astronomical Society*, 525, 5932
- Bourne, M. A. & Sijacki, D. 2017, *Monthly Notices of the Royal Astronomical Society*, 472, 4707
- Bruls, J. H. M. J., Vollmöller, P., & Schüssler, M. 1999, *Astronomy and Astrophysics*, 348, 233
- Cain, C. 2024, *Accurate simulations of reionization using the reduced speed of light approximation*
- Camps, P. & Baes, M. 2018, *The Astrophysical Journal*, 861, 80
- Castor, J. I., Abbott, D. C., & Klein, R. I. 1975, *The Astrophysical Journal*, 195, 157
- Chan, C., Müller, B., Heger, A., Pakmor, R., & Springel, V. 2018, *The Astrophysical Journal*, 852, L19
- Chang, P., Davis, S. W., & Jiang, Y.-F. 2020, *Monthly Notices of the Royal Astronomical Society*, 493, 5397
- Chen, Y.-X., Jiang, Y.-F., Goodman, J., & Ostriker, E. C. 2023, *The Astrophysical Journal*, 948, 120
- Chiavassa, A., Freytag, B., Masseron, T., & Plez, B. 2011, *Astronomy and Astrophysics*, 535, A22
- Chiavassa, A., Kravchenko, K., & Goldberg, J. A. 2024, *Living Reviews in Computational Astrophysics*, 10, 2
- Chiavassa, A., Plez, B., Josselin, E., & Freytag, B. 2009, *Astronomy and Astrophysics*, 506, 1351
- Chon, S., Hosokawa, T., Omukai, K., & Schneider, R. 2024, *Monthly Notices of the Royal Astronomical Society*, 530, 2453
- Colgan, J., Kilcrease, D. P., Magee, N. H., et al. 2016, *The Astrophysical Journal*, 817, 116
- Cox, J. P. & Whitney, C. 1958, *The Astrophysical Journal*, 127, 561
- Das, H. K., Gronke, M., & Weinberger, R. 2024, *MOGLI: Model for Multiphase Gas using Multifluid hydrodynamics*
- Davis, S. W., Stone, J. M., & Jiang, Y.-F. 2012, *The Astrophysical Journal Supplement Series*, 199, 9
- Deparis, N., Aubert, D., Ocvirk, P., Chardin, J., & Lewis, J. 2019, *Astronomy and Astrophysics*, 622, A142
- Eddington, A. S. 1917, *The Observatory*, 40, 290
- Eitner, P., Bergemann, M., Hoppe, R., et al. 2024, *Astronomy and Astrophysics*, 688, A52
- Ferguson, J. M., Morel, J. E., & Lowrie, R. B. 2017, *High Energy Density Physics*, 23, 95
- Ferguson, J. W., Alexander, D. R., Allard, F., et al. 2005, *The Astrophysical Journal*, 623, 585
- Freytag, B., Höfner, S., Aringer, B., & Chiavassa, A. 2024, *Astronomy and Astrophysics*, 692, A223
- Freytag, B., Steffen, M., & Dorch, B. 2002, *Astronomische Nachrichten*, 323, 213
- Freytag, B., Steffen, M., Ludwig, H. G., et al. 2012, *Journal of Computational Physics*, 231, 919
- Geroux, C., Baraffe, I., Viallet, M., et al. 2016, *Astronomy and Astrophysics*, 588, A85
- Gezari, S. 2021, *Annual Review of Astronomy and Astrophysics*, 59, 21
- Gnedin, N. Y. 2016, *The Astrophysical Journal*, 833, 66
- Goffrey, T., Pratt, J., Viallet, M., et al. 2017, *Astronomy and Astrophysics*, 600, A7
- Goicovic, F. G., Springel, V., Ohlmann, S. T., & Pakmor, R. 2019, *Monthly Notices of the Royal Astronomical Society*, 487, 981
- Goldberg, J. A., Jiang, Y.-F., & Bildsten, L. 2022a, *The Astrophysical Journal*, 929, 156
- Goldberg, J. A., Jiang, Y.-F., & Bildsten, L. 2022b, *The Astrophysical Journal*, 933, 164
- Greif, T. H. 2014, *Monthly Notices of the Royal Astronomical Society*, 444, 1566
- Grudić, M. Y., Guszejnov, D., Hopkins, P. F., Offner, S. S. R., & Faucher-Giguère, C.-A. 2021, *Monthly Notices of the Royal Astronomical Society*, 506, 2199
- Guillot, T. 2010, *Astronomy and Astrophysics*, 520, A27
- Guo, M., Stone, J. M., Kim, C.-G., & Quataert, E. 2023, *The Astrophysical Journal*, 946, 26
- Habing, H. J. 1996, *Astronomy and Astrophysics Review*, 7, 97
- Harris, C. R., Millman, K. J., van der Walt, S. J., et al. 2020, *Nature*, 585, 357
- Hayasaki, K., Stone, N., & Loeb, A. 2016, *Monthly Notices of the Royal Astronomical Society*, 461, 3760
- Heger, A., Jeannin, L., Langer, N., & Baraffe, I. 1997, *Astronomy and Astrophysics*, 327, 224
- Hopkins, P. F., Grudić, M. Y., Su, K.-Y., et al. 2024, *The Open Journal of Astrophysics*, 7, 18
- Huang, X., Davis, S. W., & Jiang, Y.-f. 2023, *The Astrophysical Journal*, 953, 117
- Hunter, J. D. 2007, *Computing in Science and Engineering*, 9, 90
- Jaura, O., Glover, S. C. O., Klessen, R. S., & Paardekooper, J. P. 2018, *Monthly Notices of the Royal Astronomical Society*, 475, 2822
- Jaura, O., Magg, M., Glover, S. C. O., & Klessen, R. S. 2020, *Monthly Notices of the Royal Astronomical Society*, 499, 3594
- Jermyn, A. S., Bauer, E. B., Schwab, J., et al. 2023, *The Astrophysical Journal Supplement Series*, 265, 15
- Jiang, Y.-F. 2021, *The Astrophysical Journal Supplement Series*, 253, 49
- Jiang, Y.-F. 2022, *The Astrophysical Journal Supplement Series*, 263, 4
- Jiang, Y.-F. 2023, *Galaxies*, 11, 105
- Jiang, Y.-F. & Dai, L. 2024, *Numerical Simulations of Super-Eddington Accretion Flows*
- Jiang, Y.-F., Stone, J. M., & Davis, S. W. 2012, *The Astrophysical Journal Supplement Series*, 199, 14
- Jiang, Y.-F., Stone, J. M., & Davis, S. W. 2013, *The Astrophysical Journal*, 767, 148
- Jiang, Y.-F., Stone, J. M., & Davis, S. W. 2014, *The Astrophysical Journal Supplement Series*, 213, 7
- Joyce, M., Leung, S.-C., Molnár, L., et al. 2020, *The Astrophysical Journal*, 902, 63
- Kannan, R., Garaldi, E., Smith, A., et al. 2022, *Monthly Notices of the Royal Astronomical Society*, 511, 4005
- Kannan, R., Springel, V., Hernquist, L., et al. 2023, *Monthly Notices of the Royal Astronomical Society*, 524, 2594
- Kannan, R., Vogelsberger, M., Marinacci, F., et al. 2019, *Monthly Notices of the Royal Astronomical Society*, 485, 117
- Kluyver, T., Ragan-Kelley, B., Pérez, F., et al. 2016, in *Positioning and Power in Academic Publishing: Players, Agents and Agendas* (IOS Press)

- Krumholz, M. R., Klein, R. I., McKee, C. F., & Bolstad, J. 2007, *The Astrophysical Journal*, 667, 626
- Leidi, G., Birke, C., Andrassy, R., et al. 2022, *Astronomy and Astrophysics*, 668, A143
- Levermore, C. D. 1984, *Journal of Quantitative Spectroscopy and Radiative Transfer*, 31, 149
- Levermore, C. D. & Pomraning, G. C. 1981, *The Astrophysical Journal*, 248, 321
- Lioutas, G., Bauswein, A., Soultanis, T., et al. 2024, *Monthly Notices of the Royal Astronomical Society*, 528, 1906
- Malygin, M. G., Kuiper, R., Klahr, H., Dullemond, C. P., & Henning, T. 2014, *Astronomy and Astrophysics*, 568, A91
- Marinacci, F., Vogelsberger, M., Pakmor, R., et al. 2018, *Monthly Notices of the Royal Astronomical Society*, 480, 5113
- Mayer, A. C., Zier, O., Naab, T., et al. 2024, *Moving-mesh non-ideal magneto-hydrodynamical simulations of the collapse of cloud cores to protostars*
- Mellema, G., Iliev, I. T., Alvarez, M. A., & Shapiro, P. R. 2006, *New Astronomy*, 11, 374
- Menon, S. H., Federrath, C., Krumholz, M. R., et al. 2022, *Monthly Notices of the Royal Astronomical Society*, 512, 401
- Miczek, F., Röpke, F. K., & Edelmann, P. V. F. 2015, *Astronomy and Astrophysics*, 576, A50
- Mihalas, D. & Mihalas, B. W. 1984, *Foundations of radiation hydrodynamics* (New York: Oxford University Press), aDS Bibcode: 1984oup..book.....M
- Mills, B. S., Davis, S. W., Jiang, Y.-F., & Middleton, M. J. 2024, *The Astrophysical Journal*, 974, 166
- Mocz, P., Burkhardt, B., Hernquist, L., McKee, C. F., & Springel, V. 2017, *The Astrophysical Journal*, 838, 40
- Murchikova, E. M., Abdikamalov, E., & Urbatsch, T. 2017, *Monthly Notices of the Royal Astronomical Society*, 469, 1725
- Murray, N., Chiang, J., Grossman, S. A., & Voit, G. M. 1995, *The Astrophysical Journal*, 451, 498
- Muñoz, D. J., Kratter, K., Springel, V., & Hernquist, L. 2014, *Monthly Notices of the Royal Astronomical Society*, 445, 3475
- Muñoz, D. J., Miranda, R., & Lai, D. 2019, *The Astrophysical Journal*, 871, 84
- Naiman, J. P., Pillepich, A., Springel, V., et al. 2018, *Monthly Notices of the Royal Astronomical Society*, 477, 1206
- Nayakshin, S., Cha, S.-H., & Hobbs, A. 2009, *Monthly Notices of the Royal Astronomical Society*, 397, 1314
- Nelson, D., Pillepich, A., Springel, V., et al. 2018, *Monthly Notices of the Royal Astronomical Society*, 475, 624
- Noebauer, U. M. & Sim, S. A. 2015, *Monthly Notices of the Royal Astronomical Society*, 453, 3120
- Noebauer, U. M. & Sim, S. A. 2019, *Living Reviews in Computational Astrophysics*, 5, 1
- Nordlund, A., Ramsey, J. P., Popovas, A., & Küffmeier, M. 2018, *Monthly Notices of the Royal Astronomical Society*, 477, 624
- O'Connor, E. 2015, *The Astrophysical Journal Supplement Series*, 219, 24
- Ocvirk, P., Aubert, D., Chardin, J., Deparis, N., & Lewis, J. 2019, *Astronomy and Astrophysics*, 626, A77
- Ohlmann, S. T., Röpke, F. K., Pakmor, R., & Springel, V. 2016, *The Astrophysical Journal*, 816, L9
- Ohlmann, S. T., Röpke, F. K., Pakmor, R., & Springel, V. 2017, *Astronomy & Astrophysics*, 599, A5
- Pakmor, R., Bauer, A., & Springel, V. 2011, *Monthly Notices of the Royal Astronomical Society*, 418, 1392
- Pakmor, R., Callan, F. P., Collins, C. E., et al. 2022, *Monthly Notices of the Royal Astronomical Society*, 517, 5260
- Pakmor, R., Springel, V., Bauer, A., et al. 2016, *Monthly Notices of the Royal Astronomical Society*, 455, 1134
- Paxton, B., Bildsten, L., Dotter, A., et al. 2011, *The Astrophysical Journal Supplement Series*, 192, 3
- Paxton, B., Cantiello, M., Arras, P., et al. 2013, *The Astrophysical Journal Supplement Series*, 208, 4
- Paxton, B., Marchant, P., Schwab, J., et al. 2015, *The Astrophysical Journal Supplement Series*, 220, 15
- Paxton, B., Schwab, J., Bauer, E. B., et al. 2018, *The Astrophysical Journal Supplement Series*, 234, 34
- Paxton, B., Smolec, R., Schwab, J., et al. 2019, *The Astrophysical Journal Supplement Series*, 243, 10
- Petkova, M. & Springel, V. 2011, *Monthly Notices of the Royal Astronomical Society*, 415, 3731
- Pillepich, A., Nelson, D., Hernquist, L., et al. 2018, *Monthly Notices of the Royal Astronomical Society*, 475, 648
- Popovas, A., Nordlund, A., & Szydlarski, M. 2022, *Global MHD simulations of the solar convective zone using a volleyball mesh decomposition. I. Pilot*
- Price, D. J., Liptai, D., Mandel, I., et al. 2024, *The Astrophysical Journal*, 971, L46
- Proga, D., Jiang, Y.-F., Davis, S. W., Stone, J. M., & Smith, D. 2014, *The Astrophysical Journal*, 780, 51
- Rogers, F. J. & Nayfonov, A. 2002, *The Astrophysical Journal*, 576, 1064
- Rosdahl, J., Blaizot, J., Aubert, D., Stranex, T., & Teyssier, R. 2013, *Monthly Notices of the Royal Astronomical Society*, 436, 2188
- Ryu, T., Amaro Seoane, P., Taylor, A. M., & Ohlmann, S. T. 2024a, *Monthly Notices of the Royal Astronomical Society*, 528, 6193
- Ryu, T., Krolik, J., Piran, T., Noble, S. C., & Avara, M. 2023, *The Astrophysical Journal*, 957, 12
- Ryu, T., McKernan, B., Ford, K. E. S., et al. 2024b, *Monthly Notices of the Royal Astronomical Society*, 527, 8103
- Röpke, F. K. & De Marco, O. 2023, *Living Reviews in Computational Astrophysics*, 9, 2
- Schneider, F. R. N., Ohlmann, S. T., Podsiadlowski, P., et al. 2019, *Nature*, 574, 211
- Secunda, A., Jiang, Y.-F., & Greene, J. E. 2024, *The Astrophysical Journal*, 965, L29
- Sekora, M. D. & Stone, J. M. 2010, *Journal of Computational Physics*, 229, 6819
- Siwek, M., Weinberger, R., Muñoz, D. J., & Hernquist, L. 2023, *Monthly Notices of the Royal Astronomical Society*, 518, 5059
- Skinner, M. A. & Ostriker, E. C. 2013, *The Astrophysical Journal Supplement Series*, 206, 21
- Smit, J. M., Cernohorsky, J., & Dullemond, C. P. 1997, *Astronomy and Astrophysics*, 325, 203
- Smith, A., Kannan, R., Tsang, B. T. H., Vogelsberger, M., & Pakmor, R. 2020, *The Astrophysical Journal*, 905, 27
- Sparre, M., Pfrommer, C., & Vogelsberger, M. 2019, *Monthly Notices of the Royal Astronomical Society*, 482, 5401
- Springel, V. 2010, *Monthly Notices of the Royal Astronomical Society*, 401, 791
- Springel, V., Pakmor, R., Pillepich, A., et al. 2018, *Monthly Notices of the Royal Astronomical Society*, 475, 676
- Stark, D. P. 2016, *Annual Review of Astronomy and Astrophysics*, 54, 761
- Stein, R. F. & Nordlund, A. 1989, *The Astrophysical Journal*, 342, L95
- Steinberg, E. & Stone, N. C. 2024, *Nature*, 625, 463
- Stone, J. M., Mihalas, D., & Norman, M. L. 1992, *The Astrophysical Journal Supplement Series*, 80, 819
- Stone, J. M., Tomida, K., White, C. J., & Felker, K. G. 2020, *The Astrophysical Journal Supplement Series*, 249, 4
- Sądowski, A., Narayan, R., Tchekhovskoy, A., & Zhu, Y. 2013, *Monthly Notices of the Royal Astronomical Society*, 429, 3533
- Talbot, R. Y., Sijacki, D., & Bourne, M. A. 2024, *Monthly Notices of the Royal Astronomical Society*, 528, 5432
- Teyssier, R. 2015, *Annual Review of Astronomy and Astrophysics*, vol. 53, p.325-364, 53, 325
- Thomas, T. & Pfrommer, C. 2022, *Monthly Notices of the Royal Astronomical Society*, 509, 4803
- Tiwari, V., Chan, C.-H., Bogdanović, T., et al. 2025, *Radiation Magnetohydrodynamic Simulation of sub-Eddington Circumbinary Disk around an Equal-mass Massive Black Hole Binary*
- Viallet, M., Goffrey, T., Baraffe, I., et al. 2016, *Astronomy and Astrophysics*, 586, A153
- Virtanen, P., Gommers, R., Oliphant, T. E., et al. 2020, *Nature Methods*, 17, 261
- Vogelsberger, M., Nelson, D., Pillepich, A., et al. 2020, *Monthly Notices of the Royal Astronomical Society*, 492, 5167
- Vynatheya, P., Ryu, T., Pakmor, R., de Mink, S. E., & Perets, H. B. 2024, *Astronomy and Astrophysics*, 685, A45
- Weinberger, R., Ehlert, K., Pfrommer, C., Pakmor, R., & Springel, V. 2017, *Monthly Notices of the Royal Astronomical Society*, 470, 4530
- Weinberger, R., Springel, V., & Pakmor, R. 2020, *The Astrophysical Journal Supplement Series*, 248, 32
- White, C. J., Mullen, P. D., Jiang, Y.-F., et al. 2023, *The Astrophysical Journal*, 949, 103
- Whitehouse, S. C., Bate, M. R., & Monaghan, J. J. 2005, *Monthly Notices of the Royal Astronomical Society*, 364, 1367
- Wise, J. H. & Abel, T. 2011, *Monthly Notices of the Royal Astronomical Society*, 414, 3458
- Woitke, P., Min, M., Pinte, C., et al. 2016, *Astronomy and Astrophysics*, 586, A103
- Wünsch, R. 2024, *Frontiers in Astronomy and Space Sciences*, 11, 1346812
- Yao, P. Z., Quataert, E., Jiang, Y.-F., Lu, W., & White, C. J. 2024, *Star-Disk Collisions: Implications for QPEs and Other Transients Near Supermassive Black Holes*
- Zel'dovich, Y. B. & Raizer, Y. P. 1967, *Physics of shock waves and high-temperature hydrodynamic phenomena* (New York: Academic Press), aDS Bibcode: 1967pswh.book.....Z
- Zhang, L., Blaes, O., & Jiang, Y.-F. 2022, *Monthly Notices of the Royal Astronomical Society*, 515, 4371
- Zhang, S., Zhu, Z., & Jiang, Y.-F. 2024, *The Astrophysical Journal*, 968, 29
- Zhevakin, S. A. 1963, *Annual Review of Astronomy and Astrophysics*, 1, 367

- Zhu, Z., Jiang, Y.-F., Baehr, H., et al. 2021, *Monthly Notices of the Royal Astronomical Society*, 508, 453
- Zhu, Z., Zhang, S., Jiang, Y.-F., et al. 2019, *The Astrophysical Journal*, 877, L18
- Zier, O., Kannan, R., Smith, A., Vogelsberger, M., & Verbeek, E. 2024a, *Monthly Notices of the Royal Astronomical Society*, 533, 268
- Zier, O., Mayer, A. C., & Springel, V. 2024b, *Monthly Notices of the Royal Astronomical Society*, 527, 8355
- Zier, O. & Springel, V. 2022a, *Monthly Notices of the Royal Astronomical Society*, 515, 525
- Zier, O. & Springel, V. 2022b, *Monthly Notices of the Royal Astronomical Society*, 517, 2639
- Zier, O. & Springel, V. 2023, *Monthly Notices of the Royal Astronomical Society*, 520, 3097
- Zier, O., Springel, V., & Mayer, A. C. 2024c, *Monthly Notices of the Royal Astronomical Society*, 527, 1563